2021

Dynamic Modelling and Control of Grid-Level Energy Storage Systems

Sai Pushpitha Vudata
West Virginia University, sv0015@mix.wvu.edu

Dynamic Modelling and Control of Grid-Level Energy Storage Systems

Sai Pushpitha Vudata

Dissertation submitted to the
Benjamin M. Statler College of Engineering and Mineral Resources
At West Virginia University
in partial fulfillment of the requirements for the degree of

Doctor of Philosophy
in
Chemical Engineering

Debangsu Bhattacharyya, Ph.D., Chair

Richard Turton, Ph.D.

Fernando V. Lima, Ph.D.

Xingbo Liu, Ph.D.

Parviz Famouri, Ph.D.

DEdward M. Sabolsky, Ph.D.

Department of Chemical and Biomedical Engineering

Morgantown, West Virginia

2021

Keywords: energy storage, rechargeable secondary battery, transient modeling, capacity fade, reduced order modeling, thermal management, parameter estimation, kalman filter

Abstract

Dynamic Modelling and Control of Grid-Level Energy Storage Systems

Sai Pushpitha Vudata

The focus of this work is on two energy storage technologies, namely pumped storage hydroelectricity (PHS) and secondary batteries. Under secondary battery technologies, two potential technologies for grid-scale storage, namely high-temperature sodium-sulfur (NaS) battery and vanadium redox flow battery (VRFB), are investigated. PHS is a largescale (>100 MW) technology that stores and generates energy by transporting water between two reservoirs at different elevations. The goal is to develop a detailed dynamic model of PHS and then design the controllers to follow the desired load trajectory accurately with high efficiency. The NaS battery and VRFB are advanced secondary batteries which can be charged and discharged rapidly. Since temperature excursion of high temperature NaS batteries especially under fast cycling conditions is a safety hazard and the temperature excursion can take place at some location within the cell where measurement is not feasible, the focus is on a model-based approach for transient analysis and development of novel thermal management techniques. A detailed thermo-electrochemical dynamic model of a single NaS has been developed. As a detailed cell model is computationally intractable for simulating large number of cells in the battery, various strategies such as coordinate transformation, orthogonal collocation, and model reformulation have been developed to obtain a reduced order model that solves significantly faster than the full, high-dimensional model but provides an accurate estimate of the key variables such as transient voltage/current/temperature profile in the cell. Sodium sulfur batteries need to be maintained within a temperature range of 300-400^{0}C. Therefore, the focus was on developing thermal management strategies that can not only maintain the cell temperature near the optimum, but can effectively utilize the heat, improving the overall efficiency of the battery system. VRFBs can provide large amount of storage as the electrolytes are stored in separate tanks. However, the self-discharge reactions (due to crossover) along with the undesired side reactions and the dissolved water in the membrane, can significantly reduce the capacity. A dynamic model-based approach is developed for detection, identification, and estimation of capacity fade and SOC as a function of time. A model-based prognostic capability has been developed for estimating the remaining useful cell life.

Dedicated to

My parents

Acknowledgement

I would like to express my sincere gratitude to Dr. Debangsu Bhattacharyya, my advisor, for giving me an opportunity to broaden my knowledge by giving me a chance as a PhD student in his research lab. His immense knowledge and expertise in the subject helped me throughout my course not only in understanding but also in solving unexpected issues in dynamic modelling and optimization of energy systems, especially in Aspen. His support and mentorship were of great support in my development as a researcher. I would also like to express my gratitude to Dr. Richard Turton, who I collaborated with in this project, for sharing his valuable knowledge and encouraging me. I would further like to acknowledge Dr. Fernando. V. Lima for his constant support, encouragement, and knowledge share. I would like to thank my committee members, Dr. Xingbo Liu, Dr. Parviz Famouri and Dr. Edward M. Sabolsky, for their insight, support, and advices in my research. I would also like to thank Dr. Nagasree for her mental support and encouragement.

I earnestly thank all the members from Dr. Debangsu's research group for sharing their knowledge and vision and helping in building a friendly and exciting research environment. I would specially like to thank Dr. Pratyusha, Dr. Yuan, Dr. Yifan, Rebecca Kim, Anca, Paul and Chandra Shekar for sharing their knowledge and for making research fun. I specially thank all my friends Sasank, Hemanth, Chandu, Sujan, Satish, Anudeep, Rama pinni, Akhil, Savan, Nikitha akka, Surekha, Sahiti, Koushik, Meghana, Sasanka, Pratyusha, Niharika, Ranaa, Ashish, Akash, Pavan, Chakri, Harika and Sharath for bearing me and supporting me and making life fun at WVU.

Most importantly, I thank my mother for her constant support throughout my life and my father for his support, knowledge sharing and keen insights. And I would like to acknowledge my sister and her family for always being there for me and giving me the confidence to pursue this. Finally, I thank Vivek Komarina for always being my constant support through all the phases at WVU.

I would like to thank Ms. Linda Rogers for helping me with all essential paper works, Dr. Charter Stinespring for his academic counsels.

I gratefully acknowledge the financial support from U.S. Department of Energy through U.S.-China Clean Energy Research Center (CERC) program under Cooperative Agreement DE-PI0000017.

Table of Contents

List of Figures

List of Tables

Nomenclature

Chapter 2 & 3

a_s	*Surface area of graphite matrix per unit volume sulfur electrode (m^2/m^3)*
a_{s0}	*Net surface area of graphite matrix per unit volume sulfur electrode (m^2/m^3)*
$A(t)$	*Coefficient of linear or quadratic term—Solved in terms of B(t) using BCs*
$B(t)$	*Collocation coefficients*
c_p	*Specific heat capacity (J/kgK)*
C_+	*Concentration of sodium ions ($kmol/m^3$)*
D	*Diffusion coefficient (m^2/s)*
D_0	*Arrhenius constant for electrolyte diffusion coefficient (m^2/s)*
dE/dT	*Temperature dependence of open circuit voltage (V)*
e^-	*Electron*
F	*Faraday constant (C/kmol)*
$H`$	*Activation energy for sodium ion movement in electrolyte (kcal/mol)*
H	*Activation energy for sodium ion movement in electrolyte (kCal/mol)*
h	*heat transfer coefficient (W/m^2K)*
h'	*sensible heat (kJ/kg)*
ΔH	*specific enthalpy change (kJ/kg)*
I	*Current (A)*
i_0	*Exchange current density of sodium electrode (A/m^2)*
J	*Current density ($C/s.m^2$)*
K_p	*Polarization coefficient ($ohm.m^2$)*
L	*Length of electrolyte (m)*
M	*Mole fraction elemental sulfur in sulfur electrode*
m	*Mass (kg)*
MW	*Molecular weight (kg/mol)*
N	*Number of terms in the approximate solution*
Nu	*Nusselt number*
p	*Porosity*
p_t	*Thermoelectric power (V/K)*
Pr	*Prandtl number*
$P(r)$	*Jacobi polynomial*
q	*Heat source term (W/m^3)*
Q_{Ohmic}	*Heat due to Ohmic losses (W/m^3)*
$Q_{Entropy}$	*Heat due to reaction (W/m^3)*
R	*Ideal gas constant (C/kmol K)*
r	*Radius (m)*
$r_{el,i}$	*Radius of inner electrolyte (m)*

$r_{el,o}$	*Radius of outer electrolyte (m)*
Re	*Reynolds number*
r_o	*Radius of outer cell container (m)*
$R_{universal}$	*Ideal gas constant (C/kmol K)*
SOD	*State of discharge (with respect to Na_2S_3) (Ah(max)/Ah)*
T	*Temperature (^0C)*
T_{air}	*Temperature of ambient air (^0C)*
T_{PCM}	*Temperature of phase change material ($^\circ C$)*
t	*Time (s)*
t_+	*Transference number of sodium ions*
v	*velocity (m/s)*
V	*Volume (m^3)*
W_s	*Weight of initially charged sulfur (kg)*
x	*Subscript in polysulfide, Na_2S_x*
X_e	*Mole fraction electrolyte (Na_2S)*
X_s	*Value of x in polysulfide, Na_2S_x*

Chapter 4

a	*wave speed (m/s)*
A	*cross-sectional area (m^2)*
C	*Hydraulic capacitance*
D	*Pipe diameter (m)*
f	*coefficient of friction*
g	*acceleration due to gravity (m/s^2)*
h	*dimensionless head*
Δh	*dimensionless hydraulic loss*
H	*pressure head (m)*
L	*Hydraulic inductance*
$\widetilde{m_s}$	*dimensionless start torque*
q	*dimensionless flow*
Q	*flow (m^3/s)*
R_p	*pumping parameter*
R	*Hydraulic resistance*
R_m	*mechanical loss coefficient*
t_s	*starting torque*
T_a	*time constant of rotational mass in turbine*
T_{wt}	*time constant of water in turbine*
V	*velocity (m/s)*

Chapter 5 & 6

a	*specific surface area of porous carbon electrode (m^{-1})*
A	*geometric area of collector (m^2)*
c	*concentration (mol/m^3)*
c^s	*concentration at liquid-solid interface (mol/m^3)*
d_f	*mean fibre diameter (m)*
d_g	*gas bubble diameter (m)*
d	*inter-fibre distance (m)*
D	*diffusion coefficient (m^2/s)*
E_0	*open-circuit voltage (V)*
E_{cell}	*cell voltage (V)*
F	*Faraday's constant (C/mol)*
h	*electrode height (m)*
I_{app}	*applied current (load) (A)*
$\vec{j}$	*current density (A/m^2)*
k	*permeability (m^2)*
k_i	*reaction rate constants (i = 1, 2) (m/s)*
k_m	*local transfer constant (m/s)*
k_d	*dissociation coefficient (mol/m^3s)*
K	*Kozeny–Carman constant*
L	*thickness (m)*
$\vec{n}$	*unit outer normal*
m	*Molar mass (kg/mol)*
$\vec{N}$	*molar flux (mol/m^3s)*
Nu	*Nusselt number*
p	*pressure (Pa)*
R	*universal gas constant (J/mol K)*
S	*source/sink (mol/m^3s)*
S_{cr}	*crossover flux (mol/m^3s*
S_d	*diffusive source term (mol/m^3s)*
SOC	*State of charge (Ah(max)/Ah)*
t	*time (s)*
T	*temperature (^0C)*
E	*cell voltage (V)*
Q	*heat source (W/m)*
V	*electrolyte tank volume (half-cell) (m^3)*
$\vec{v}$	*velocity (m/s)*
v_{slip}	*slip velocity (m/s)*
w	*width (m)*
x	*thickness (m)*

y	*height (m)*
z	*valence*

Greek Letters

Chapter 2 & 3

α	*Heat transfer coefficient between the cell container and the air (W/m^2K)*
α_1	*Overpotential coefficient (Risch and Newman* [43]*) (V)*
α_L	*Linear coefficient of thermal expansion for electrolyte (1/K)*
β_1	*Overpotential coefficient (Risch and Newman* [43]*) (V)*
β_3	*Overpotential coefficient (Risch and Newman* [43]*) (V)*
δ	*Stefan-Boltzmann constant (Wm^2/K^4)*
ϵ	*Effective emissivity*
$\eta_{(Na)}$	*Overpotential of sodium electrode (V)*
λ	*Thermal conductivity (W/mK)*
μ	*Local potential (V)*
ρ	*Density (kg/m^3)*
$\rho_{l(Na)}$	*Resistivity of liquid sodium (ohm.m)*
σ_0	*Arrhenius constant for electrolyte ionic conductivity (K/Ohm.m)*
σ_e	*Electronic conductivity (A/V)*
σ_i	*Ionic conductivity (A/V)*
σ_{i0}	*Net ionic conductivity of polysulfide melt (1/Ohm.m)*
φ_0	*Cell potential (voltage) (V)*
φ_e	*Electronic potential (V)*
φ_i	*Ionic potential (V)*
μ·	*viscosity (kg/m.s)*
β	*liquid fraction*
γ	*specific latent heat (kJ/kg)*

Chapter 4

α	*pipe inclination angle*
γ	*pumping parameter*
κ	*guide vane angle*
λ	*local loss coefficient*
η_g	*efficiency of generator*
σ	*machine constant*
ω	*dimensionless torque*
φ	*machine constant*

Chapter 5 & 6

α	*transfer coefficient*
γ	*piston velocity (m/s)*
ϵ	*volume fraction*
β_l	*volume fraction of liquid*
β_g	*volume fraction of gas*
η	*overpotential (V)*
κ	*ionic conductivity (S/m)*
λ	*thermal conductivity (W/mK)*
μ	*dynamic viscosity (kg/ms)*
ϕ	*potential (V)*
ϕ_e	*ionic potential (V)*
ϕ_s	*electronic potential (V)*
ρ	*density (kg/m)*
σ	*conductivity (S/m)*
θ	*degree of dissociation*
ω	*volumetric flow rate (m^3/s)*

Subscripts

Chapter 2 & 3

air	*Air in the furnace, surrounding sodium sulfur cell*
(el)	*Denotes variable within the beta"-alumina electrolyte*
(Na)	*Denotes variable within the beta sodium electrode*
Na	*Liquid sodium in the sodium electrode*
PCM	*PCM surrounding the sodium sulfur cell*
(S)	*Denotes variable within the beta sulfur electrode*
ss	*Stainless steel wick in the sodium electrode*

Chapter 5 & 6

a	*anodic property*
air	*property of air*
app	*applied quantity*
av	*average value*
c	*cathodic property*
coll	*current collector quantity*
d	*dissociation property*
e	*liquid or ionic property*
f	*fixed charge quantity*
g	*gaseous property*
H^+	*protons*

H_2O	*water property*
H_2	*hydrogen gas property*
HSO_4^-	*bi-sulphate ion*
i	*species i*
in	*inlet value*
k	*reaction (1) or (2)*
l	*liquid property*
s	*solid or electronic property*
O_2	*oxygen gas property*
SO_4^{-2}	*sulphate ion*
V^{+2}	*vanadium ion with +2 oxidation state*
V^{+3}	*vanadium ion with +3 oxidation state*
V^{+4}	*vanadium ion with +4 oxidation state*
V^{+5}	*vanadium ion with +5 oxidation state*
w	*water property (membrane)*
0	*initial or equilibrium value*
−	*negative electrode quantity/property*
+	*positive electrode quantity/property*

Superscript

Chapter 5 & 6

cc	*current collector*
e	*electrolyte property*
eff	*effective value*
in	*inlet value*
m	*membrane property*
out	*outlet value*
s	*liquid-solid interface property*
0	*initial value*
−	*volume average*

Abbreviations

ACM	*Aspen custom modeler*
AIC	*Akaike information criterion*
ARX	*Autoregressive exogeneous model*
AS-PHS	*Adjustable speed pumped hydro storage*
BESS	*Battery energy storage system*
CAES	*Compressed air energy storage*
CC	*Coulomb counting*

C-PHS	*Conventional pumped hydro system*
ECM	*Equivalent circuit models*
HSC	*Hydraulic short circuit*
HT-NaS	*High temperature sodium sulfur battery*
IT-NaS	*Intermediate temperature sodium sulfur battery*
KF	*Kalman filter*
MIMO	*Multi input multi output system*
NaS	*Sodium sulfur battery*
NAARX	*Non-linear additive autoregressive with exogenous input*
OCV	*Open circuit voltage*
ODE	*Ordinary differential equations*
PCM	*Phase change material*
PDAE	*Partial differential algebraic equations*
PHS	*Pumped hydro-electric storage*
PID	*Proportional-integral-derivative controller*
PRBS	*Pseudorandom binary sequence*
RC	*Resistance capacitance models*
RFB	*Redox flow battery*
RMSE	*Root mean squared error*
ROM	*Reduced order models*
RT-NaS	*Room temperature sodium sulfur battery*
SMO	*Sliding mode observer*
SOC	*State of charge*
SOD	*State of discharge*
TSE	*Total squared error*
T-PHS	*Ternary pumped hydro system*
VCHP	*Variable conductance heat pipe*
VRFB	*Vanadium redox flow battery*

Chapter 1. Introduction

1.1. Overview

Due to the increased demand for energy, rapidly aging electric transmission and distribution infrastructure and increased concerns regarding the environmental influences has been a growing interest to produce and supply energy more efficiently. Renewable energy sources such as wind and solar have been growing at a remarkable rate over the last several years. However, these energy sources are intermittent and vary irrespective of the demand [1]. Therefore, fossil-fueled power sources are playing a critical role by rapidly changing their load to take care of the imbalance between the demand and supply. However, rapid load-following and low-load operation causes efficiency loss and have adverse effects on the plant health [2][3]. Energy storage, especially at large-scale, can reduce the imbalance to a great extent thus addressing some of the major issues caused by the increasing integration of renewables into the grid [4][5][6][7]. Modern electric grid helps to meet the challenge of handling projected energy needs, including addressing climate change by incorporating more energy from renewable sources and improving efficiency from non-renewable energy processes. There is considerable research effort worldwide for modelling and optimizing the efficiency and safety of the existing technologies for energy storage. The research work proposed here focuses on three energy storage technologies that have the potential to improve the reliability and feasibility of the future grid with large presence of renewable energy sources. The first technology that will be investigated is the advanced sodium sulfur battery (NaS). The temperature of NaS batteries should be maintained between 300°C and 400°C for proper operation of the cell [8]. These batteries are considered to be a very attractive developing technology, because they can be cycled large number of times with little loss in performance and have long discharge cycles, fast response [9] and high energy density (760 Wh/kg at 350^{o}C) [7]. A limitation of this type of cells is that while the cell is idling, its temperature still needs to be maintained above 300^{o}C so an external heating system may be needed in absence of a proper thermal management strategy thus lowering the battery efficiency. On the other hand, if the cell temperature exceeds 400^{o}C, there can be fire hazards. Thus, a reliable and efficient thermal management strategy is critical for deployment of NaS for grid-level energy storage. Another potential battery technology is vanadium redox flow battery (VRFB). In VRFB, energy is stored by employing vanadium redox

couples (V^{2+}/V^{3+} in the negative and V^{4+}/V^{5+} in the positive half-cells) [10]. Unlikely of non-flow batteries, power and energy ratings of VRFB are independent of each other and each may be optimized separately for a specific application since the electrolytes are stored in external tanks. However, the self-discharge reactions along with the undesired side reactions and the water transported through the membrane can significantly reduce the capacity of VRFBs [11]. In this research, for maximizing the utilization and overall energy efficiency of VRFBs under load-following applications, their design and operation will be optimized with due consideration of the undesired efficiency loss mechanisms. A condition monitoring technique will be developed that can co-estimate the current state of capacity fade in the battery and helps in determining the time at which the electrolytes are to be remixed/rebalanced to avoid complete damage to the system. The third technology being considered is the pumped hydro-electric storage system (PHS). This is a largescale (>100 MW) technology, which can store the electric energy in the form of gravitational energy and utilizes the stored energy when demand is higher than supply. Though PHS has advantages like energy management via time shift, supply reserve and non-spinning reserve [12], as well as long lasting lifetime and practically unlimited cycle stability; the key disadvantages are the large land use and the dependence on topographical conditions. The goal is to develop a dynamic model of PHS incorporating electric machine dynamics and hydraulic dynamics. This model can be used to study the feasibility of PHS to regulate the frequency with due consideration of the discrepancy between the demand and supply.

1.2. Specific Objectives

Specific Aim #1: *Development of a Non-isothermal, Dynamic Model of a Sodium-Sulfur Cell*. The sodium-sulfur battery has high potential for electrical storage at the grid level due to its high energy density, low cost of the reactants, and high open-circuit voltage. However, the use of sodium-sulfur batteries at the grid level requires high current density operation that can cause cell deterioration, leading to lower sulfur utilization and lower energy efficiency. In addition, it can result in undesired thermal runaway leading to potentially hazardous situations. A rigorous, dynamic model of a sodium-sulfur battery can be used to study these phenomena, design the battery for optimal transient performance, and develop mitigation strategies. Most literature on sodium-sulfur batteries is concerned about the dynamics of the sulfur electrode (a sodium-polysulfide melt). There is limited data in the open literature for dynamics of an entire cell. With this motivation, a

first principles, fully coupled thermal-electrochemical dynamic model of the entire sodium-sulfur cell will be developed. The thermal model will consider heat generation due to Ohmic loss, Peltier heat, and heat due to entropy change. Species conservation equations in the sulfur electrode will consider phase transition and change in the composition depending on the SOD. Species conservation equations will be written in the beta"-alumina electrolyte for the ionic species by considering the change in composition due to diffusion and migration. In addition, the potential distribution, and cell resistance for this spatially distributed system will be modeled. Furthermore, temperature-dependent correlations for the physicochemical properties will be developed. The model will be used to study both charging and discharging characteristics of the cell at varying current densities.

Specific Aim #2: *Development of a NaS Battery Model and its Thermal Management strategies.* The cell model developed under Specific Aim#1 is computationally intractable for simulating the large number of cells in the battery. Various strategies such as coordinate transformation, orthogonal collocation, and model reformulation [13] will be developed to obtain a reduced order model that can be solved significantly fast yet provides an accurate estimate of the key variables. Under rapid charging/discharging, especially under discharging conditions, it can lead to significant excursion in the battery temperature when the current density is high. Efficient thermal management strategies will be developed not only for maintaining the cell temperature near the optimum under rapid cycling operation at high current density but can effectively utilize the heat thus improving the overall efficiency of the system.

Specific Aim #3: *Transient Modeling of a Vanadium Redox Flow Battery*. The vanadium redox flow battery (VRFB) is a rechargeable flow battery that is one of the most promising large-scale energy storage systems making them suitable for grid energy storage. However, the self-discharge reactions along with the undesired side reactions and water transfer through the membrane causes imbalance in electrolyte and state-of-charge (SOC), which can significantly reduce the capacity of VRFBs [11],[14]. Remixing/rebalancing of electrolytes can mostly reverse the capacity fade [11]. A rigorous, dynamic model of a vanadium redox flow battery can be used to study these phenomena, determine when to remix/rebalance electrolytes, identify the battery for estimating the capacity and state. Most literature on vanadium redox flow batteries is concerned about the chemistry of the carbon electrodes and the membrane. There are works in the existing literature on vanadium redox flow batteries considering individual capacity fade mechanisms. With this

motivation, a first principles, 2D electrochemical dynamic model of all-vanadium redox flow battery will be developed. The electrochemical model will consider self-discharge reactions, caused by the diffusion, convection, and migration of the vanadium ions from one half-cell to the other. In addition, side reactions, as a result of evolution of hydrogen and oxygen gases and water transfer through the membrane will be considered. Furthermore, the Donnan potential, as a result of ion-crossover, at the membrane electrode interface will be determined. The model will be used to study both charging and discharging characteristics of the cell at varying current densities and electrolyte flowrates.

Specific Aim #4: *Condition Monitoring through Co-estimation of Capacity and State of Charge.* The vanadium redox flow battery model developed in specific aim #3 considers capacity fade mechanisms, ion-crossover, side reactions and water transfer through the membrane. Under rapid charging/discharging conditions, it can lead to significant excursion in the capacity of the battery. Remixing/ rebalancing of electrolytes helps to reverse the capacity fade. The developed 2D model is used first for identification and later for estimation. A dynamic model-based approach will be proposed to identify the model. A computationally efficient Kalman filter will be developed for co-estimating time-varying capacity fade and state of the battery under the effect of variable operating conditions.

Specific Aim #5: *Development of a Dynamic Model of Pumped Hydro Storage System.* A mathematical model of PHS will be developed to study the hydraulic transients and the generation/consumption curves. Though PHS can store large amounts of energy at a lower cost, the capital costs and geography are critical decisive factors [15]. Therefore, this work involves the development of a dynamic model considering both electric machine dynamics and hydraulic dynamics to study the impact of storage volume and elevation changes. The model will be simulated for following the desired load trajectory with maximum efficiency.

1.3. Expected Significance

The expected significance of the proposed research includes:

i) First-principles fully coupled thermal-electrochemical model of NaS cells to understand the effects of heat generation rate, rates of electrochemical reactions, and internal resistance.

ii) development of reduced order models of NaS, which are then sued for developing a battery model.
iii) thermal management strategies for maintaining the temperature of NaS batteries within desired limit while utilizing the generated heat.
iv) identification of the reactions involved in cross-contamination of vanadium ions in VRFB and development of a dynamic model to predict the capacity loss due to these reactions.
v) a condition monitoring framework to co-estimate the state of charge and capacity of VRFB.
vi) electromechanical model of PHS including hydrodynamics.
vii) reduced order modeling of battery systems for future optimization and integration.

Chapter 2. Transient Modeling and Simulation of a Non-isothermal Sodium-Sulfur Cell

2.1. Literature Review

Renewable energy sources such as wind and solar have been growing at a remarkable rate over the last several years. However, these energy sources are intermittent and vary irrespective of the demand [1]. Therefore, fossil-fueled power sources are playing a critical role by rapidly changing their load to take care of the imbalance between the demand and supply. However, rapid load-following and low-load operation causes efficiency loss and have adverse effects on the plant health [2][3]. Energy storage, especially at large-scale, can reduce the imbalance to a great extent thus addressing some of the major issues caused by the increasing integration of renewables into the grid [4][5][6][7].

Energy can be stored on a large scale in various storage systems like pumped hydroelectric, compressed air energy storage (CAES), battery energy storage systems (BESS), etc. However, pumped hydroelectric and CAES are large energy storage systems and require certain geographical formations that are often located far from the locations where electricity is needed. BESS are modular and do not need any geographical formations [16][17][18]. Moreover, smaller systems have typically faster ramp rates compared to larger units [19]. BESS are highly scalable and have fast response time to peak shaving and load shifting, improving the grid reliability and stability [16][18] [19][20]. Further, BESS are suitable for on/off operations and can be centrally located or distributed [21].

Depending on the combinations of materials and chemicals used, a wide range of battery technologies is available [7][16][17][18]. For grid-level storage, various secondary battery technologies are of main interest since they can be discharged and charged repeatedly, have high energy densities, low self-discharge rates, and long life-times. Rechargeable Li-ion batteries are currently being widely evaluated as a promising technology since they have significantly high energy density and a long cycle life [22][23]. However, Coulombic overheating and high costs are the major constraints for large-scale commercialization of Li-ion technology. Therefore, the ongoing need to store energy more safely, compactly and affordably motivates continued research on alternative battery technologies [24][25][26][27]. Sodium is the second lightest alkali metal.

Using sodium in the anode coupled with an appropriate cathode material can help to achieve high specific energy density and high open circuit voltage at a lower cost compared to Li-ion batteries [27][28][29][30].

When liquid sulfur is used in the cathode with beta”-alumina as the electrolyte, the resulting sodium sulfur (NaS) battery yields high energy density, low cost of the reactants, high open-circuit voltage and comparatively inexpensive cathode and anode making the NaS battery an ideal candidate for grid-level energy storage applications [31][32]. The NaS batteries can be operated under room temperature [33][34][35] but room-temperature NaS batteries have a low-capacity retention and poor cycling properties [26]. For grid-level storage applications, high-temperature sodium-sulfur batteries are of main interest. These batteries typically operate at 300-400^{o}C and have the desired favorable characteristics as discussed earlier for grid-level storage applications. However, one of the issues of these batteries is thermal runaway especially under high energy-density operation. For developing an efficient thermal management system, a detailed dynamic model of the entire cell that can capture the nonlinearities of the NaS cells under changing operating conditions will be critical.

There is a lack of research literature on modeling of sodium-sulfur cells/batteries in the public domain. Sudworth and Tilley [30] described the development of sodium-sulfur batteries, principles of their operation, design and manufacture, performance and safety as well as prototype demonstrations. β″- alumina electrolyte shows high sodium ion conductivity at high temperature, which helps the Na-S battery to operate effectively at low loss. Initially the cell remains in the two-phase region containing mainly sulfur along with some amount of sodium polysulfide depending on the SOD. As reactions proceed, the sulfur electrode becomes single phase containing only polysulfide. As a result, not only does the capacity get reduced, but also the cell voltage (EMF) gets affected. The cell voltage and capacity depend on the potential profile and electrochemical reaction rates in the electrodes as well as the sodium ion conductivity of the electrode – all of which are strongly affected by the operating temperature of the cell [36][37][38][39][40]. The SOD also affects the cell resistance and the heat generation rate and entropy [41][42]. However, the cell potential profile as well as other key variables are also affected due to the inhomogeneous composition of the sulfur electrode. Kawamoto [43] investigated the 2-D distribution of the melt in sulfur electrode and observed that at high current density, the non-uniformity in the melt

increases thus decreasing the sulfur utilization. For grid-connected application, high energy density operation of the batteries is of significant interest. However, high energy density operation causes low sulfur utilization, low energy efficiency and unusual temperature rise due to high heat generation rates. Kawamoto and Kusakabe [44] have investigated the high current density operation of a single sodium sulfur cell, but the impact of concentration polarization was neglected. Kawamoto [45] developed a non-isothermal dynamic model by capturing the spatial variation of the cell voltage and ion concentration profile, but only the sulfur electrode was modeled. The effect of temperature and mole fraction of electrolyte on the sodium ion diffusion coefficient in the sulfur electrode was also neglected.

Existing literature that has focused on modeling the NaS batteries, uses considerably simpler models of the cell. Hussein and Cheung [46] developed an equivalent circuit model for a NaS battery where, the heat transfer characteristics of individual cells were not considered. For small power systems, Sarasua and Molina [47] developed a simple battery model to analyze the thermal behavior of NaS battery. Min and Lee [48] developed a steady state lumped thermal model for an entire cell, as well as a battery module. Aygun [49] incorporated a two-dimensional heat transfer model with an electrochemical model, which can be used as a computational design tool to calculate the two-dimensional distribution of temperature inside a NaS battery. Most of the papers cited above neglected the variation of thermo-physical properties with temperature. However, dynamic characteristics of the cell/battery are affected considerably by the varying thermo-physical properties with temperature. Therefore, correlations were developed in this paper to understand the cell performance under different ambient conditions.

Overall, there is a lack of studies in the open literature on detailed, non-isothermal dynamic model of the entire sodium sulfur cell by considering both the electrochemical as well as thermal phenomena using temperature-dependent correlations for thermophysical properties. Such models are very useful for studying the high current-density operations and large ramp rates as would be expected in grid-connected operations. As noted above, the operation of sodium sulfur cells at high current density with large ramp rates can cause cell performance loss due to lower sulfur utilization and lower energy efficiency. In addition, these demanding operations can result in undesired thermal runaway leading to potentially hazardous situations. The model developed in this work is

validated with the experimental data from the literature. The validated model is used to study the cell dynamics under various load-following conditions.

2.2. Model Development

The battery considered in this study consists of a central molten sodium electrode, beta"-alumina solid ceramic electrolyte, and an outer molten sulfur/sodium-polysulfide electrode as shown in Figure 2.1.

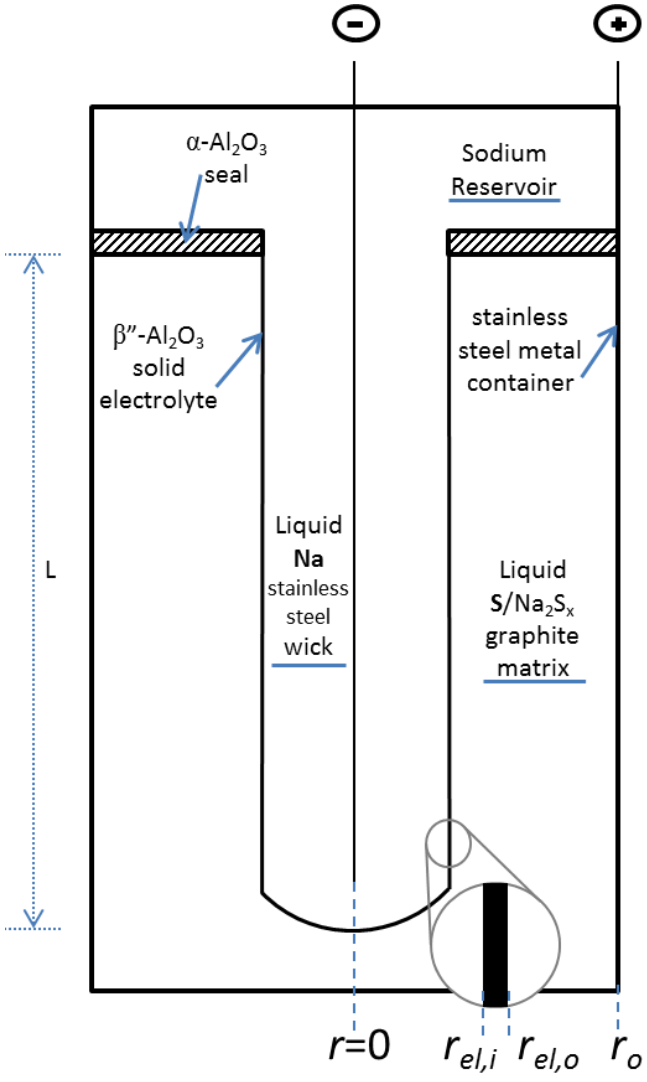

Figure 2.1. Schematic of a central sodium sulfur cell

The half-cell reactions that take place in the sodium and sulfur electrodes, respectively, are given by:

$$2Na \leftrightarrow 2Na^{+} + 2e^{-} \quad (2.1)$$

$$2Na^{+} + xS + 2e^{-} \leftrightarrow Na_2S_x \quad (2.2)$$

The overall cell reaction is given by:

$$2Na + xS \leftrightarrow Na_2S_x \quad (2.3)$$

where *x* is the variable subscript for sulfur in the sodium-polysulfide melt. The forward reaction takes place during cell discharge when the positive sodium ions move from the anode to the cathode through the beta"-alumina electrolyte. The beta"-alumina electrolyte is practically impermeable to electrons [31][50]. Sodium ions react with the liquid sulfur in the cathode to produce sodium polysulfides. Under fully charged condition, the sulfur electrode contains only sulfur. As discharge operation begins, the sulfur electrode transitions to a two-phase mixture of sulfur and polysulfide. As the reaction progresses, more sodium ions react with the sulfur and the mole fraction of total sulfur decreases. Composition of the sulfur electrode changes based on the amount of sodium that crosses the electrolyte. The sodium polysulfide composition in the melt is denoted by the subscript '*x*' in Reaction (3). The phase of the melt changes depending on the SOD of the cell since '*x*' changes depending on the SOD. At a mole fraction of about 0.729, the sulfur electrode becomes single-phase polysulfide until the melt reaches 0.571 mole fraction sulfur [37]. At this point the solid polysulfide Na_2S_2 begins to form and proper operation of the cell is no longer possible. Therefore, the cell is considered to be fully discharged when the sulfur electrode composition reaches Na_2S_3.

It is desired that the anode and cathode materials stay in the liquid phase for proper operation of the cell. The sodium sulfur battery usually operates between 300-400°C, at which temperature of the sodium, sulfur, and polysulfides (Na_2S_5-Na_2S_3) exist in the liquid phase [31]. The open circuit voltage of the cell at 350°C is 2.075 V [31]. The specific energy density of the battery reaches 760 Wh/kg at 350°C, nearly three times that of a lead acid battery [7].

The sodium electrode contains a stainless-steel wick that is in direct contact with the inner side of the beta"-alumina electrolyte, allowing for complete wetting of the electrolyte surface with liquid

sodium. The sulfur/sodium polysulfide melt is contained in a graphite matrix for better electron conduction in the sulfur electrode.

2.2.1. Model Assumptions

The following assumptions are made in developing the model:

- variation in the cell potential, temperature, and concentration gradients in the axial direction are negligible.
- Convective flux in the cell compartments is negligible.
- the supply of sodium to the sodium electrode is abundant over the entire range of operation assuming that a large reservoir for sodium is available.
- the sodium electrode/beta"-alumina electrolyte interface is always completely wetted.

2.2.2. Sulfur Electrode

The energy conservation equation for the sulfur electrode is given by:

$$\rho_{(S)} c_{p(S)} \frac{\partial T_{(S)}}{\partial t} - \frac{1}{r}\frac{\partial}{\partial r}\left(r\lambda_{(S)}\frac{\partial T_{(S)}}{\partial r}\right) = q_{(S)} \tag{2.4}$$

where $r, \rho, c_p, \lambda, T, t$, and q denote the radius, density, specific heat, thermal conductivity, temperature, time, and the heat source per unit volume for the sulfur electrode, respectively with the (S) subscript denoting sulfur electrode. Temperature-dependent correlation, equation A1 as shown in the Appendix A, has been developed for the thermal conductivity of sodium polysulfides and liquid sulfur using the data available in the open literature [22]. This correlation can be found in Table 2.1 and more information is provided under the Appendix A. Density and specific heat of the sulfur electrode are assumed to be constant as reported in Table 2.1 [22]. Additional information is provided under the Appendix A. The heat source term is given by:

$$q_{(S)} = Q_{Ohmic} + Q_{Entropy} \tag{2.5}$$

$$Q_{Ohmic} = \frac{1}{\sigma_{e(S)}}\left(\frac{I}{2\pi r L}\right)^2 \tag{2.6}$$

$$Q_{Entropy} = \frac{a_s}{K_p}\left(\varphi_{e(S)} - \varphi_{i(S)} - \mu\right)\left(T\frac{dE}{dT}\right) \tag{2.7}$$

Here, σ_e, a_s, K_p, φ_e, φ_i, μ, and dE/dT denote the electronic conductivity of the melt, surface area per unit volume of graphite matrix, the surface polarization resistance coefficient, electronic and ionic potential, local potential, and temperature dependence of open circuit voltage, respectively.

The term $(\varphi_{e(S)} - \varphi_{i(S)} - \mu)$ is called the overpotential, which changes sign depending on whether the cell charging or discharging. The values for electronic conductivity, surface area per unit volume, and polarization coefficient are obtained from the open literature [45]. The term(dE/dT), typically known as the entropy term, depends on the SOD [34]. The developed correlation between the entropy and SOD and its fit to the experimental data are shown in Equation A.2 and Figure A.2, respectively, under the Appendix A. The SOD is also a function of the melt composition as shown in Equation A3.

The local potential is given by the following equation:

$$\mu = \begin{cases} 2.05, & M \geq 0.710286 \\ \alpha_1 + \beta_1 X_e, & M < 0.710286 \end{cases} \tag{2.8}$$

Here, α_1 and β_1 are overpotential coefficients [51], M is the mole fraction sulfur, and X_e is the mole fraction 'electrolyte' (Na_2S) in the sulfur electrode [52][53]. The overpotential coefficients are functions of temperature, given by equation A4 and equation A5 as shown in Table 2.1. Additional explanation is provided under the Appendix A using Figure A.3. The mole fraction of sulfur is related to the mole fraction of electrolyte by:

$$X_e = 1/X_S \tag{2.9}$$

$$M = X_S/(2 + X_S) \tag{2.10}$$

where X_S is the value of the subscript x in Na_2S_x. The sodium ion conservation equation in the sulfur electrode is given by [45]:

$$\frac{\partial C_{+(S)}}{\partial t} = -\frac{1}{F}\frac{a_s}{K_p}(\varphi_{e(S)} - \varphi_{i(S)} - \mu) \tag{2.11}$$

where C_+ and F are the concentration of sodium ions and Faraday's constant. Charge conservation in the sulfur electrode leads to Equations 2.12 and 2.13 [52]:

$$-\sigma_{i(S)}\frac{\partial}{\partial r}\left(r\frac{d\varphi_{i(S)}}{dr}\right) + r\frac{a_s}{K_p}\varphi_{i(S)} = \frac{1}{3}FD_{(S)}\left(\frac{3t_+ - 1}{t_+(1-t_+)}\right)\frac{\partial}{\partial r}\left(r\frac{dC_{+(S)}}{dr}\right) + r\frac{a_s}{K_p}(\varphi_{e(S)} - \mu) \tag{2.12}$$

$$-\sigma_{e(S)}\frac{\partial}{\partial r}\left(r\frac{d\varphi_{e(S)}}{dr}\right)+r\frac{a_s}{K_p}\varphi_{e(S)}=r\frac{a_s}{K_p}(\varphi_{i(S)}+\mu) \tag{2.13}$$

Here, σ_i, D, and t_+ are the ionic conductivity, diffusion coefficient of sodium ions, and the transference number of sodium ions in the sulfur electrode, respectively. The ionic conductivity of the sodium polysulfide melt is a function of the mole fraction of sulfur in the melt [52][53] as shown in Table 2.1. The diffusion coefficient (Table 2.1) for sodium ions in the melt is a function of temperature and mole fraction of the electrolyte (Na_2S) in the melt [54]. The transference number (Table 2.1) of sodium ions is based on the overpotential coefficients β_1, β_3 and the mole fractiona of electrolyte as shown in Table 2.1 and is based on the experimental cells of Risch and Newman [51].

2.2.3. Beta"-Alumina Electrolyte

The energy conservation equation in the beta"-alumina solid electrolyte is given by:

$$\frac{\partial T_{(el)}}{\partial t}=\frac{1}{\rho_{(el)}c_{p(el)}r}\left(q_{(el)}r+\frac{\partial}{\partial r}\left(r\lambda_{(el)}\frac{\partial T_{(el)}}{\partial r}\right)\right) \tag{2.14}$$

where ρ and c_p denote the density and specific heat capacity of the electrolyte respectively, with subscript denoting the beta-alumina electrolyte. The temperature-dependent correlation for density is determined based on the thermal expansion coefficient and is shown in Table 2.2. The density is given by equation A7 in the Appendix A, where additional information is provided. The thermal expansion coefficient is given by Sudworth and Tilley [22]. The specific heat capacity and thermal conductivity of the electrolyte are also functions of temperature [55] as shown in Table 2.2.

The heat source term $q_{(el)}$ (W/m^3) in the electrolyte is mainly due to Ohmic heat loss and is given by:

$$q_{(el)}=\frac{J^2}{\sigma_{i(el)}} \tag{2.15}$$

where J is the current density. Sodium ion conduction in beta"-alumina electrolyte is mainly due to the ionic conductance and ion migration.

Table 2.1. Additional Equations for Sulfur Electrode

Variable Notation	Equation/ Value	Units	Reference/ Comments
$\lambda_{(S)}$	$0.4813 - 1.8648 \times 10^{-3} T_{(S)} + 2.4844 T_{(S)}^2$	W/mK	[22]
$\rho_{(S)}$	1880	kg/m^3	[22]
$c_{p(S)}$	1315	J/kgK	[22]
$\sigma_{e(S)}$	50	A/V	[45]
a_s	$a_{s0}(1 - p_{(S)}) \begin{cases} \times 1, & X_S < 5.24 \\ \times (5.24/X_S), & X_S > 5.24 \end{cases}$	m^2/m^3	[45]
$p_{(s)}$	0.35	-	[56]
a_{s0}	1×10^4	m^2/m^3	[45]
K_p	1×10^{-4}	Ω/m^2	[45]
$T\frac{dE}{dT}$	$-15.536(SOD)^5 + 32.652(SOD)^4 - 22.969(SOD)^3 + 6.0576(SOD)^2 - 0.5629(SOD) - 0.0362$	V	This work
α_1	$(-8.1667 \times 10^{-5})(T_{(S)}) + 2.5087$	V	[51]
β_1	$(-7.350 \times 10^{-4})(T_{(S)}) - 1.5600$	V	[51]
β_3	$(3.0783 \times 10^{-3})(T_{(S)}) + 0.0472$	V	[51]
X_s	$(2/C_+)(W_s/32)(1/V_{(S)})$	-	[52][53]
F	9.6487×10^7	C/kmol	Faraday's constant
t_+	$(-\beta_3/\beta_1 - X_e)/(1 - X_e)$	-	[51]
$\sigma_{i(S)}$	$\sigma_{i0(S)}(1 - p_{(S)})$	A/V	[52][53]
$\sigma_{i0(S)}$	$\begin{cases} -457.04M + 657.04, & M \geq 0.72 \\ -242.99M + 207.75, & 0.60 > M > 0.72 \\ 61.956, & M \leq 0.60 \end{cases}$	1/ohm.m	[52][53]
$D_{(S)}$	$(1.53 \times 10^{-6}) exp\left(-8590/T_{(S)}\right) exp\ (5.30X_e)$	m^2/s	[54]
SOD	$\begin{cases} -343.55M + 304.82, & single\ phase\ polysulfide \\ -202.43M + 202.23, & two\ phase\ sulfur/polysulfide \end{cases}$	Ah(max)/Ah	This work

('contd.)

$V_{(S)}$	9.5425×10^{-5}	m^3	-
α	30	W/m^2K	[22]
ϵ	0.066	-	[36][57]
δ	5.67×10^{-8}	W/m^2K^4	Stefan-Boltzmann constant
W_s	0.1	kg	[45]

The sodium ion conservation in the electrolyte is given by:

$$\frac{\partial C_{+(el)}}{\partial t} = \frac{D_{(el)}}{p_{(el)}} \frac{1}{r} \frac{\partial}{\partial r}\left(r \frac{\partial C_{+(el)}}{\partial r}\right) \tag{2.16}$$

where p is the porosity of the beta"-alumina electrolyte. The correlation for porosity is proposed as shown in Table 2.2. The equation is based on the theoretical and calculated density of sodium beta"-alumina, and describes it as a function of temperature, as shown in Equation A8. More details about the correlation can be found in the Appendix A.

Conservation of positive ions in the electrolytes is written by considering ion transport by both diffusion and migration:

$$-\sigma_{i(el)} \frac{\partial \varphi_{i(el)}}{\partial r} - F D_{(el)} \frac{\partial C_{+(el)}}{\partial r} = J \tag{2.17}$$

The ionic conductivity, σ_i, and diffusion coefficient, D, are functions of temperature, as shown in Table 2.2. More information about these variables can be found in the Appendix A, where the equation for ionic conductivity is given by Equation A9 and for diffusion coefficient is given by Equation A10.

2.2.4. Sodium Electrode

The energy conservation for the sodium electrode can be written as:

$$\left(m_{ss} c_{p,ss}\right) \frac{\partial T_{(Na)}}{\partial t} + \left(m_{Na} c_{p,Na}\right) \frac{\partial T_{(Na)}}{\partial t} = q_{(Na)} + \left(2\pi r_{el,i} L \lambda_{(el)}\right) \frac{\partial T_{(el)}}{\partial r}\Big|_{r=r_{el,i}} \tag{2.18}$$

where m is the mass and c_p is the specific heat, with subscripts ss and Na denoting the stainless steel wick and the liquid sodium in the sodium electrode.

Table 2.2. Additional Equations for Beta"-Alumina Electrolyte

Variable Notation	Equation/ Value	Units	Reference/ Comments
$\lambda_{(el)}$	$2.451 + 2.456 \times 10^{-4}(T_{(el)}) - 6.178 \times 10^{-7}(T_{(el)})^2 + 4.275 \times 10^{-10}(T_{(el)})^3 - 6.993 \times 10^{-14}(T_{(el)})^4$	W/mK	[55]
$\rho_{(el)}$	$3220\, exp\left(-3\alpha_L\left(T_{(el)} - 25\right)\right)$	kg/m^3	[22]
$c_{p,(el)}$	$0.7321 + 5.006 \times 10^{-4}(T_{(el)}) - 2.151 \times 10^{-7}(T_{(el)})^2$	J/kgK	[55]
$D_{(el)}$	$D_0 exp\left[-H/(RT_{(el)})\right]$	m^2/s	[58]
$p_{(el)}$	$(3220 - \rho_{(el)})/3220$	-	[22]
$\sigma_{i(el)}$	$(\sigma_{0(el)}/T_{(el)})exp\left[-H/(RT_{(el)})\right]$	1/ohm.m	[58]
$\sigma_{0(el)}$	1.49×10^6	K/Ωm	[58][59]
H	5.497	kcal/mol	[58] [59]
α_L	7.5×10^{-6}	K^{-1}	[22]
p_t	1.8×10^{-4}	V/K	[60]
D_0	3.98×10^{-8}	m^2/s	[58]
H	5.497	kcal/mol	[58][59]

Specific heats are functions of temperature as shown in Table 3. They are given by Equations A11 and A12, respectively, in the Appendix A, and explained in Figure A4. The heat source term, $q_{(Na)}$, for the sodium electrode considers the Ohmic heat loss at the interface of the electrolyte,

$$q_{(Na)} = \frac{I^2 \rho_{l(Na)} r_{el,i}}{2\pi(r_{el,i}/2)L} \tag{2.19}$$

where $\rho_{l(Na)}$ is the resistivity of liquid sodium. The resistivity of liquid sodium is a function of temperature [22], as shown in Table 2.3. The concentration of sodium ions at the beta"-alumina interface is given by:

$$\frac{\partial C_{+(Na)}}{\partial t} = \frac{-I}{FV_{(Na)}} \tag{2.20}$$

where V is the volume of the sodium electrode, including the molten sodium, the wick, and the reservoir. The ionic potential drop in the sodium electrode is given by:

$$\varphi_{i(Na)} = -\eta_{(Na)} \tag{2.21}$$

where $\eta_{(Na)}$ is the linear current potential relationship shown in Table 2.3 is derived from Butler-Volmer kinetics. No electronic potential change is considered in the sodium electrode.

Table 2.3. Additional Equations for Sodium Electrode

Variable Notation	Equation/ Value	Units	Reference/ Comments
m_{Na}	0.057	kg	[45]
m_{ss}	20.3	kg	[22], linearly scaled to cell dimensions
$c_{p,ss}$	$-4.591 \times 10^{-4}\left(T_{(Na)}\right)^2 + 0.4813(T_{(Na)}) + 444.99$	J/kgK	[22]
$c_{p,Na}$	$1437.08 - 0.58063(T_{(Na)}) + 4.624 \times 10^{-4}(T_{(Na)})^2$	J/kgK	[22]
$\rho_{l(Na)}$	$6.87 \times 10^{-8} + 2.44 \times 10^{-10} T_{(Na)} + 2.67 \times 10^{-13}(T_{(Na)})^2 + 1.07 \times 10^{-15}(T_{(Na)})^3 - 2.67 \times 10^{-18}(T_{(Na)})^4$	Ohm.m	[22]
$V_{(Na)}$	2×10^{-3}	m^3	[45]
$\eta_{(Na)}$	$(IRT_{(Na)})/(2\pi r_{el,i} L i_0 F)$	W/m^3	This work
i_0	5×10^4	A/m^2	[61]

2.2.5. Boundary Conditions

Table 2.4 lists the boundary conditions based on the following assumptions:

- The Peltier heat is released at the electrolyte-sulfur electrode interface.
- There is no loss of ions through the metal container boundary of the cell.
- Heat is lost to the surroundings from the outer wall of the metal container by both convective and radiative heat transfer mechanisms.

Table 2.4. Boundary Conditions

Number	Location	Boundary Condition
Sodium Electrode (*Na*) / Beta"-Alumina Electrolyte (*el*):		
BC1	$r = r_{el,i}$	$C_{+(Na)} = C_{+(el)}$
BC2	$r = r_{el,i}$	$T_{(el)} = T_{(Na)}$
BC3	$r = r_{el,i}$	$\varphi_{i(el)} = -\eta_{Na}$
Beta"-Alumina Electrolyte (*el*) / Sulfur Electrode (*S*):		
BC4	$r = r_{el,o}$	$C_{+(el)} = C_{+(S)}$
BC5	$r = r_{el,o}$	$T_{(el)} = T_{(S)}$
BC6	$r = r_{el,o}$	$-\lambda_{(el)} 2\pi r_{el,o} L \frac{\partial T_{(el)}}{\partial r} = -\lambda_{(S)} 2\pi r_{el,o} L \frac{\partial T_{(S)}}{\partial r} \pm I p_t T_{(S)}$
BC7	$r = r_{el,o}$	$-\sigma_{i(el)} \frac{\partial \varphi_{i(el)}}{\partial r} - F D_{(el)} \frac{\partial C_{+(el)}}{\partial r} = J$
BC8	$r = r_{el,o}$	$-\sigma_{i(S)} \frac{\partial \varphi_{i(S)}}{\partial r} - F D_{(S)} \frac{\partial C_{+(S)}}{\partial r} = J$
BC9	$r = r_{el,o}$	$\varphi_{i(el)} = \varphi_{i(S)}$
BC10	$r = r_{el,o}$	$\frac{\partial \varphi_{e(S)}}{\partial r} = 0$
Sulfur Electrode (*S*) / Metal Container:		
BC11	$r = r_o$	$\frac{\partial C_{+(S)}}{\partial r} = 0$
BC12	$r = r_o$	$\frac{\partial T_{(S)}}{\partial r} + (\frac{\alpha}{\lambda_{(S)}})(T_{(S)} - T_{air}) + (\frac{\epsilon \delta}{\lambda_{(S)}})(T_{(S)}^4 - T_{air}^4) = 0$
BC13	$r = r_o$	$\frac{\partial \varphi_{i(S)}}{\partial r} = 0$
BC14	$r = r_o$	$\varphi_{e(S)} = \varphi_0$ so as to satisfy: $I = -2\pi L \int_{r_{el,o}}^{r_o} (\frac{a_s}{K_p})(\varphi_{e(S)} - \varphi_{i(S)} - \mu) r dr$

2.3. Results and Discussion

The model is developed in Aspen Custom Modeler® V.8.4. and solved using method of lines.

2.3.1. Model Validation

The model of the 80 Wh cell is validated at various current density operations and states of discharge/charge with the experimental data from the open literature [44][45]. Dimensions of the experimental cell are given in Table 2.5.

Table 2.5. Cell Dimensions

Parameter	Value	Units
L	0.18	m
$r_{el,i}$	0.0069375	m
$r_{el,o}$	0.0075	m
r_o	0.015	m
T_{air}	330	°C
$V_{(Na)}$	2×10^{-3}	m^3
$V_{(S)}$	9.5425×10^{-5}	m^3

Figure 2.2 shows model validation for charging and discharging when the total amount of the current from/to the cell is 3 A, 6 A, and 9 A, corresponding to the current density of 35.4 mA/cm^2, 70 mA/cm^2 and 106 mA/cm^2, respectively.

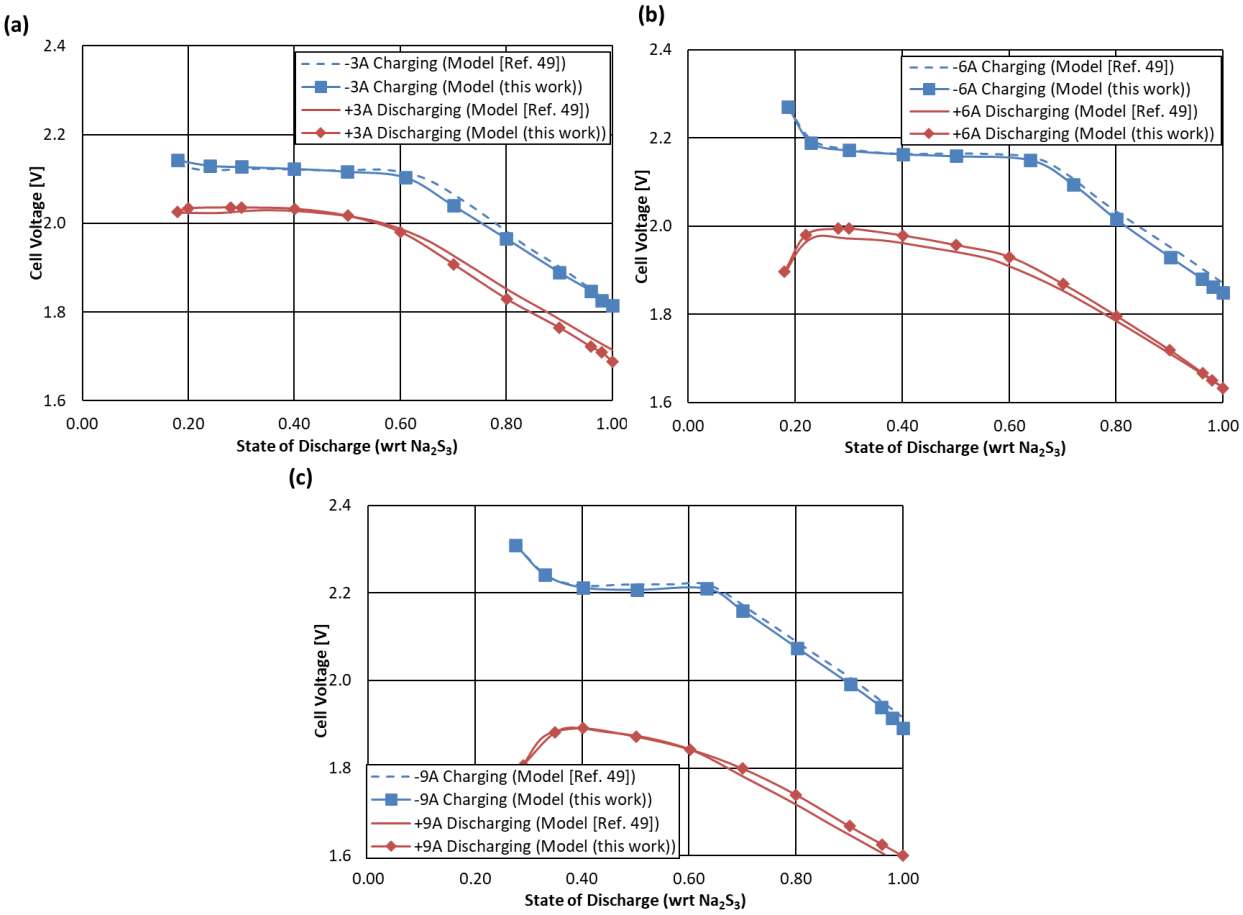

Figure 2.2. Comparison between model results and experimental data from Kawamoto [45] for cell voltage vs SOD for an ambient temperature of 335°C and during discharging/charge at (a) +/-3A corresponding to a current density of 35.4 mA/cm^2, (b) +/-6A corresponding to a current density of 70 mA/cm^2 and (c) +/-9A corresponding to a current density of 106 mA/cm^2

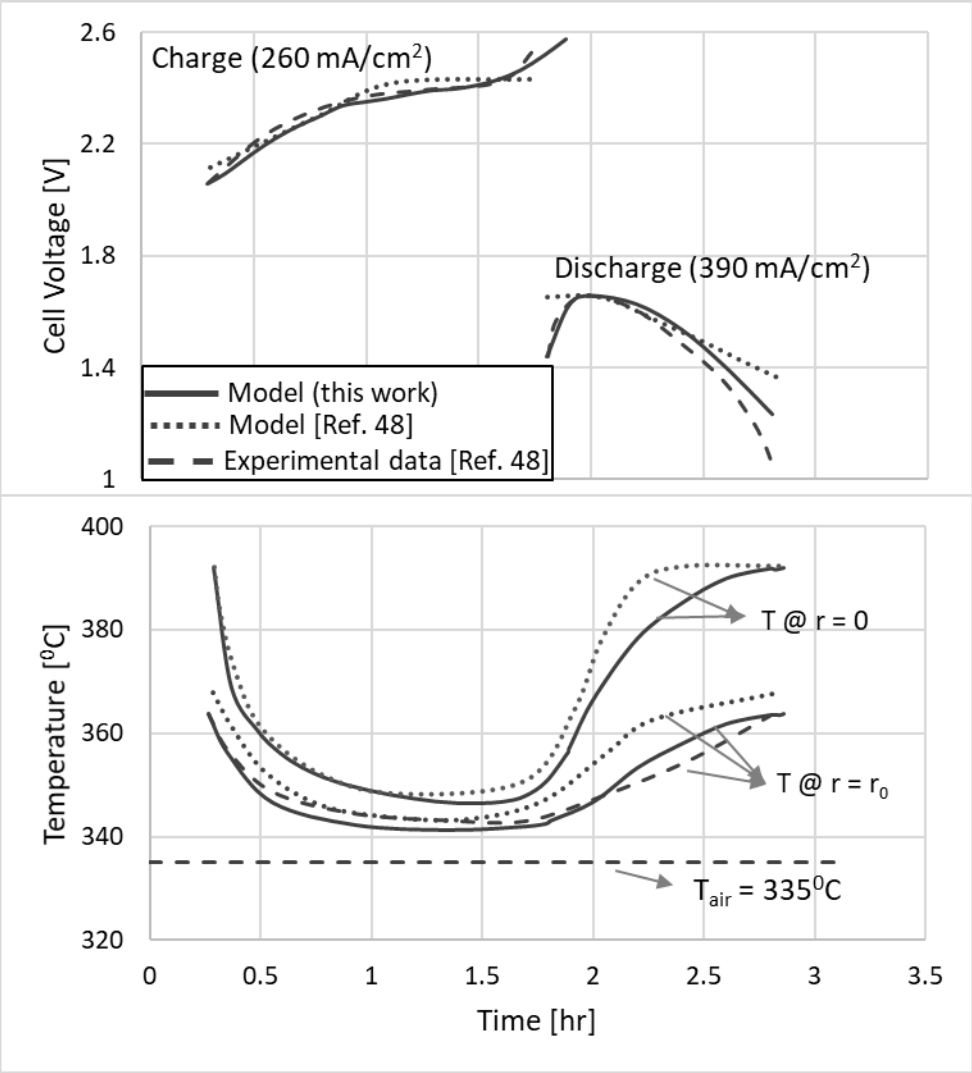

Figure 2.3 Comparison between results from the model developed in this work, results from the model developed by Kawamoto and Kusakabe [44] and experimental data [44] for cell voltage and temperature at the surface and center (only model results compared as no experimental data available) of the cell at 335°C ambient temperature and corresponding to the current density of 260 mA/cm^2 during charging and 390 mA/cm^2 during discharging.

The results from the model for both charging and discharging compare well with the experimental data as shown in Figure 2.2. During charging, the root- mean-square error (RMSE) for voltage is ~0.055 V, ~0.066 V, and ~0.041 V, at 3 A, 6 A, and 9 A, respectively. During discharging, the RMSE is ~0.0136 V, ~0.0356 V and ~0.0293 V at 3 A, 6 A, and 9 A, respectively. During discharging, the cell voltage is nearly constant when the operation is in the two-phase region

(<55% SOD), and then decreases as the SOD increases further. During charging, the cell begins in the single-phase region at the sulfur electrode and the voltage continues to increase and becomes nearly constant once the melt is in the two-phase region. Similar to the observations of Kawamoto [37], inflections are found to occur at lower SOD. As the current density increases, there is a relative increase in the SOD at which the inflection occurs. The main reason for this is the steep concentration gradient near the sulfur electrode-electrolyte interface at lower SOD as shown in Figure 2.4.

Kawamoto and Kusakabe [44] have reported experimental data of the voltage and cell outer surface temperature profiles for high current density operation. Kawamoto and Kusakabe [44] have also shown comparison of their model results with those experimental data. Figure 2.3 shows the comparison between results from the model developed in this work, results from the model developed by Kawamoto and Kusakabe [44] and the experimental data [44] for cell voltage and temperature at the surface. There were no experimental data available for the temperature of the cell center so only results from both the models are compared. The experimental data correspond to an ambient temperature of 335°C and the current density of 260 mA/cm^2 during charging and 390 mA/cm^2 during discharging. Root mean square error (RMSE) between the model developed here and the experimental data [44] as well as the model developed by Kawamoto and Kusakabe [44] and the experimental data [44] is shown in Table 2.6. It is observed from Figure 2.3 and Table 2.6 that that results from both models for the voltage profile compare well with the experimental data during charge. However, during discharging the results from this model for the voltage profile is considerably closer to the experimental data than that of Kawamoto and Kusakabe [44]. RMSE values from both models for the temperature profile is similar during charging, but the results for the temperature profile during discharging compare better with the experimental data than that of Kawamoto and Kusakabe [44]. The study also shows that even though the ambient temperature is held constant at 335^{o}C, the high current density operation leads to a temperature that is very close to the maximum temperature limit of 400^{o}C typically considered to be safe for sodium-sulfur cells. Since temperature of the cell at the center may be difficult to be measured in real life, a non-isothermal model can be very useful to avoid unsafe operation of the cell. To this end, one operational strategy can be to vary the current density of a given cell to maintain the cell temperature within the limit. This strategy is discussed in detail in Section 2.3.4.3.

Table 2.6. Root mean square error (RMSE) values between models and experimental data [44]

	Between Model developed in this work and the experimental data [44]	Model developed by Kawamoto and Kusakabe [44] and their experimental data [44]
Voltage (Charging)	~0.023 V	~0.036V
Voltage (Discharging)	~0.078 V	~0.098 V
Temperature (Charging)	~2.1^{o}C	~2.5^{o}C
Temperature (Discharging)	~3.3^{o}C	~5.2^{o}C

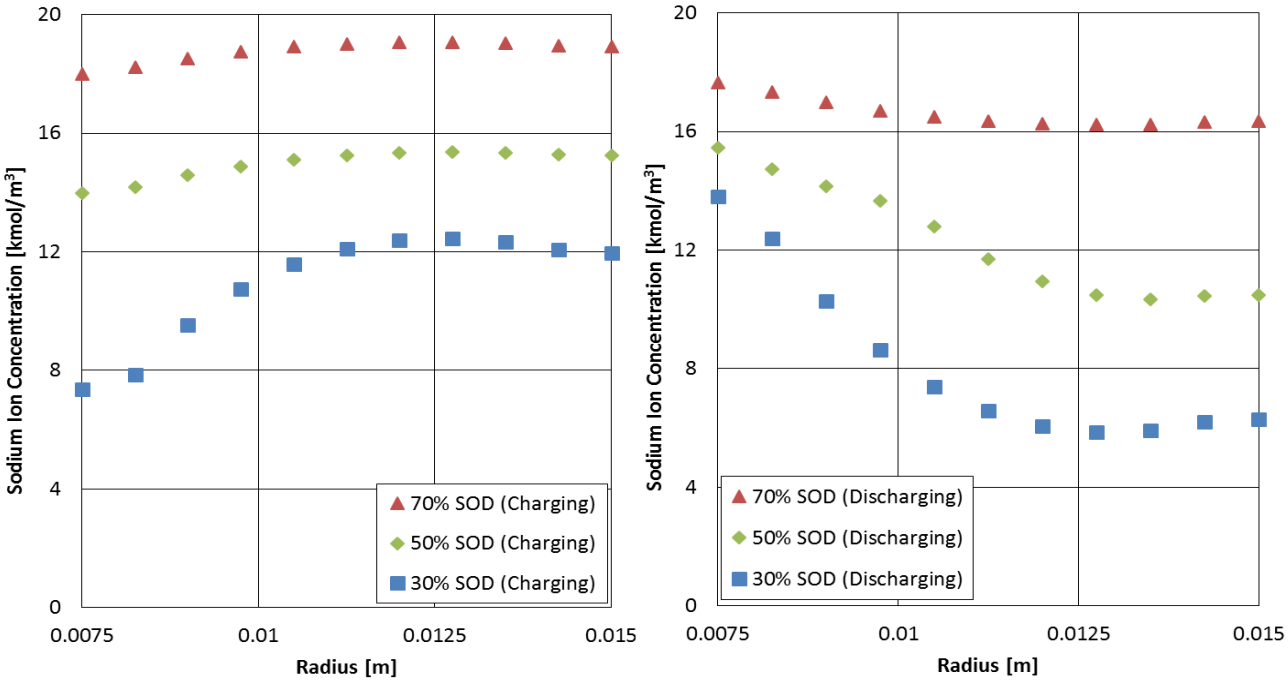

Figure 2.4. Sodium ion concentration profile in the location between sodium/electrolyte interface to sulfur electrode during charging/discharge at ±6A at 70% SOD, 50% SOD and 30% SOD, respectively at 330°C ambient temperature.

2.3.2. Concentration distribution

As mentioned, when the cell discharges, the concentration of sodium ions in the beta"-alumina electrolyte and sulfur electrode increases, moving from the two-phase region (S, Na_2S_x) to the single-phase region (Na_2S_x). The electric conduction characteristics differ between these two regions. The overpotential term in Equation (2.11) alters sign as the cell switches from charging to discharging, which results in an overall increase in the sodium ion concentration during charging while a decrease during discharging as seen in Figure 2.4. In addition, at the electrolyte/sulfur electrode interface, as SOD increases the Na ion concentration increases.

In the single-phase region, diffusion due to the concentration gradient is negligible i.e., the electric conduction is dominated by migration. As stated in Section 2.2, the sulfur electrode becomes single phase when the sulfur mole fraction becomes about 0.729 and remains as a single phase until the sulfur mole fraction reaches 0.571. It can be observed form Equation (2.8) that in this region the local potential increases during charging due to the increase in overpotential coefficients that depend on the temperature. This affects the overpotential, which leads to an increase in the concentration gradient of sodium ions in the single-phase region during charging. As seen in Figure 2.4, when the SOD decreases, sodium ion concentration at the cathode becomes much smaller than at the anode thus the driving force term in the diffusive flux (Equation 2.12) changes sign. Thus, at the lower SOD, transport of sodium ions from the cathode to the anode needs an increasingly higher potential for overcoming the opposing concentration gradient that keeps rising. This leads to the steep rise in the voltage at lower SOD while charging. However, in the two-phase region the local potential is constant (Equation (2.8)), which results in nearly constant cell voltage. The voltage characteristics under discharging condition can be explained in a similar manner.

2.3.3. Temperature Distribution

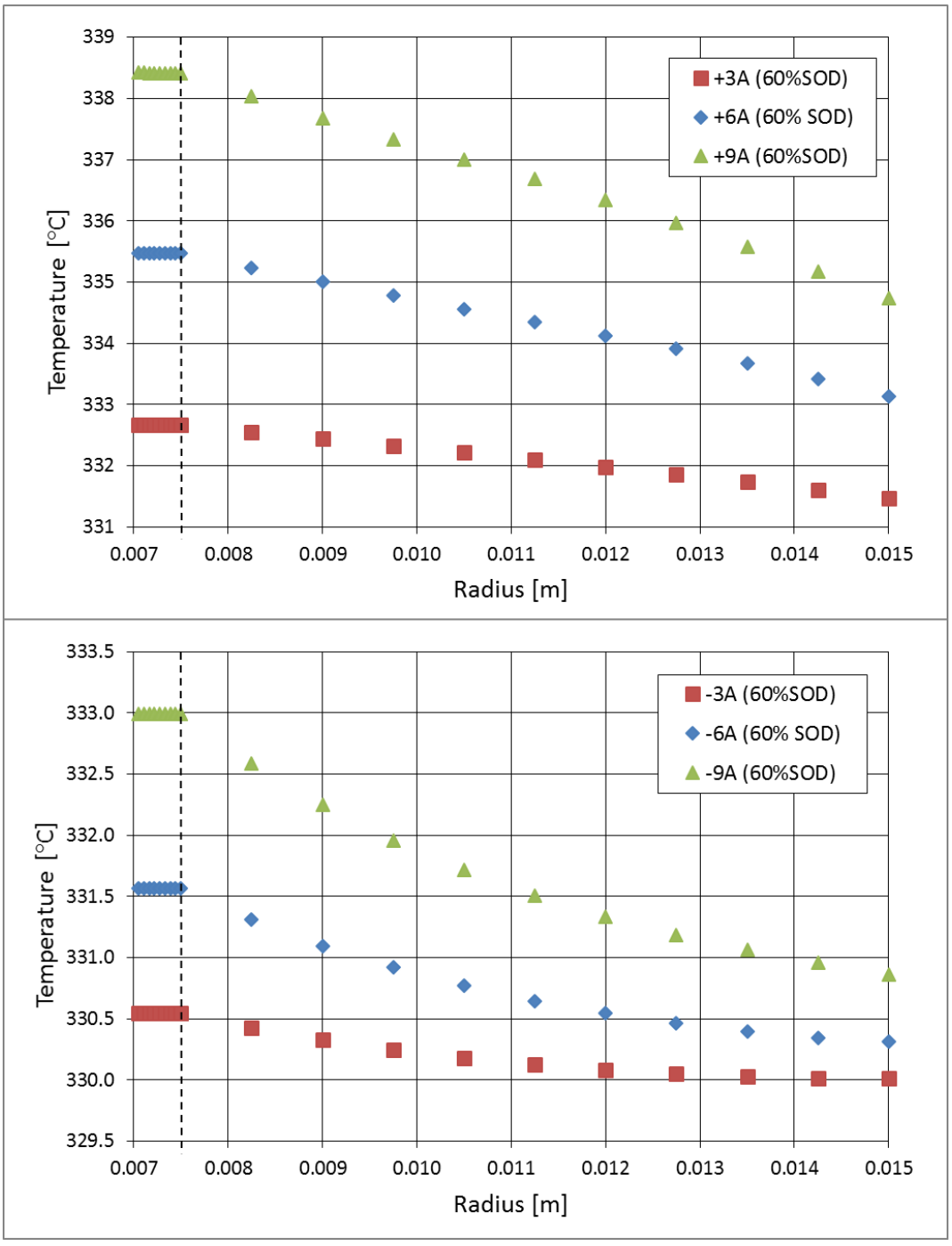

Figure 2.5. Temperature profile in the cell during discharging and charge at 60% SOD for 3A, 6A and 9A current, respectively (corresponding to 35.4 mA/cm^2, 70 mA/cm^2 and 106 mA/cm^2 current density, respectively) for the ambient temperature of 330°C (vertical dotted line represents the electrolyte/ sulfur electrode interface).

The temperature profiles within the cell at 60% SOD during discharging and charge is shown in Figure 2.5. The ambient air temperature was maintained at 330°C. The dotted line in the graph represents the electrolyte/ sulfur electrode interface. As expected, higher current density operation results in higher temperatures within the cell. It can also be observed that there is a greater temperature increase during discharging than during charging. This is due to the electro-chemical reactions that take place in the sulfur electrode, which are exothermic during discharging and endothermic during charging. The temperature difference between the center of the cell and ambient conditions is nearly 3 times greater during discharging than charge. It should be noted that this creates a mismatch in heat generated during discharging and charge. Therefore, for maintaining the same cell temperature during charging and discharge, the heat removal rate should be different between charging and discharging even at the same SOD and same current density.

2.3.4. Impact of Key Operating Conditions

Operating conditions can affect the dynamics of the NaS cell. First, the impact of different environment temperatures is evaluated. Second, the transient response of the cell at higher current density operation is studied. Dynamic responses of the cell under various load demands are also studied.

2.3.4.1. Impact of the Cell Environment's Temperature

For the experimental cell of Kawamoto and Kusakabe [44] and Kawamoto [37], the furnace air temperature was controlled. During real-life operation of large number of cells as in a battery, this ambient temperature is expected to vary depending on the thermal management strategy. Figure 2.6 shows the cell voltage profile for different ambient temperatures.

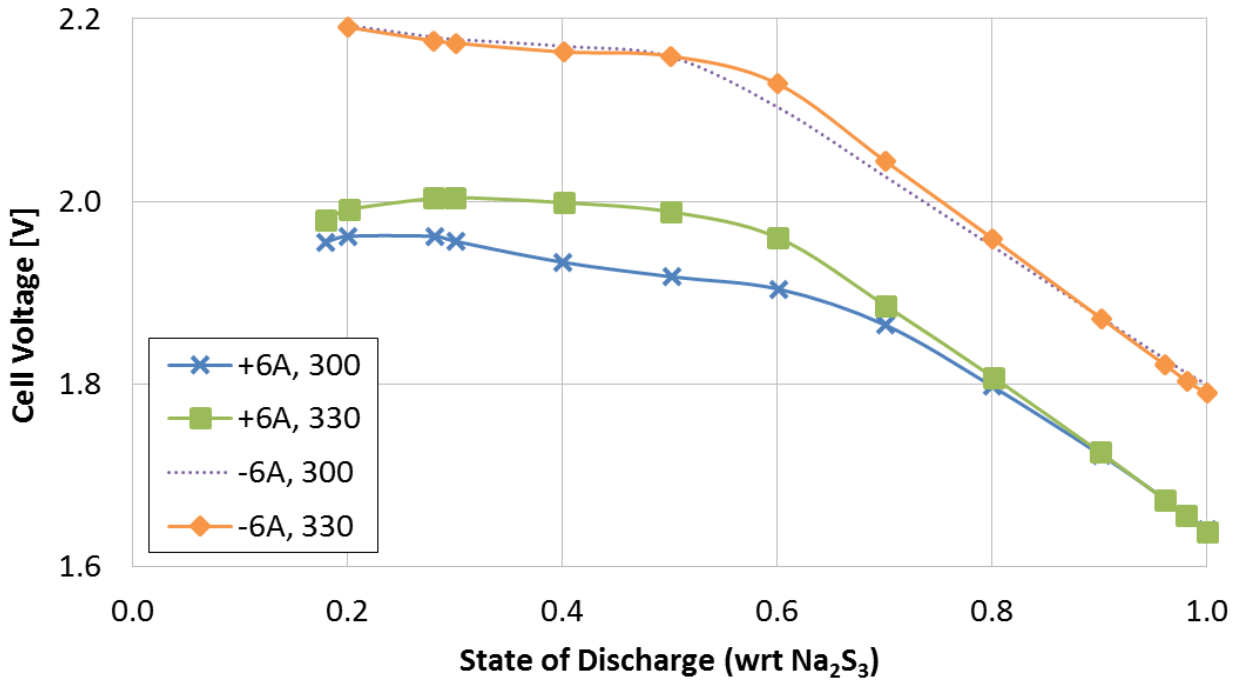

Figure 2.6. Cell voltage vs SOD during discharging/charge at 300°C and 330°C ambient temperature for a current density of 70 mA/cm^2.

It is observed that the cell voltage profile is practically unaffected by the temperature under charging conditions whereas during discharging the cell voltage profile improves with the increase in the temperature. During charging as the cell approaches fully charged condition, the concentration of sulfur at the cathode/electrolyte interface keeps growing thus resulting in a higher cell resistance [39][45] or lower ionic conductivity. Since ionic resistance becomes the limiting mechanism during charging and the ionic conductivity is not affected directly by the cell temperature as can be observed in Table 2.1, an increase in the ambient temperature has negligible impact during charging. However, during discharging, the limiting mechanism for a large range of SOD is the reaction overpotential and the reaction overpotential is strongly affected by the temperature as seen by Eq. (2.8) and the corresponding correlations for α_1 and β_1 in Table 2.1, the cell voltage profile improves during discharging as the ambient temperature is increased. Considering the entire discharge cycle shown in Figure 2.6, the cell energy efficiency during discharging is about 91.92% at 330°C compared to about 90.63% at 300°C. It should be noted that while operation at higher temperatures can improve the cell efficiency, there is higher risk of fire

hazard especially under high current density operation and rapid load changes as expected in grid-connected systems.

2.3.4.2. Impact of High Current Density Operation

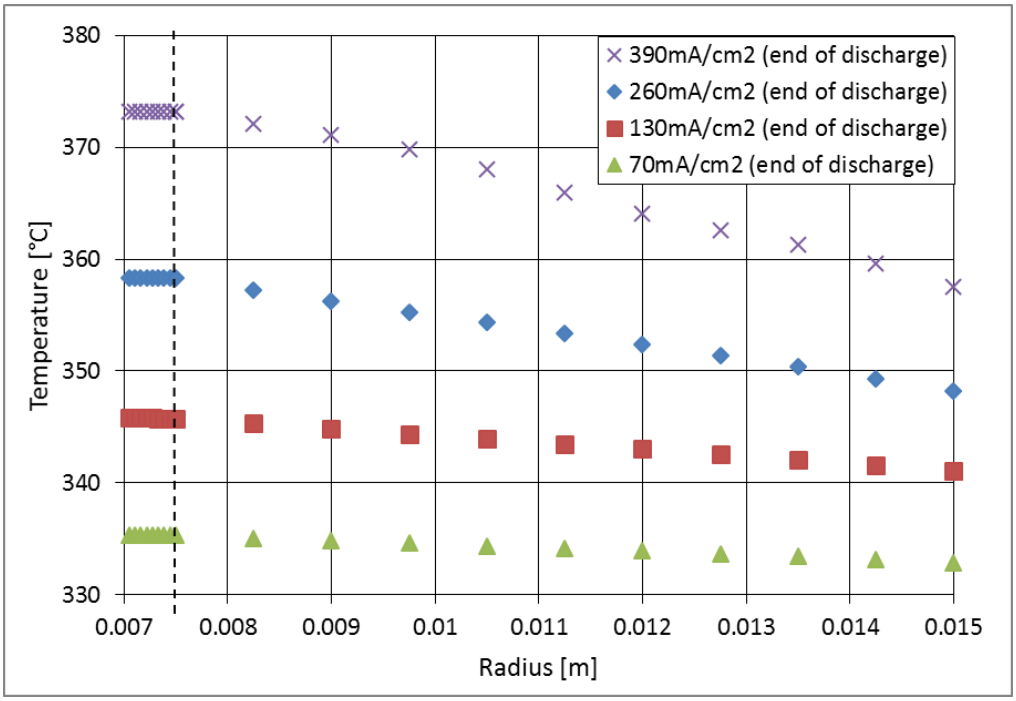

Figure 2.7. Temperature profile in the cell at 70 mA/cm^2, 130 mA/cm^2, 260 mA/cm^2 and 390 mA/cm^2 current density, respectively, at 330°C ambient temperature (vertical dotted line represents the electrolyte/ sulfur electrode interface).

For a grid connected battery, high current density operation would be expected at certain time instants when the differences between demand and supply of electric power is very high. It is desired to study the impact of high current density operation on the cell temperature since increasing temperature can lead to a fire hazard. Figure 2.7 shows the temperature profile within the cell at the end of discharge as the current density is changed while the ambient temperature is held constant at 335°C. At high current density (390 mA/cm^2) operation, where the cell generates 33 A, the maximum cell temperature is about 38°C higher in comparison to the maximum cell temperature when the current density is 70 mA/cm^2 generating 6A. The difference between the maximum and minimum temperature at 390 mA/cm^2 current density in the cell is almost 1.5 times that compared to the cell operating under a current density of 260 mA/cm^2 and almost 3 times more compared to a cell operating under a current density of 130 mA/cm^2 and almost 6 times more

compared to a cell operating under a current density of 70 mA/cm^2. These results show that for safe operation of the cell under high current density operation, a model-based approach can be valuable for monitoring and control since it is difficult to measure the temperature inside the cell in general.

2.3.4.3. Impact of change in the Current Density

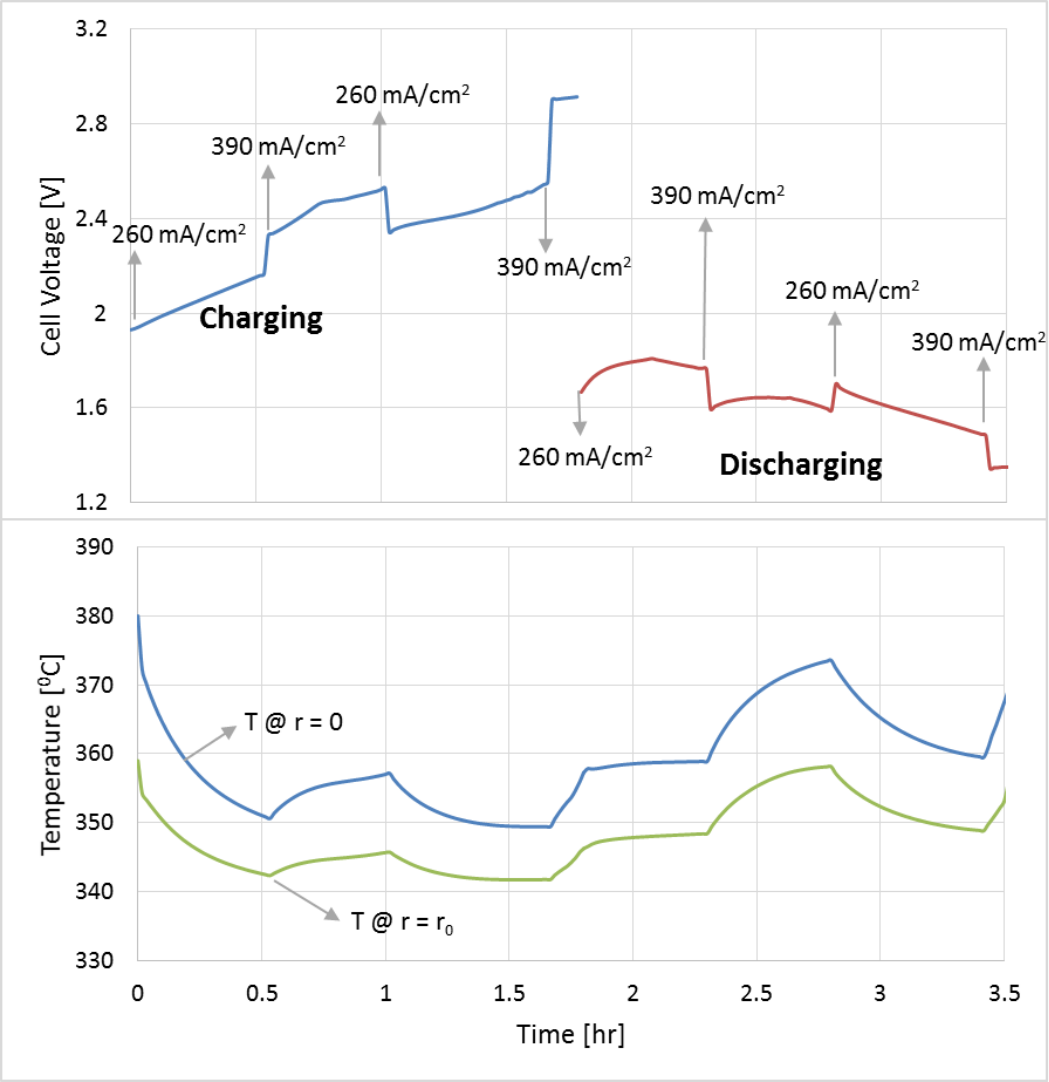

Figure 2.8. Transient response of the cell voltage and temperature at the center and surface during discharging and charge for an ambient temperature of 335°C.

Figure 2.8 shows the transient response of cell voltage and temperature at the center and surface for high current density operation. It is observed that when higher current is drawn from the cell even at a similar OSD, the cell voltage decreases. The reverse happens during charging.

Corresponding impact in the temperature profile can also be observed in Figure 2.8. Note that the initial decrease in the temperature till about 0.5 hr is due to the arbitrary initial temperature of the cell that is considered. As the current density is increased during charging at 0.5 hr, the temperature at both locations starts increasing. As the current density is decreased at 1 hr, both temperature starts decreasing. Similar behavior can be observed during discharging as well, i.e. temperature starts increases as the current density is increased and vice versa. The behavior shows how the current density may be manipulated to ensure the cell remains within the safe operating limit. Since the highest temperature of the cell is at the center, a transient non-isothermal model can be useful to monitor that temperature and limit current density or regulate current density, if needed, to avoid unsafe operation.

2.4. Conclusions

A non-isothermal, transient model of the entire NaS cell with beta”-alumina electrolyte was modeled. The dynamic model was validated for various current density operations over SOD. The results from the model were found to agree well with the experimental data. It was observed that cell voltage profile can change considerably depending on the SOD, current density, temperature profile and whether the cell is charging or discharging. Inflection in the cell voltage profile was observed as the cell transitions from a single phase to a two-phase region. The inflection point is found to shift based on the current density. As the SOD decreases, sodium ion concentration at the cathode becomes much smaller than at the anode. Therefore, at the lower SOD, a higher potential is needed for transport of sodium ions from the cathode to anode to overcome the opposing concentration gradient. The higher cell temperature during discharging was observed because of the mismatch between the rates of heat generated during charging and discharging, due to the exothermic electrochemical reactions during discharging. It was observed that operating the cell at higher temperature can improve the cell efficiency. However higher temperature operation increases the risk of fire and therefore a proper thermal management strategy is desired. Changing the ambient temperature did have minor effect on the cell voltage during charging but improved the cell voltage profile during discharging. It was also observed that the current density can affect the cell voltage even at the same SOD. This aspect can be exploited for the battery power management.

It was observed that as the current density is increased, there is significant increase in the cell temperature. At the high current density operation considered in this study, the maximum temperature in the cell that occurs at the Na electrode is about 28°C higher than the environment temperature. Thus, the study shows that if the cell environment temperature is maintained at a fixed value, it can lead to fire hazard for very high current density operation as would be expected for a grid-connected system. The study suggests two possible thermal management strategies: lowering the environment temperature, limit the current density to an upper limit depending on the environment temperature. However, as the cell produces very different amount of heat depending on whether it is charging or discharging and the current density, the thermal management approach must be able to remove variable amount of heat as well to maintain the cell temperature within a desired range.

The model presented here can be readily extended to room temperature NaS cells especially for studying the deviation in spatial and temporal temperature profile of those cells from the room temperature under charging/discharging conditions and how the deviation affects the cell efficiency and performance.

The model presented here can also be extended to Li-S cells. In Li-S cells, the anode and the electrolytes are quite different than the Na-S cells. Even though there are certain differences between the cathodes of these two types of cells including the differences in the specific energy density, lowest state of sulfur that the cell can be discharged into, volumetric change during reaction, degradation mechanisms, to name a few, cathode reactions and electronic and ionic transport mechanisms are similar. Therefore, the model of the sulfur electrode presented here can be a very good starting point for modeling the cathode of the Li-S cells.

Chapter 3. Development of Model-Based Thermal Management Strategies for High-Temperature Sodium Sulphur Batteries for High Current-Density Operation

3.1. Literature Review

The basic principle of operation for the sodium sulfur battery (NaS), is the electrochemical reaction between molten sulfur and molten sodium electrodes separated by a beta-alumina electrolyte. This results in high energy density, high open circuit voltage and an inexpensive battery system suitable for large scale grid-level energy storage applications [31][32]. Based on the operating temperature, NaS cells are categorized into three types. i) Room temperature sodium sulfur battery (RT-NaS) operating at 25 $^{\circ}$C to 60 $^{\circ}$C, ii) Intermediate temperature sodium sulfur battery (IT-NaS) operating at 150 $^{\circ}$C to 200 $^{\circ}$C and iii) High temperature sodium sulfur battery (HT-NaS) operating at 300 $^{\circ}$C to 400 $^{\circ}$C [26][33][34][35]. Currently, RT-NaS batteries have a low-capacity retention and poor cycling properties which compromises the stability of the cell [26][35]. IT-NaS batteries also have limitations in the chemistry and solubility of sodium polysulfides resulting in low cell conductivity [26]. In general, lowering the operating temperature of the NaS batteries can cause severe performance loss. Operating at high temperature, as in the HT-NaS batteries, can overcome these performance issues, but the concern of HT-NaS batteries is thermal runaway especially under high current density operation. Therefore, an efficient thermal management system will be crucial for safe and efficient operation of NaS batteries at high temperature and high current density.

Existing literature on thermal management strategies for NaS battery models is rather scarce compared to other battery systems. Though NaS batteries have undergone continuous development, safety and thermal runaway have been a serious concern [62], especially at the grid level. Thermo-electrochemical models are useful for evaluating thermal properties of the cell at high current-density operations. Eck [63] suggested that the final design of the thermal management system should be able to heat/cool the battery to maintain it at the preferred temperature and ensure an even temperature distribution throughout the battery. Hartenstine [64] used a variable conductance heat pipe (VCHP) to maintain the temperature of a NaS cell. However, the approach is not adequate to rapidly remove large amounts of variable heat as would be expected for grid-connected batteries. Thermal management strategies for other types of batteries such as

the Li-ion batteries [65][66][67][68][69][70][71][72][73] can be highly useful resources for NaS batteries as well.

One of the critical considerations for designing an efficient thermal management system for a NaS battery module is that the temperature at any location in each cell remains between 300 $^{\circ}$C to 400 $^{\circ}$C. For maximizing the efficiency, the cells should be operated as close as 400 $^{\circ}$C without exceeding it. During discharge, electrochemical reactions in the NaS cells are exothermic while they are endothermic during charge. The Ohmic heat loss is always positive irrespective of whether the cell is charging or discharging. Therefore, higher amounts of heat are generated during discharge than charge. This aspect motivates a thermal management design that can efficiently reject or vary the amount of heat with time. During fast charging/discharging in a grid-connected system, there would be high variability in heat generation further motivating rapid and efficient variable heat rejection. Furthermore, since the NaS batteries can operate around 300-400 $^{\circ}$C, the heat can be used for other applications such as preheating combustion air, residential heating, etc. thus improving the overall system efficiency. From this perspective, it is desirable to minimize the variability in the heat rejection (i.e. temporal variation in the heat rejection from the battery). Overall considerations of the aspects discussed above motivates a thermal management design that can maintain the temperature at any location in any cell close to 400 $^{\circ}$C but does not exceed that temperature. Moreover, it should be capable of rapidly rejecting variable amounts of heat from the cells, while minimizing the variability in the heat rejection rate from the battery to the environment. Obviously, consideration of these competing aspects makes design and operation of the thermal system for NaS battery modules very challenging.

Thermal management strategies for batteries can be largely divided into three categories- active cooling, passive cooling, and hybrid cooling. Active cooling using forced air convection is by far the most common strategy [69][74][75][76][77]. The forced air convection strategy is often used due to the maturity of that technology, ready availability of the utility, and compatibility with the cell materials. However, active cooling creates uneven temperature within the battery module affecting the battery performance and battery life. Optimization of the air flow path [78] can help to reduce the non-uniformity in temperature distribution, albeit at the cost of complicated flow path designs. However, due to the low specific heat of air and a low heat transfer coefficient, rapid removal of large amount of variable heat can be challenging using forced air convection. If the air

flow and heat removal rates vary significantly, it may not be acceptable for many systems where the rejected heat is being utilized, as noted earlier. Passive cooling strategies use a phase change material (PCM) for cooling [79][80]. Since the system can reject the heat to the PCM that changes phase over a small temperature range [80][81][82][83][84][85], the PCM can minimize the temperature variation of the battery module along with little to no variation in the heat rejection rate compared to active cooling.

The PCM material and its quantity are selected by considering a number of criteria such as the melting temperature, latent heat, sensible heat capacities, thermal stability, mechanical stability, cyclic property degradation, heat transfer characteristics, and cost. Though passive cooling can maintain the desired temperature within a battery module, the PCM can only absorb heat inactively. Under fast, variable, and/or continuous charging/discharging conditions, the passive thermal management system may not adequately reject heat from the PCM leading to a buildup of heat that can lead to subcooling (i.e., completely solidified and then exchanging sensible heat) or superheating (i.e., completely melting and then exchanging sensible heat). Therefore, a combination of active cooling and passive cooling is used in hybrid thermal management [86][87][88]. In this paper, all three thermal management strategies, i.e. active cooling, passive, and hybrid cooling are simulated and compared for the sodium-sulfur battery module.

To develop an efficient thermal management system, a detailed dynamic model of the entire battery system that can capture nonlinearities in the temperature under changing and discharging conditions is a valuable tool. However, detailed, dynamic, non-isothermal models of NaS batteries are scarce in the open literature. Hussein and Cheung [46] developed an equivalent circuit model for a NaS battery where, the heat generation and heat transfer at the level of individual cells were not considered. For small power systems, Sarasua and Molina [47] developed a simple model of a NaS battery to analyze its thermal behavior. Min and Lee developed a steady state lumped thermal model for an entire cell, as well as a battery module [48]. Aygun [49] developed a heat transfer model that can be used as a computational design tool to calculate the two-dimensional distribution of temperature inside a NaS battery. Existing papers on non-isothermal NaS battery models lack consideration of detailed mechanisms of heat generation and transfer at the level of the individual cells. Moreover, these papers also neglect the variation of thermo-physical properties with temperature, which can affect the dynamic characteristics of the cell and as a result that of the

battery. Under high current density operation of the NaS cells, there can be considerable spatial and temporal variation of temperature in individual cells and large differences in temperature characteristics from cell to cell depending on the thermal management strategy. Since this paper is focused on developing thermal management strategies under high current density operation, a dynamic thermal-electrochemical model of the NaS battery is developed based on the model of the sodium sulfur cell developed in our previous work [89] that can capture the spatial and temporal variation of temperature in each of the cells. However, the cell model developed in our previous work is highly nonlinear, strongly coupled, and is computationally very expensive, if not intractable, when used to simulate hundreds of cells present in a battery module. Thus, model reduction is desired. Various strategies like proper orthogonal decomposition, orthogonal collocation on finite elements, quasi linearization approximation etc., have been applied to Li-ion battery models to reduce the order and complexity of the model [13][90][91][92][93]. These strategies differ greatly in terms of their applicability, flexibility, computational expense, and accuracy [13][94]. In this paper, a strategy involving coordinate transformation and direct orthogonal collocation is developed, similar to the work of Northrop et al. [13] for Li-ion battery.

The rest of the chapter is arranged as follows. Section 3.2.1 provides a brief review of the model of the single NaS cell developed in our previous work [89]. Section 3.2.2 provides the details of the reduced order model development for a single cell. Section 3.2.3 describes the model set up and specification of the battery module and the stack. Section 3.3 details the development of the specifications and model of active, passive and hybrid thermal management strategies. Section 3.4 includes results followed by conclusion in Section 3.5.

3.2. Model Development

The graphical representation of a typical central sodium sulfur cell is shown in Figure 3.1. The solid ceramic beta”-alumina electrolyte is sandwiched between the central molten sodium electrode that is contained in a stainless-steel wick and the outer molten sulfur/sodium-polysulfide electrode. For better electronic conduction [44], a graphite matrix is placed in the sulfur electrode. More information regarding the battery cell specifications has been provided in Chapter 2.

3.2.1. Cell Model

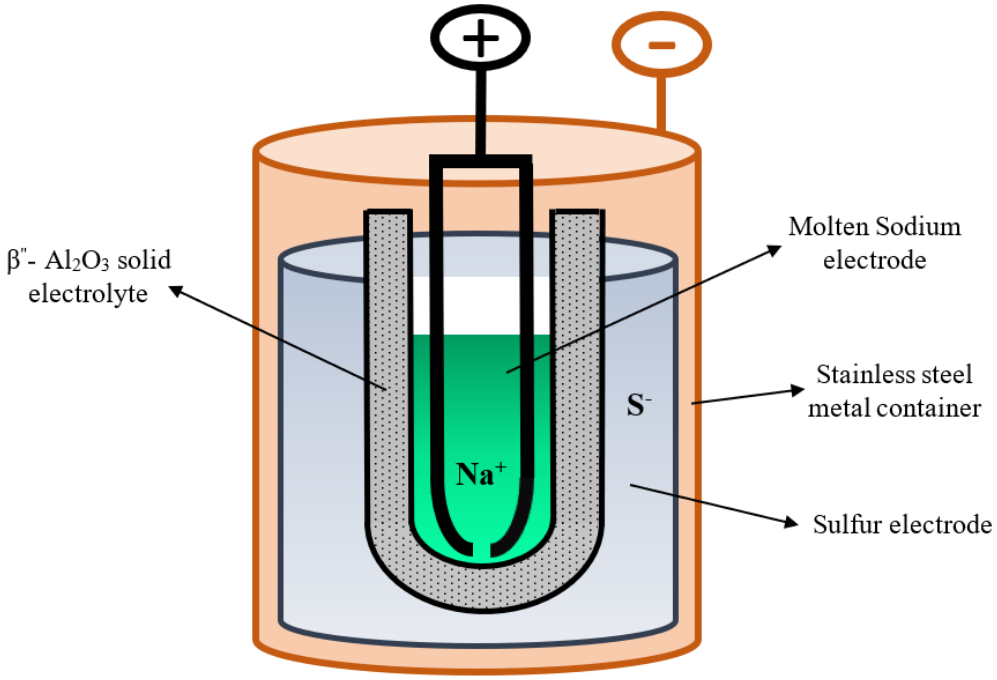

Figure 3.1. Graphic representation of a central sodium sulfur cell

The overall cell reaction is given by:

$$2Na + xS \leftrightarrow Na_2S_x \tag{3.1}$$

For maintaining the cell efficiency in a desired range, the cells are operated at a temperature range of 300-400 ˚C, in which sodium, sulfur, and polysulfides all exist in the liquid phase [31]. At 350 ˚C the electromotive force of the cell reaches 2.075 V [31] and the specific energy density reaches 760 Wh/kg, nearly three times that of a lead acid battery [7].

Details of the cell model can be found in Chapter 2. This section provides a summary of that chapter. In that chapter, a dynamic, fully coupled thermal-electrochemical model was developed. Rate limiting mechanisms take place in the sulfur electrode, making it the most important component of the sodium sulfur cell. However, the electrolyte can also cause considerable losses depending on the operating temperature. The temperature of the sodium electrode is expected to be the highest for this particular cell configuration as the sodium electrode is centrally located. Therefore, a model for the sodium electrode, sulfur electrode and the electrolyte were developed in the previous chapter.

Table 3.1. Dynamic sodium sulfur cell model

Equations	Governing equations	Boundary condition
Sodium electrode		
Energy Balance	$\left(m_{ss}c_{p,ss}\right)\frac{\partial T_{(Na)}}{\partial t}+\left(m_{Na}c_{p,Na}\right)\frac{\partial T_{(Na)}}{\partial t}=$ $q_{(Na)}+\left(2\pi r_{el,i}L\lambda_{(el)}\right)\frac{\partial T_{(el)}}{\partial r}\Big\vert_{r=r_{el,i}}$	
Heat source term	$q_{(Na)}=\frac{I^2\rho_{l(Na)}r_{el,i}}{2\pi(r_{el,i}/2)L}$	
Sodium-ion conservation equation	$\frac{\partial C_{+(Na)}}{\partial t}=\frac{-I}{FV_{(Na)}}$	
Potential drop equation	$\varphi_{i(Na)}=-\eta_{(Na)}$	
Beta"-alumina electrolyte		
Energy balance	$\frac{\partial T_{(el)}}{\partial t}=\frac{1}{\rho_{(el)}c_{p(el)}r}\left(q_{(el)}r+\frac{\partial}{\partial r}\left(r\lambda_{(el)}\frac{\partial T_{(el)}}{\partial r}\right)\right)$	$@\ r=r_{el,i}$ $T_{(el)}=T_{(Na)}$ $@\ r=r_{el,\mathrm{o}}$ $T_{(el)}=T_{(\mathrm{S})}$
Heat source term	$q_{(el)}=\frac{J^2}{\sigma_{i(el)}}$	
Sodium-ion conservation equation	$\frac{\partial C_{+(el)}}{\partial t}=\frac{D_{(el)}}{p_{(el)}}\frac{1}{r}\frac{\partial}{\partial r}\left(r\frac{\partial C_{+(el)}}{\partial r}\right)$	$@\ r=r_{el,i}$ $C_{+(Na)}=C_{+(el)}$ $@\ r=r_{el,o}$ $C_{+(el)}=C_{+(S)}$
Current density equation	$-\sigma_{i(el)}\frac{\partial\varphi_{i(el)}}{\partial r}-FD_{(el)}\frac{\partial C_{+(el)}}{\partial r}=J$	$@\ r=r_{el,i}$ $\varphi_{i(el)}=-\eta_{Na}$

(‘contd.)

Sulfur electrode		
Energy balance	$\rho_{(S)} c_{p(S)} \frac{\partial T_{(S)}}{\partial t} - \frac{1}{r}\frac{\partial}{\partial r}\left(r\lambda_{(S)}\frac{\partial T_{(S)}}{\partial r}\right) = q_{(S)}$	$@\ r = r_{el,o}$ $-\lambda_{(el)} 2\pi r_{el,o} L \frac{\partial T_{(el)}}{\partial r} = -\lambda_{(S)} 2\pi r_{el,o} L \frac{\partial T_{(S)}}{\partial r} \pm Ip_t T_{(S)}$ $@\ r = r_o$ $\frac{\partial T_{(S)}}{\partial r} + (\frac{\alpha}{\lambda_{(S)}})(T_{(S)} - T_{air}) + (\frac{\epsilon\delta}{\lambda_{(S)}})(T_{(S)}^4 - T_{air}^4) = 0$
Heat source term	$q_{(S)} = Q_{Ohmic} + Q_{Entropy}$ $Q_{Ohmic} = \frac{1}{\sigma_{e(S)}}\left(\frac{I}{2\pi r L}\right)^2$ $Q_{Entropy} = \frac{a_s}{K_p}(\varphi_{e(S)} - \varphi_{i(S)} - \mu)\left(T\frac{dE}{dT}\right)$	
Sodium-ion conservation equation	$\frac{\partial C_{+(S)}}{\partial t} = -\frac{1}{F}\frac{a_s}{K_p}(\varphi_{e(S)} - \varphi_{i(S)} - \mu)$	
Charge conservation equation	$-\sigma_{i(S)}\frac{\partial}{\partial r}\left(r\frac{d\varphi_{i(S)}}{dr}\right) + r\frac{a_s}{K_p}\varphi_{i(S)} = \frac{1}{3}FD_{(S)}\left(\frac{3t_+ - 1}{t_+(1-t_+)}\right)\frac{\partial}{\partial r}\left(r\frac{dC_{+(S)}}{dr}\right) + r\frac{a_s}{K_p}(\varphi_{e(S)} - \mu)$ $-\sigma_{e(S)}\frac{\partial}{\partial r}\left(r\frac{d\varphi_{e(S)}}{dr}\right) + r\frac{a_s}{K_p}\varphi_{e(S)} = r\frac{a_s}{K_p}(\varphi_{i(S)} + \mu)$	$@\ r = r_{el,o}$ $\varphi_{i(el)} = \varphi_{i(S)}$ $@\ r = r_o$ $\frac{\partial C_{+(S)}}{\partial r} = 0$ $@\ r = r_o$ $\frac{\partial \varphi_{i(S)}}{\partial r} = 0$ $\varphi_{e(S)} = \varphi_0$

Summary of the governing equations and the boundary conditions are shown in Table 3.1. The model considered heat generation due to Ohmic loss within the cell, Peltier heat at the electrolyte boundaries, and heat due to the entropy change. The first-principles model included conservation of ionic and electronic species and energy as shown in Table 3.1. Temperature dependent correlations for thermophysical properties were also developed in Chapter 2.

Radiative and convective heat loss from the outer wall of the cell to the environment was also modeled. In previous chapter, the environment in which the cell was placed was assumed to be temperature-controlled, where the temperature could be perfectly controlled at a desired temperature in the range of 300-400 ˚C. In this chapter, the environmental temperature for any given cell depends on the thermal interaction with other cells in the battery and the specific thermal management strategy.

The dynamic, spatially distributed cell model developed in our previous work is computationally expensive for simulating batteries and battery modules comprising hundreds of cells. One way of reducing the computational expense of that earlier model is to reduce the large number of partial differential algebraic equations (PDAEs) in that model to differential algebraic equations (DAEs) as described below.

3.2.2. Reduced Order Model

3.2.2.1. Coordinate transformation

As shown in Figure 3.1, the sodium sulfur cell model has three spatial domains defined consecutively. The sodium electrode, electrolyte, and negative sulfur electrode are defined in the spatial domain of $[0, r_{el,i}]$, $[r_{el,i}, r_{el,o}]$, and $[r_{el,o}, r_o]$, respectively. Each spatial domain is normalized to [0, 1] by using the scaling variables given by Equations (3.2) to (3.4).

$$R_1 = \frac{r}{r_{el,i}} \qquad \text{(Sodium electrode)} \tag{3.2}$$

$$R_2 = \frac{r - r_{el,i}}{r_{el,o} - r_{el,i}} \qquad \text{(Electrolyte)} \tag{3.3}$$

$$R_3 = \frac{r - r_{el,o}}{r_o - r_{el,o}} \qquad \text{(Sulphur electrode)} \tag{3.4}$$

The scaling approach is applied to the appropriate equations in Table 3.1. As an example, by applying the scaling approaches given by Equations (3.2) to (3.4) to the energy balance equation of sodium electrode, electrolyte, and negative sulfur electrode given in Table 3.1, the following transformed equations are obtained.

$$m_{ss} c_{p,ss} \frac{\partial T_{(Na)}}{\partial t} + m_{Na} c_{p,Na} \frac{\partial T_{(Na)}}{\partial t} = q_{(Na)} + 2\pi L \lambda_{(el)} \frac{\partial T_{(el)}}{\partial R} \tag{3.5}$$

$$\frac{\partial T_{(el)}}{\partial t} = \frac{1}{(Rr_{el,o} - r_{el,i})\rho_{(el)} c_{p(el)}}$$

$$\left((Rr_{el,o} - r_{el,i}) q_{(el)} + \frac{1}{r_{el,o}} \frac{\partial}{\partial R} \left(\frac{(Rr_{el,o} - r_{el,i})}{r_{el,o}} \lambda_{(el)} \frac{\partial T_{(el)}}{\partial R} \right) \right) \tag{3.6}$$

$$(Rr_o - r_{el,o}) \rho_{(s)} c_{p(s)} \frac{\partial T_{(s)}}{\partial t} - \frac{1}{r_o} \frac{\partial}{\partial R} \left(\frac{(Rr_o - r_{el,o})}{r_o} \lambda_{(s)} \frac{\partial T_{(s)}}{\partial R} \right) = (Rr_o - r_{el,o}) q_{(s)} \tag{3.7}$$

The spatial variables are independent and scaled between 0 to 1. Therefore, they can be replaced by a dummy spatial variable, R.

3.2.2.2. Orthogonal Collocation

The model is then discretized in the spatial domain using orthogonal collocation [13] using the following equation:

$$u(R,t) = A(R,t) + \sum_{k=0}^{N} B_k(t)\, T_k(R) \tag{3.8}$$

where $u(R,t)$ is the variable of interest, $T_k(R)$ represent the chosen trial functions with homogenous boundary conditions, $A(R,t)$ is a function chosen to satisfy the (time-dependent) boundary conditions, and $B_k(t)$ represent the coefficients of the trial functions.

Cosine functions are selected as the trial functions. Linear and/or quadratic terms are added to satisfy the boundary conditions. As an example, the temperature equations are approximated as follows:

$$T_{(Na)}(R,t) = A_{(Na),T}(t)R^2 + \sum_{K=0}^{N_p} B_{(Na),T,k}(t) Cos(k\pi R) \tag{3.9}$$

$$T_{(el)}(R,t) = A_{(el),T,0}(t)R + A_{(el),T,1}(t)R^2 + \sum_{K=0}^{N_s} B_{(el),T,k}(t) Cos(k\pi R) \tag{3.10}$$

$$T_{(s)}(R,t) = A_{(s),T,0}(t)R + A_{(s),T,1}(t)R^2 + \sum_{K=0}^{N_n} B_{(s),T,k}(t) Cos(k\pi R) \tag{3.11}$$

Similarly, the remaining partial differential equations of the cell model are transformed to ordinary differential equations as shown in Table 3.2. The governing differential equations are exactly satisfied at the collocation points, which are zeros of Jacobi polynomials [13]. The Jacobi polynomials (also known as Gauss-Jacobi polynomials) of degree N can be written as follows:

$$P_N{}^{(\alpha,\beta)}(r) = \sum_{k=0}^{N} (-1)^{N-k} \gamma_k r^k \tag{3.12}$$

$$\gamma_k = \frac{N-k+1}{k}\frac{N+k+\alpha+\beta}{k+\beta}\gamma_{k-1} \tag{3.13}$$

where α and β are the characteristic parameters of the Jacobi polynomial. We have considered, $\alpha = \beta = 0$ as in Gauss-Legendre collocation. A system of ordinary differential equations has been successfully obtained by considering $N = 3$ collocation points, which is simulated in ASPEN V.8.4. Orthogonal collocation is applied only for the differential variable in the electrolyte and sulfur electrode since they are functions of space and time.

Table 3.2. Approximate forms of key variables in each region

Governing equation
Sodium electrode
Not required
Beta-Alumina electrolyte
$T_{el}(R,t) = A_{el,T,0}(t)R + A_{el,T,1}(t)R^2 + \sum_{K=0}^{N_{el}} B_{el,T,k}(t)Cos(k\pi R)$
$C_{el}(R,t) = A_{el,C,0}(t)R + A_{el,C,1}(t)R^2 + \sum_{K=0}^{N_{el}} B_{el,C,k}(t)Cos(k\pi R)$
$\varphi_{i(el)}(R,t) = A_{el,\varphi_i,0}(t)R + A_{el,\varphi_i,1}(t)R^2 + \sum_{K=0}^{N_{el}} B_{el,\varphi_i,k}(t)Cos(k\pi R)$
Sulfur electrode
$T_s(R,t) = A_{s,T}(t)\left(\frac{1}{2}R^2\right) + \sum_{K=0}^{N_s} B_{s,T,k}(t)Cos(k\pi R)$
$C_s(R,t) = A_{s,C}(t)(R-1)^2 + \sum_{K=0}^{N_s} B_{s,C,k}(t)Cos(k\pi R)$
$\varphi_{i(s)}(R,t) = A_{s,\varphi_i}(t)(R-1)^2 + \sum_{K=0}^{N_s} B_{s,\varphi_i,k}(t)Cos(k\pi R)$
$\varphi_{e(s)}(R,t) = A_{s,\varphi_e,0}(t)R + A_{s,\varphi_e,1}(t)R^2 + \sum_{K=0}^{N_s} B_{s,\varphi_e,k}(t)Cos(k\pi R)$

3.2.3. Stack Model

With a set of reduced ordinary differential equations (ODEs), instances of a single cell model were created. The instances are combined in a series pattern to design a nominal 640 V module inspired by NGK [95]. The module specifications are shown in Table 3.3.

Table 3.3. Specifications of sodium-sulfur module

Parameter	***NaS Module***
Configuration	320 cells arranged in series
Voltage	640 V
Power	20 kW
Capacity	25.6 kWh

Two such modules are connected in series to develop a stack such that: (1) the capacity can be expanded as needed and (2) power can be obtained through steady, continuous discharge or else high pulses for shorter larger pulses. Aspen Custom Modeler (ACM) V.8.4. was used to simulate all the cells simultaneously.

3.3. Thermal Management

Figures 3.2(i), 3.2(ii), and 3.2(iii) show the configurations for active cooling, passive cooling and hybrid cooling that are modeled and evaluated. In active cooling, the cooling medium chosen is air as. In passive cooling, a suitable PCM is considered for heat rejection. In hybrid cooling, a combination of air cooling and PCM is considered.

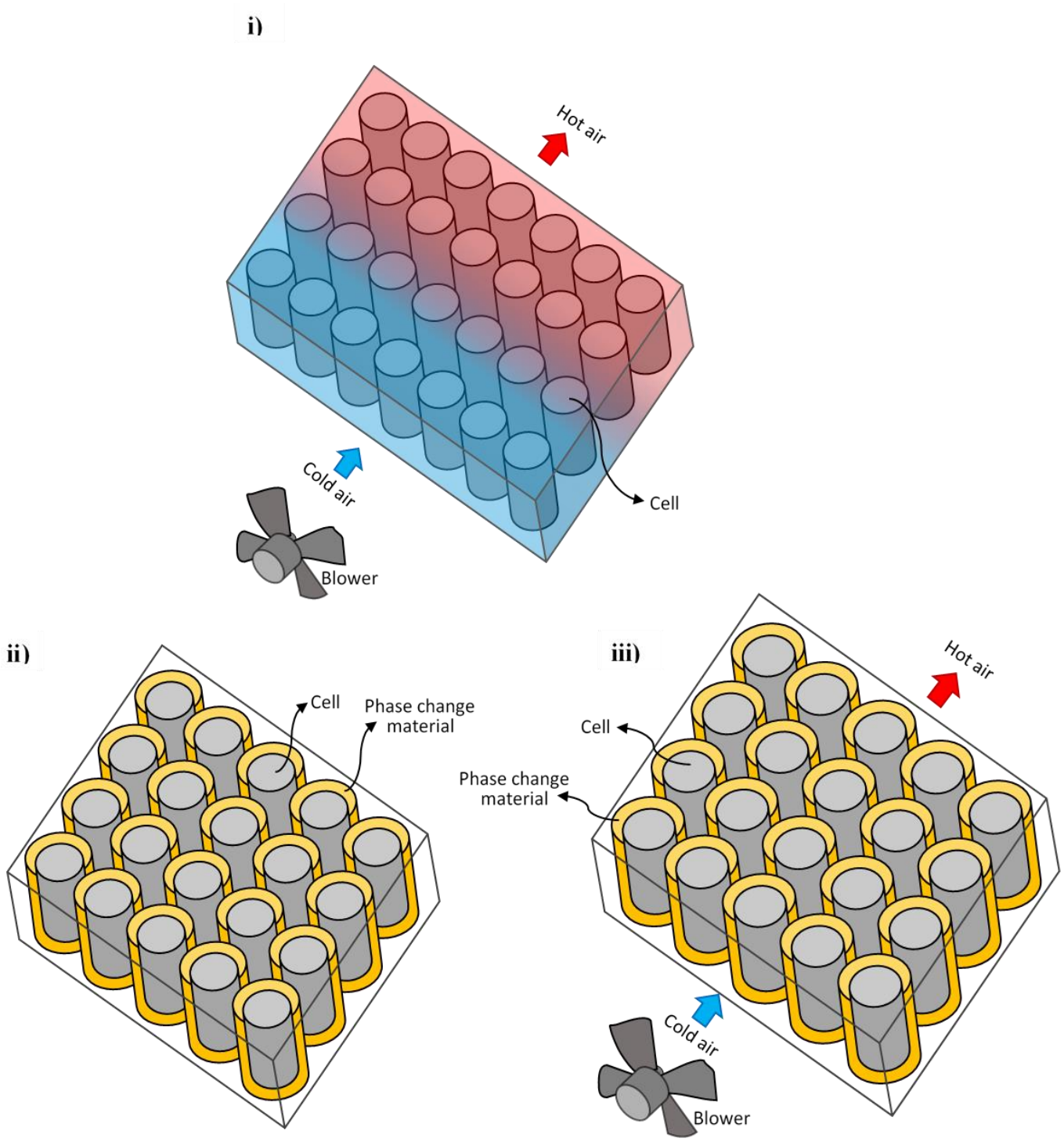

Figure 3.2. Schematic representation of i) active thermal management strategy ii) passive thermal management strategy iii) hybrid thermal management strategy

3.3.1. Active Thermal Management System

A schematic of active thermal management system is shown in Figure 3.2 (i). Depending on the desired flow path, the cooling air from fan or blower enters the system and passes throughout the cells maintaining the temperature.

The energy conservation equation for air is [76][77]:

$$\rho_{air} C_{p(air)} \left(\frac{\partial T_{air}}{\partial t} + v_{air} \frac{\partial T_{air}}{\partial z} \right) = \sum q_{cell} \tag{3.14}$$

where ρ, λ and C_p are density, thermal conductivity and specific heat at a given temperature and q_{cell} is the total heat generated by a single cell.

Heat is lost to the surroundings (air flow) at the outer metal container of the cell.

At the cell-air interface both convection and radiation are considered.

$$q_{cell} = a_{spe} h_{air} (T_{cell} - T_{air}) + \epsilon \delta a_{spe} (T_{cell}^4 - T_{air}^4) \tag{3.15}$$

where h_{air} is the heat transfer coefficient of air and a_{spe} is the specific area. The correlation for calculating the heat transfer coefficient is provided in Table B.1 in Appendix B.

3.3.2. Passive Thermal Management System

In a passive thermal management strategy, each cell is surrounded by a PCM as shown in Figure 3.2 (ii). The PCM begins to melt as it absorbs the heat generated by the cells.
The enthalpy change for the changing phase of the PCM is used in the mathematical formulation of passive cooling [79][82]. The energy conservation equation for PCM is as follows:

$$\rho_{PCM} \frac{\partial H_{PCM}}{\partial t} = \lambda_{PCM} \left(\frac{\partial^2 T_{PCM}}{\partial r^2} + \frac{1}{r} \frac{\partial T_{PCM}}{\partial r} \right) \tag{3.16}$$

$$H_{PCM} = h'_{PCM} + \Delta H_{PCM} \tag{3.17}$$

$$h'_{PCM} = \int_{T_0}^{T} C_{p,PCM} dT \tag{3.18}$$

$$\Delta H_{PCM} = \beta \gamma \tag{3.19}$$

$$m_{PCM} * \frac{d\beta}{dt} * \gamma = q_{cell} \quad \text{for} \quad 0 \leq \beta \leq 1 \tag{3.20}$$

where $\rho, \lambda, H, h', \Delta H, \beta$ and γ are the density, thermal conductivity, enthalpy, sensible heat, enthalpy of melted PCM, liquid fraction of melted PCM, and specific phase change enthalpy respectively.

The boundary condition at the cell-PCM interface is:

$$-\lambda_{cell}\frac{\partial T_{cell}}{\partial r} = -\lambda_{PCM}\frac{\partial T_{PCM}}{\partial r} \tag{3.21}$$

The convective heat transfer at the PCM-air interface is given by:

$$-\lambda_{PCM}\frac{\partial T_{PCM}}{\partial r} = h_{PCM}(T_{PCM} - T_{air}) \tag{3.22}$$

where h_{PCM} is the heat transfer coefficient of PCM. An equation for the heat transfer coefficient of PCM is given in Table B.1 in Appendix B. The following properties are considered for selection of the PCM: (i) melting temperature in the desired temperature range, (ii) high heat of fusion, (iii) high thermal conductivity, (iv) high specific heat and density, (v) long term stability during repeated cycling. After evaluating a number of candidate PCMs, potassium nitrate was selected as the PCM. Various properties of PCM are listed in the Appendix B.

3.3.3. Hybrid Thermal Management System

A hybrid thermal management strategy is a combination of forced air convection and passive cooling [86][87][88]. The battery module containing cells, surrounded by PCM, and placed in the path of the air is shown in Figure 3.2 (iii). A PID controller is developed to maintain the liquid fraction of PCM. Experimentally, the liquid fraction of PCM can be measured using a proximity-meter (volumetric expansion of about 13% is expected when fully melted). Using a PID controller that manipulates the air flowrate, the PCM liquid fraction is maintained between 0 to 1.

3.4. Results and Discussions

The model of a single cell after coordinate transformation and orthogonal transformation is coded in ACM [89]. To develop a battery module in ACM consisting of 320 cells, instances of the single cell model are used. Thermal management strategies and the control systems are also modeled in ACM.

3.4.1. Performance of the reduced order model

Three collocation points are found to be sufficient for all regions. The difference in the key performance variables of interest such as the V-I characteristics and temperature distribution are found to be very low. The largest error was observed in the calculation of the sodium ion concentration in the sulfur electrode under some transient conditions. Figure 3.3 compares the full order model and the reduced order model for 6A discharge current at 60% SOD for an ambient temperature of 330 $^{\circ}$C. The mean absolute error for potential profile is nearly 0.7% and for temperature profile, it is about 0.3% for this specific case. For many other cases that we compared the reduced order model with the full order model, the error is found to be less than 1%. Therefore, the reduced order model was used for battery simulation presented in subsequent sections.

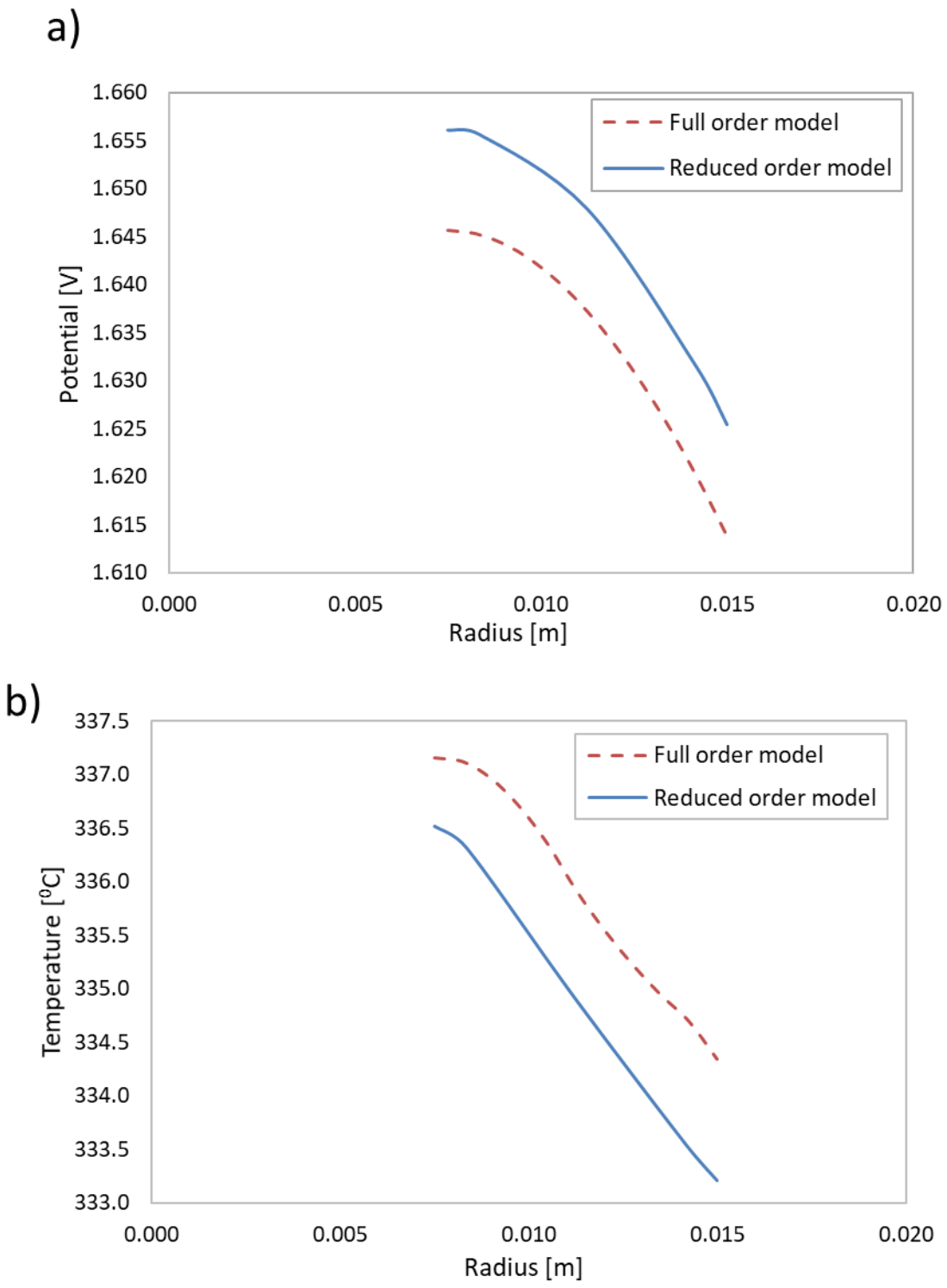

Figure 3.3. For PDE model and 3 collocation points ODE-based model for +6A discharge for an ambient condition of 330 ˚C at 60% SOD comparison of a) potential profile b) temperature profile with respect to the radius of the cell

3.4.2. Temperature distribution during charge/discharge

Figure 3.4 shows the difference in the temperature profile in a single cell between charge and discharge under the same current of 22 A at 60% SOD. While the ambient temperature is kept constant at 330 ˚C for both charge and discharge, the temperature difference between the environment and the cell center during charge is 12 ˚C and during discharge is 24 ˚C. In this case the ambient temperature is kept constant, but when hundreds of cells reject heat to the environment, the environmental temperature, to which the batteries are exposed, can go up if the heat is not rejected efficiently, which, in turn, will lead to further rise in the cell temperature during discharge.

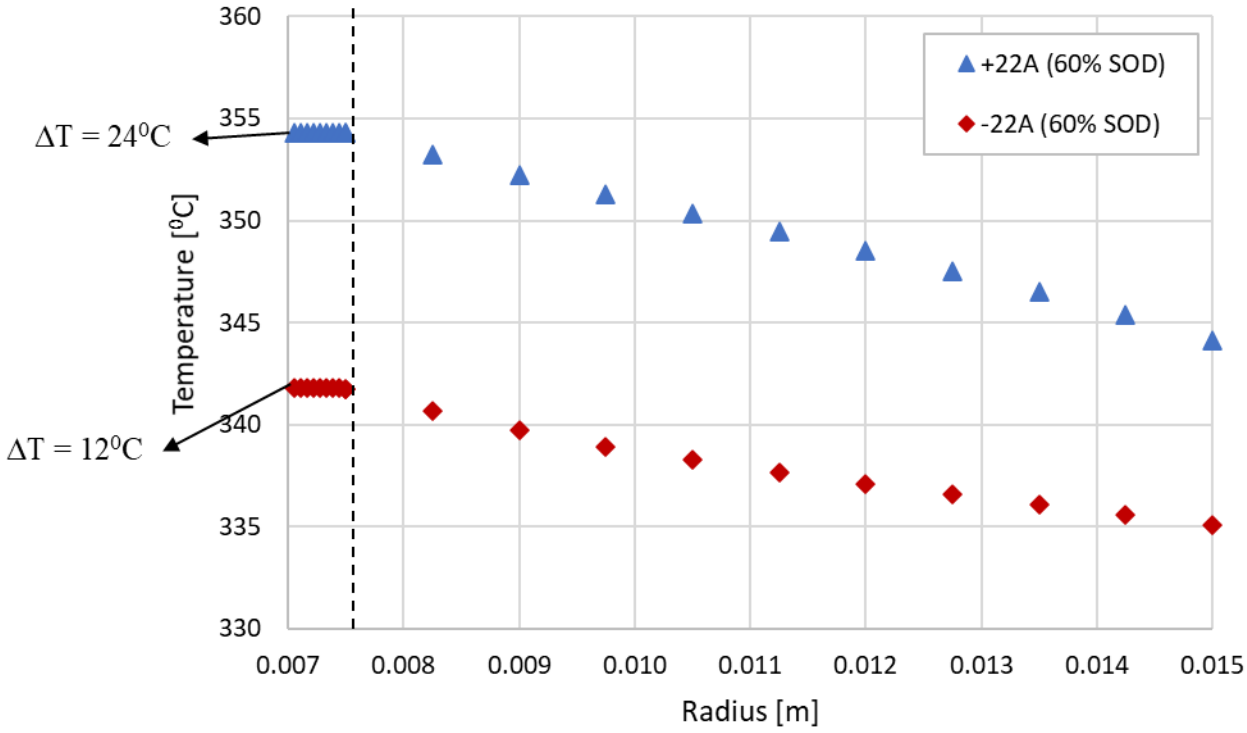

Figure 3.4. Temperature profile in the cell during discharging and charge at 60% SOD for ±22 A current (corresponding to 260 mA/cm^2 current density) for the ambient temperature of 330 ˚C (vertical dotted line represents the electrolyte/sulfur electrode interface).

3.4.3. Impact of change in current density

Figure 3.5 shows the transient response of temperature at the center (denoted as $r = 0$) and surface (denoted as $r = r_o$) of a single cell for different current densities. The ambient temperature is kept constant at 335 ˚C. As expected, the maximum cell temperature is at the center irrespective of the

current density. It is observed that the maximum cell temperature is 360.5 ˚C when the current density is 260 mA/cm^2, whereas for 70 mA/cm^2 the maximum cell temperature is 340.5 ˚C. It can also be observed that the maximum cell temperature at the cell outer wall for 260 mA/cm^2 operation is 350 ˚C whereas for 70 mA/cm^2, the corresponding temperature is 338 ˚C. For operation at 260 mA/cm^2 the maximum temperature difference between the center and cell wall is about 10˚C while the corresponding temperature difference is about 3 ˚C for the operation at 70 mA/cm^2. When hundreds of cells reject heat to the environment under high current density operation, the environmental temperature can go up if the heat is not rejected efficiently, which, in turn, will lead to further rise in the cell temperature during discharge. The studies presented in work further motivates development of an effective thermal management strategy.

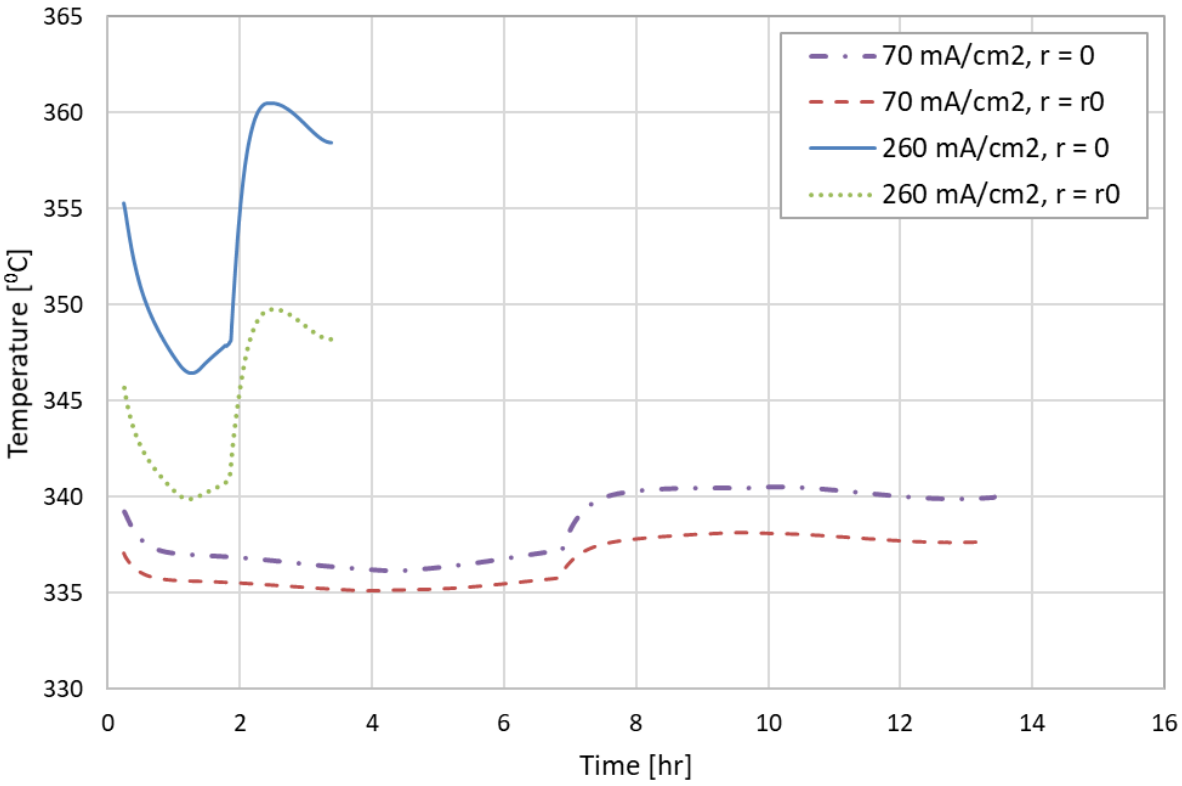

Figure 3.5. Transient response of cell temperature at the center and cell outer wall during discharging and charging at ±6 A current (corresponding to 70 mA/cm^2 current density) and ±22 A current (corresponding to 260 mA/cm^2 current density) for an ambient temperature of 335 ˚C ($r = 0$ is the center of the cell, $r = r_0$ is the surface of the cell).

3.4.4. Thermal Management

3.4.4.1. Active Cooling

In forced air convection, as air passes through the module, the air temperature keeps increasing as it goes towards the exit. Therefore, the exit row cells are always at the highest temperature. The design decision for arranging the total number of cells is the number of rows. For any given flowrate, as the number of rows is increased the flow path length for air increases increasing the outlet side temperature. On the other hand, if the number of rows is lower, then both the flow path length and the air velocity decrease accompanied by a decrease in the heat transfer coefficient. For a given cell arrangement, the air velocity can be increased by increasing the air flowrate. An increase in the air velocity for sustained cycling at a given current density can reduce the relative temperature difference between the inlet and exit cells at any time instant. This reduces the variability in the heat rejection rate as shown in Figure B.2 in the Appendix B, but this will lead to more parasitic losses as shown in Figure B.3. In addition, as the air velocity is increased for sustained cycling at a given current density, the average cell temperature will be lower causing a reduction in the cell efficiency.

In this work, the maximum current for any cell is considered to be +/-22 A (260 mA/cm^2 current density). For this current density, it was observed that 20 cells in a single row led to the lowest temperature rise in the exit rows of cells. Figure 3.6 shows the transient outer surface temperature of cells located at the (air) inlet row, center row, and exit row for charge/discharge cycles at +/-22 A at an air inlet temperature of 335 $^{\circ}$C for a constant air velocity of 3 m/s. The difference in the minimum and maximum outer wall temperature of the cells located at the exit row is ~2.6 $^{\circ}$C. The maximum temperature difference between the cells located at the air inlet and exit is almost 1 $^{\circ}$C. However, the variability in heat rejection rate is as high as 40% under this condition.

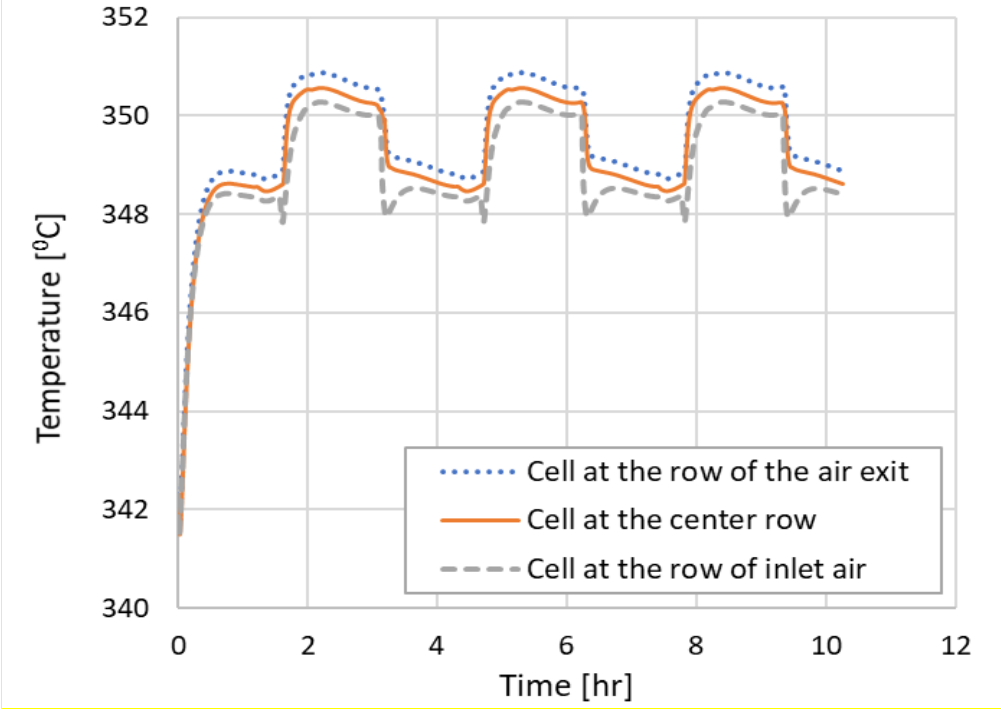

Figure 3.6. Transient profile of cell outer wall temperature for different cells at different locations in a module, in presence of forced air cooling for ±22 A current for an air inlet temperature of 335 ˚C and air velocity of 3 m/s.

3.4.4.2. Passive Cooling

Figure 3.7 shows the transient profile of cell temperatures and liquid fractions for charging and discharging cycles at ±22 A when the cell is placed in the PCM and the ambient temperature at the PCM boundary is constant at 335 ˚C. In this case, all cells, irrespective of their location, have the same temperature profile. In this case, the variability in the heat rejection rate is zero. It is observed that a steady cyclic profile with a relative cell outer wall temperature variation of 2.8 ˚C is achieved. However, the liquid fraction has a sustained increase eventually becoming completely melted beyond which the advantage of the PCM to provide a near-constant boundary temperature for the cells will not be realized. The continuous rise in the liquid fraction is due to the mismatch between the heat rejected and heat generated during charging and discharging cycles. In this case, more heat is generated during discharge than can be rejected during discharge. While the system could reject more heat during charging compared to what is generated, it still cannot reject the additional heat that accumulates in the system during discharge. The heat transfer between the PCM and the environment takes place due to natural convection, thus leading to low heat transfer coefficient.

When the surface area of the PCM is increased (i.e. by providing a higher amount of PCM), the amount of heat exchange to the environment increases. This helps in rejecting sufficient heat during discharge under certain condition. However, in that case the PCM becomes fully solid and its temperature keeps decreasing which further decreases the cell temperature causing efficiency loss. Thus, the main issue with the passive cooling approach is the lack of ability for variable heat rejection.

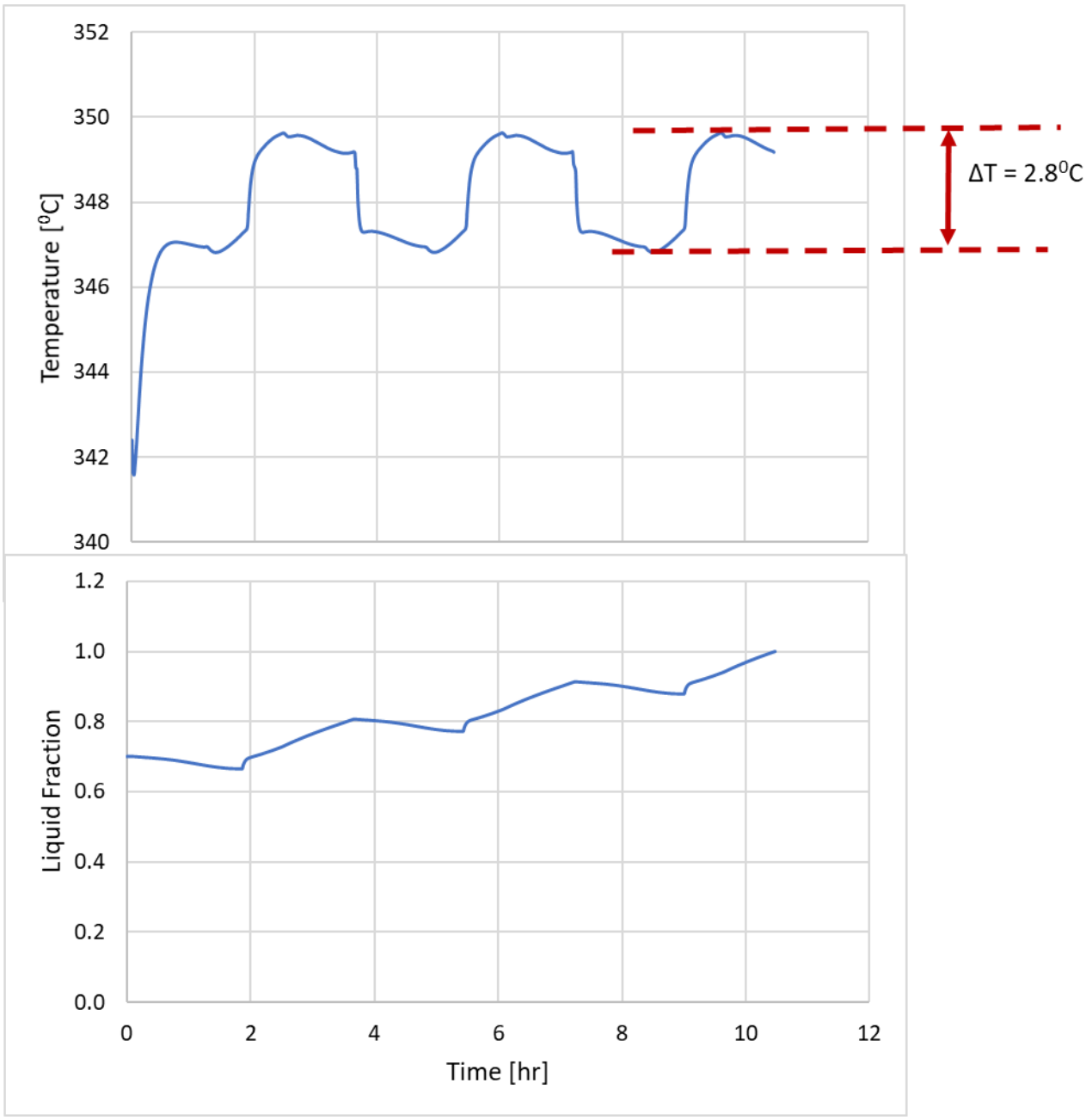

Figure 3.7. Transient profile of liquid fraction of PCM and temperature of cell at ±22 A current in presence of phase change material for an ambient condition of 335 ˚C

3.4.4.3. Hybrid Cooling

Combining forced air convection and passive cooling using the PCM provides the flexibility of variable heat rejection. For this arrangement, the liquid fraction can be maintained between 0 to 1 by manipulating the air flowrate. Figure 3.8 shows the temperature profile and liquid fraction

profile during continuous charging and discharging cycles at ±22 A for an air inlet temperature of 335 ˚C. It is observed that not only the temperature variation could be controlled within small variability, but the liquid fraction profiles are controlled as a steady cyclic profile within the desired bounds.

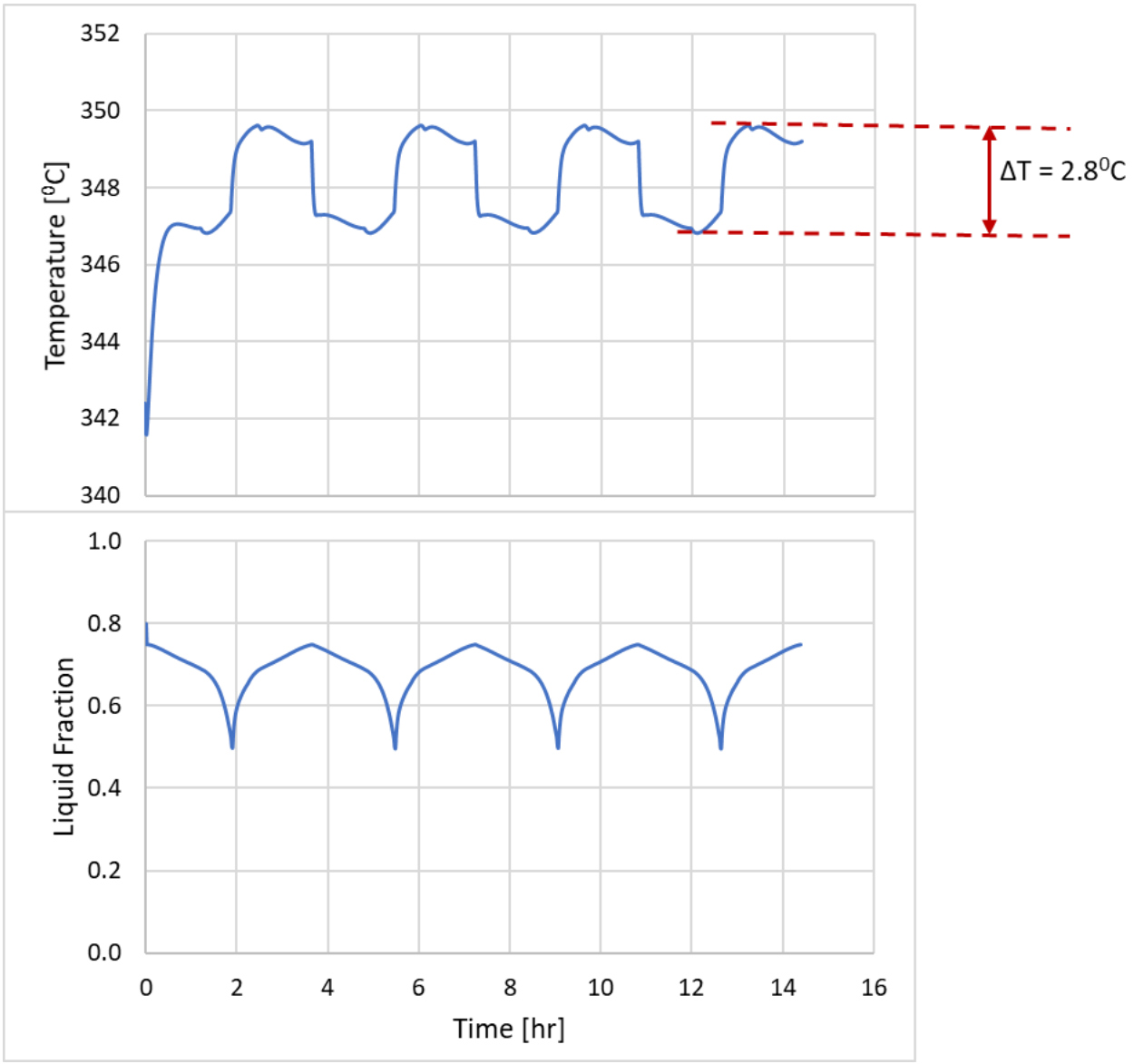

Figure 3.8. Transient profile of liquid fraction of PCM and temperature of cell at ±22 A current in presence of phase change material and forced air convection for an ambient condition of 335 ˚C

In Figure 3.9, the liquid fraction of PCM varies between 0.49-0.75. In this case, if +/-22A is the highest current for this system and the maximum air velocity is the same, then the mass of PCM can be lowered further while still maintaining the liquid fraction within the range of 0-1. In the design, if the maximum continuous charging/discharging rate of a battery module is specified, then the amount of PCM can be calculated. This involves a tradeoff between the capital cost of PCM and the variability in heat rejection. For the given maximum continuous cycling rate of the battery module, the variability in heat rejection can be eliminated by rejecting the same amount of heat at all instances of time and making that rate equal to the time-averaged heat generation rate for an entire charge-discharge cycle. The minimum amount of PCM that will satisfy this condition is such that during discharge, the PCM liquid fraction will go from zero to one and during charging, it will return from one to zero. Considering the cyclic steady state, any additional amount of PCM does not provide any additional advantage since the effect of the additional mass would lead to a liquid fraction that does not reach the lower/upper limits during charge/discharge cycles. If the amount of PCM is lower than the minimum amount of PCM, then the variability in the heat rejection rate will increase as the amount of PCM decreases. This profile is shown in Figure 8 where the mass of PCM per unit energy is shown as a function of the variability in the heat rejection rate. It can be seen that the variability in the heat rejection rate reaches zero for a current density of +/22 A when the mass of PCM per unit energy becomes 0.74 gm/Wh (i.e. mass of PCM for single cell is 42.43 gm) when the maximum air velocity remains constant at 3 m/s. As expected, as the mass of PCM becomes zero, the variability in the heat rejection rate becomes the same as the active cooling case. For a given mass of PCM, as the maximum air velocity is increased, the variability in heat rejection reduces albeit at the cost of higher parasitic losses. Since, the quantity of PCM affects the capital cost, the tradeoff between the capital cost for PCM, fan power requirement, and variability in the heat rejection rate need to be considered for determining the amount of PCM for the desired maximum continuous charging/discharging rate.

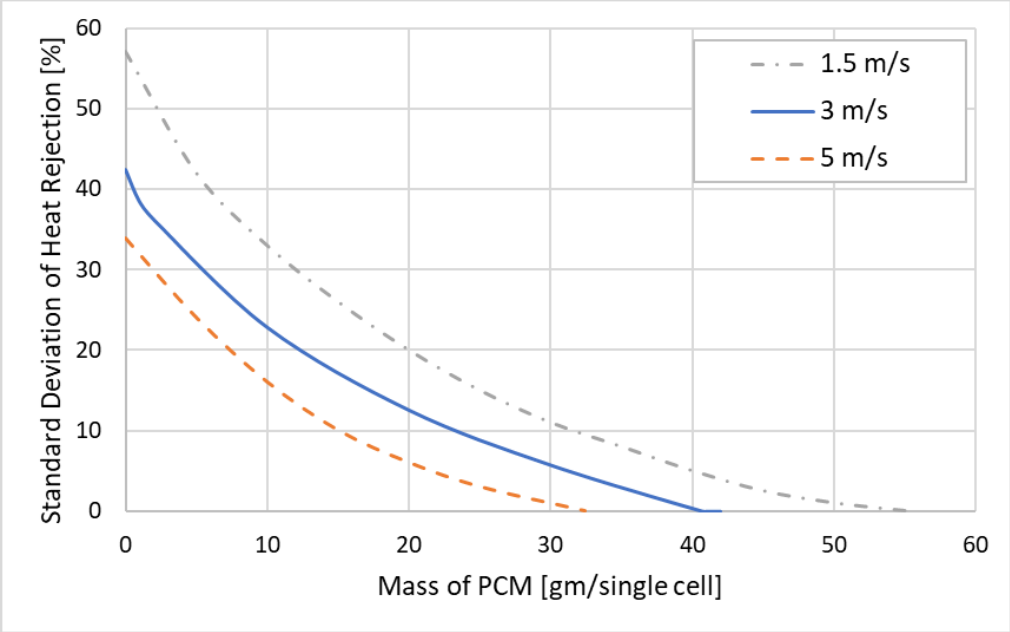

Figure 3.9. Standard deviation in heat rejection for continuous charging and discharging for different mass of phase change material for ±22 A current for different maximum air velocities.

3.5. Conclusions

A dynamic non-isothermal, distributed model of a sodium sulfur battery is developed. This model uses instances of a reduced order model of a single cell that is developed by applying orthogonal collocation to a rigorous PDAE model. Temperature gradients in the cell during discharge are found to be considerably higher than for the charge cycle. For example, the temperature difference between the environment and the cell center is found to be almost 2 times greater during discharge than charge for a single cell at 60% SOD under 260 mA/cm^2 current density for a constant ambient temperature. As the current density increases, there can be a significant temperature rise in a single cell even under the same environmental condition. For example, it was observed that the maximum cell temperature (i.e. at the center of the cell) at 260 mA/cm^2 operation is almost 20 $^{\circ}$C higher than operation at 70 mA/cm^2. The maximum cell temperature at the cell outer wall for 260 mA/cm^2 operation is almost 12 $^{\circ}$C higher than the operation at 70 mA/cm^2. The difference between the maximum and minimum cell temperature at the center and surface at 260 mA/cm^2 is almost 3 times higher compared to that at 70 mA/cm^2 operation.

Three thermal management strategies, namely active cooling, passive cooling and hybrid cooling, are developed and analyzed for a battery stack. For active cooling, as the air velocity is lowered, it results in a higher temperature in the cells in the direction of air flow. As the air velocity is increased, it reduces temperature gradient along the direction of air flow as expected but results in higher parasitic losses and can lead to lower temperatures, especially during charge, leading to a decrease in the efficiency. However, it was observed that the operations at high air flow rates lead to considerable increases in the fan power requirement. For passive cooling using a PCM, the main issue is found to be the lack of ability for variable heat rejection rate leading to rising liquid fraction from cycle to cycle. The capability for variable heat rejection rate is desired due to the significantly different heat generation rate during discharge than charge. The hybrid cooling strategy uses the advantages of both active and passive cooling to maintain the cell temperature. The variability in the cell temperature during charge/discharge cycles is reduced and the liquid fraction is maintained between 0-1. Furthermore, for the design of a sustained, high current density operation, the minimum quantity of PCM may be calculated such that the variability in the heat rejection rate is zero while still maintaining the liquid fraction between 0-1. Obviously for operations at any other current density lower than the maximum, the variability in the heat rejection rate would be zero using a properly designed controller. Adding more mass of PCM than the minimum needed for the design sustained high current density operation simply adds to the capital cost. On the other hand, if the PCM quantity decreases, the variability in the heat rejection rate will increase. The hybrid cooling approach is found to be an efficient strategy that can reduce the variability in the heat rejection rate and cell temperature. Moreover, the quantity of the PCM can be calculated for a battery stack by considering the tradeoff between the variability in the heat rejection rate, capital cost of the PCM, and operating cost due to the fan power requirement.

Chapter 4. Transient Modeling of a Vanadium Redox Flow Battery

4.1. Literature Review

As mentioned in Chapter 1, secondary batteries are of importance for grid-level storage as they can be repeatedly charged and discharged. Rechargeable lead acid and Li-ion batteries are conventional BESS used to store renewable energy [22], [23], [96]–[102]. However, these battery storage systems have certain limitations like low energy efficiency, poor discharge behaviors, high costs and coulombic overheating, especially for large-scale commercialization [103], [104]. Therefore, the inability to store renewable energy safely and affordably at grid-level motivates to continue research on alternative battery technologies [25], [105]. Because of the high energy efficiency, safety, low cost and long cycle life, energy storage using redox flow battery (RFB) has gained increased interest [134]–[149]. Moreover, RFBs have high flexibility since energy capacity and power generation are independent for these batteries [115].

Vanadium redox flow battery (VRFB) is one of the most promising type of RFBs that are commercially available. Compared to other RFBs such as Zn-Br, Fe-Cr and Zn-air batteries, VRFBs have advantages like (a) large (theoretically unlimited) energy capacity - by increasing the quantity of electrolyte, VRFB can supply almost unlimited amount of energy; (b) they can be left completely discharged for long periods without much detrimental effect; (c) no permanent damage is caused by accidental mixing of electrolytes; (d) the electrolyte is aqueous and essentially safe and non-flammable [110], [112]. Moreover, in VRFB, the ability of vanadium to exist in different oxidation states is exploited and same element is used in both cathode and anode, which avoids cross-contamination of elements making it environmentally friendly [136]–[141], [147]–[153]. VRFBs have an overall efficiency of 70%- 90% with a lifetime of more than 15,000 – 20,000 charge/discharge cycles [112].

With vanadium existing as V(II)/V(III) in anode and V(IV)/V(V) in cathode respectively, in sulfuric acid solution, redox reactions take place to generate/store energy. Models were generated using anion exchange membrane [126]. However, the Nafion-115 ion-selective membrane is highly used because of its high chemical stability [112], [127]. Though using single active element in different oxidation states avoids cross-contamination, the ion crossover through the membrane is unavoidable [14], [114], [128]–[132]. Due to the presence of fixed charge in the membrane, the

counter-ions are attracted, and the co-ions are repelled, which results in a discontinuity of the ionic potential and concentration at the membrane electrode interface. This impact is called Gibbs-Donnan effect and for an electrolyte concentration below ~0.2 M [14], [133] this effect can be neglected. However, the electrolyte concentration is generally higher than this value, resulting in the permeation of all ions through the membrane. This results in self discharge and imbalance of the vanadium ions between the negative and positive electrolytes during charging and discharging cycles, which leads to reduction in its Columbic efficiency and lifetime [14], [129]–[132]. Along with the ion-crossover reactions there are other notable side reactions like evolution of H_2 gas at the negative electrode on charge and the evolution of O_2 gas at the positive electrode. The bubbles formed due to the gaseous side reactions results in partial obstruction of electrolyte and reduction in the active surface area available for the reaction [111], [134]–[137]. The evolution of hydrogen gas reduces the mass and charge transport coefficients, and the evolution of oxygen reduces the effective diffusion coefficients and the effective ionic and thermal conductivities [111], [134], [135]. This further results in performance degradation and reduction in lifetime. Moreover, along with the ion-crossover and gaseous side reactions, water transport through the membrane results in capacity degradation. Water transport can be caused because of several processes like water transported along with vanadium ions, electro-osmotic drag, and diffusion between two electrolyte half cells [111], [131]. For estimating and determining the capacity fade or performance degradation with time, a detailed dynamic model of the vanadium redox flow battery that can capture the transients of the voltage, capacity, and state of charge (SOC) is crucial.

Due to prolonged time requirements and high cost of experimental studies, very few ex-situ [129], [138]–[140] and in-situ [141]–[143] experimental studies are available considering the capacity degradation mechanisms. Many researchers developed equivalent circuit models (ECM) to analyze the electrochemical characteristics and to estimate the capacity fade [121], [144]–[152]. First-order [150]–[152] and second order [147], [149] resistor–capacitor (RC) models have also been developed by taking into account the polarization effects of VRFB. Kalman filters have been used for estimating parameters in the ECMs by using measured data [148]. For estimating the capacity fade, sliding mode observer (SMO) has been proposed [121]. However, the effect of ion-crossover, side reactions and water transport were not considered in these papers. Moreover, the dynamic variability of VRFB system due to capacity fade and time-varying parameters have been neglected in the works mentioned above.

For detailed investigation of various degradation mechanisms in the VRFBs, many researchers developed rigorous dynamic models of all-vanadium cell system [11], [14], [130], [131], [134], [135], [137], [180]–[187]. Early works were conducted by Li et al. [153], who proposed a dynamic model to study the transient performance of VRFB under charge and discharge cycling. Syllas-Kazacos et al. [11], [130] developed a dynamic model to study the effects of ion-diffusion and side reactions over long-term performance of VRFB. They investigated the effect of temperature during self-discharge reactions [154] and on capacity fade [137] and, the effect of ambient temperature and flow rate on thermal behavior of VRFB [155]. However, these zero-order models, because of several assumptions, like, uniform ion concentration, and instant ion transfer between the electrode, lack the fidelity to predict all physical and chemical phenomena taking place inside the cell. Shah et al. [156] proposed a two-dimensional (2D) transient model based on momentum and mass transfer and ion conservation to study the impacts of concentration variations, flow rate and porosity on the VRFB. Shah et al. [157] further extended the model to study the effects of non-isothermal dynamic model to estimate the influence of flow rate and current on temperature distribution within the cell. Further, they modeled the effect of evolution of hydrogen and oxygen gases, in the electrolytes, on capacity degradation [134], [135]. Vynnycky [158] developed an asymptotically reduced model to analyze the current density at grid-scale operation for VRFB stacks. Knehr et al. [131] proposed a transient isothermal model incorporating ion-crossover and water transport through the membrane to study the related capacity fade. However, in their work, the Donnan potential, which refers to the unequal distribution of ionic species between two ionic solutions separated by a semipermeable membrane, at the membrane electrode interface was not in agreement with the theoretical value for cation-exchange membrane. Yang et al. [159] studied the effect of ion-crossover in a Nafion ion-exchange membrane by considering the effect of electric field. They obtained results which is not in agreement with those from Knehr et al. [131]. Darling et al. [160] developed a model to analyze the ion-crossover at different current densities. Their work suggested the importance of the effect of electric field and showed that there is an increasing accumulation of ions in positive side with increasing current density. Boettcher et al. [161] developed 0-D and 2-D models considering the effect of ion crossover to predict the capacity fade. He found that the 0-D model has several limitations compared to the 2-D model, which could not capture the entire effect of crossover on capacity fade. Hao et al. [14] modeled an interfacial sub-model at the membrane electrode interface to study the effect of ion-crossover through the

membrane. Their work predicts a faster accumulation of ions in the positive half-cell for cation-exchange membrane than the accumulation in the negative half-cell for anion-exchange membrane. All these modelling studies provide important information for VRFB cell performance. However, due to the complexity associated with the cell chemistry, the understanding of certain mechanisms is still limited. Moreover, most of the papers cited above neglected the combined effect of all capacity degradation mechanisms listed above. In the existing literature, typically different capacity fade mechanisms were evaluated individually and combined to understand their effect on the cell performance. However, the capacity fading mechanisms work synergistically thus need to be evaluated together.

Overall, there is lack of studies in the open literature on detailed dynamic model of VRFB considering two or more capacity fading mechanisms. Such models can be very helpful in diagnostic and prognostic studies of the cell.

4.2. Model Development

The VRFB considered in this study consists of an ion-exchange membrane, separating the positive electrode and negative electrode as shown in Figure 5.1. The system contains two tanks and two pumps connected to the negative electrode and positive electrode respectively, for the electrolyte flow. This separation of the energy conversion part and the storage part helps in having decoupled energy and power capacity.

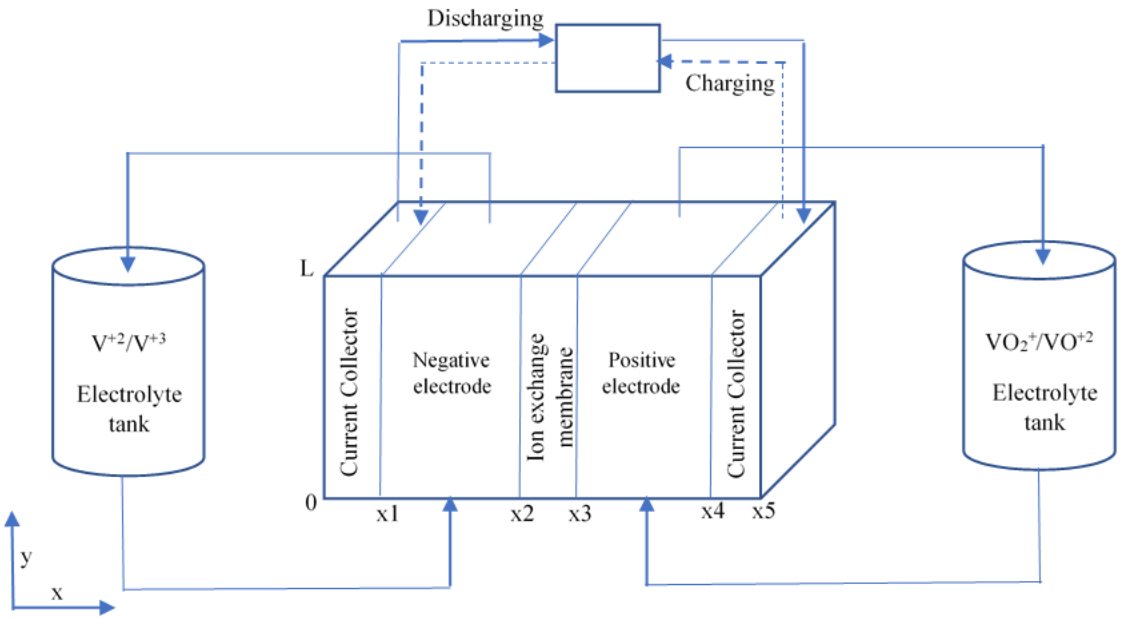

Figure 4.1. Schematic 2D model of Vanadium Redox Flow Battery

Half-cell reactions that take place in the positive and negative electrodes, respectively, are given by:

$$VO^{+2} + H_2O \leftrightarrow {VO_2}^+ + 2H^+ + e^- \qquad E^0 = 1.00V \quad (5.1)$$

$$V^{+3} + e^- \leftrightarrow V^{+2} \qquad E^0 = -0.26V \quad (5.2)$$

The overall cell reaction is given by:

$$VO^{+2} + H_2O + V^{+3} \leftrightarrow {VO_2}^+ + 2H^+ + V^{+2} \qquad E^0 = 1.25V \quad (5.3)$$

The forward reaction takes place during charging when V^{+3} and V^{+4} ions enter the cell. V^{+4} is oxidized to V^{+5} by releasing an electron which is removed by a conducting electrode material and a hydronium ion which moves across the membrane. At the anode, the electron reduces V^{+3} to V^{+2} and the hydronium ion offsets the overall charge of the half-cell. The ions leave the cell in charged state, as V^{+5} and V^{+2}. The reverse of charging occurs during discharge.

As mentioned before, along with the half-cell reactions a number of other reactions take place within the cell, which reduces the capacity of the cell subsequently. Following crossover reactions occur due to the transport of vanadium ions through the membrane:

Negative electrode:

$$VO^{+2} + V^{+2} + 2H^{+} \rightarrow 2V^{+3} + H_2O \quad (5.4)$$

$$VO_2{}^{+} + 2V^{+2} + 4H^{+} \rightarrow 3V^{+3} + 2H_2O \quad (5.5)$$

Positive electrode:

$$V^{+2} + 2VO_2{}^{+} + 2H^{+} \rightarrow 3VO^{+2} + H_2O \quad (5.6)$$

$$V^{+3} + VO_2{}^{+} \rightarrow 2VO^{+2} \quad (5.7)$$

Gaseous side reactions notably, evolution of oxygen at the positive electrode and evolution of hydrogen at negative electrode, are as follows:

$$2H_2O \leftrightarrow O_2 + 4e^{-} + 4H^{+} \quad (5.8)$$

$$2H^{+} + 2e^{-} \leftrightarrow H_2 \quad (5.9)$$

Along with these ion-crossover and side reactions, water transport through the membrane causes membrane degradation.

4.3. Governing Equations

4.3.1. Model assumptions

The following assumptions are made in developing the model:

- Dilute solution approximation
- Electrolyte flow – incompressible and laminar
- Gas bubbles do not coalesce, because of the repulsive electrical forces between the bubbles
- Non-expanding bubbles approximation is considered (gas-phase and liquid-phase pressures are equal)
- Overall momentum equation for gas-bubbles and electrolyte is approximated by the liquid
- Liquid and solid phases in electrodes are assumed to attain same temperature

Few equations considered here are from the literature [14], [136], [131], [162] and suitably modified based on the specific configuration and operating conditions considered in this work.

4.3.2. Porous carbon electrode

The volume averaged mass balance for porous carbon electrode is given by:

$$\frac{\partial}{\partial t}\left(\epsilon\left(1-\beta_g\right)c_i\right)+\nabla.\vec{N_i}=S_i \tag{5.10}$$

,where i is species V(II), V(III), V(IV), V(V), H^+, $HSO_4{}^-$, O_2 and H_2. S_i is the source term, given in Table 5.1. Concentration flux is given by Nernst-Planck equation [136][163] considering transport due to diffusion, convection and migration as follows:

$$\vec{N_i}=-D_i\epsilon^{3/2}\left(1-\beta_g\right)^{3/2}\nabla c_i-\frac{z_i c_i D_i F}{RT}\nabla\emptyset_e+\overrightarrow{v_l c_l} \tag{5.11}$$

Diffusivity of ions is given in Table C.1. in Appendix C. $SO_4{}^{-2}$ concentration is calculated using the condition of electroneutrality as shown below:

$$\sum_i z_i c_i=0 \tag{5.12}$$

Assuming the first step of dissociation is complete, and the second step is partially complete, the dissociation source term to maintain the correct ionic ratios is given as:

$$S_d=k_d\left(\frac{c_{H^+}-c_{HSO_4{}^-}}{c_{H^+}+c_{HSO_4{}^-}}-\theta\right) \tag{5.13}$$

The dissociation parameters are given in Table C.1. in Appendix C. The ionic (liquid) and electronic (solid) potentials are coupled through charge conservation equation as follows:

$$\nabla.\overrightarrow{J_e}=-\nabla.\overrightarrow{J_s}=j_\pm \tag{5.14}$$

$$\nabla.F\sum_i z_i\vec{N_i}=\nabla.\overrightarrow{J_e}=j_\pm \tag{5.15}$$

$$-\nabla.\sigma_s\nabla\emptyset_s=-\nabla.\overrightarrow{J_s}=j_\pm \tag{5.16}$$

Effective conductivity of carbon electrode, $\sigma_s=(1-\epsilon)^{3/2}\sigma_f$, where σ_f is the effective conductivity of solid material and is given in Table C.1. in Appendix C.

Current density equations in positive and negative electrode are given respectively, by the Butler-Volmer formulae as follows:

$$j_+=a\epsilon\left(1-\beta_g\right)F(c_4)^{\alpha_{o,+}}(c_5)^{\alpha_{r,+}}\left[k_+^o\left(\frac{{c_4}^s}{c_4}\right)\exp\left(\frac{F\alpha_{o,+}\eta_+}{RT}\right)-k_+^r\left(\frac{{c_5}^s}{c_5}\right)\exp\left(-\frac{F\alpha_{r,+}\eta_+}{RT}\right)\right] \tag{5.17}$$

$$j_{-} = a\epsilon\left(1-\beta_g\right)F(c_2)^{\alpha_{o,-}}(c_3)^{\alpha_{r,-}}\left[k_{-}^{o}\left(\frac{{c_2}^s}{c_2}\right)\exp\left(\frac{F\alpha_{o,-}\eta_{-}}{RT}\right) - k_{-}^{r}\left(\frac{{c_3}^s}{c_3}\right)\exp\left(-\frac{F\alpha_{r,-}\eta_{-}}{RT}\right)\right] \quad (5.18)$$

Table 4.1. Source term in positive and negative electrodes respectively

Source Term	Positive electrode	Negative electrode
S_2 (V(II) Concentration equation (mol/m^3)	N/A	$\frac{-j_{-}}{F} - \vec{N}_{cr,V_{+4}} - 2\vec{N}_{cr,V_{+5}}$
S_3 (V(III) Concentration equation (mol/m^3)	N/A	$\frac{j_{-}}{F} + 2\vec{N}_{cr,V_{+4}} + 3\vec{N}_{cr,V_{+5}}$
S_4 (V(IV) Concentration equation (mol/m^3)	$\frac{-j_{+}}{F} + 3\vec{N}_{cr,V_{+2}} + 2\vec{N}_{cr,V_{+3}}$	N/A
S_5 (V(V) Concentration equation (mol/m^3)	$\frac{j_{+}}{F} - 2\vec{N}_{cr,V_{+2}} - \vec{N}_{cr,V_{+3}}$	N/A
S_{H^+} (Proton concentration equation (mol/m^3)	$\frac{2j_{+}}{F} - 2\vec{N}_{cr,V_{+2}} - S_d$	$-2\vec{N}_{cr,V_{+4}} - 4\vec{N}_{cr,V_{+5}} - S_d$
$S_{HSO_4^-}$ (Bisulfate concentration equation (mol/m^3)	S_d	S_d
S_{H_2O} (Water concentration equation)	$-\frac{j_{+}}{F} + 7\vec{N}_{cr,V_{+2}} + 6\vec{N}_{cr,V_{+3}} - 5\vec{N}_{cr,V_{+4}} - 4\vec{N}_{cr,V_{+5}}$	$-6\vec{N}_{cr,V_{+2}} - 6\vec{N}_{cr,V_{+3}} + 6\vec{N}_{cr,V_{+4}} + 6\vec{N}_{cr,V_{+5}}$
S_{H_2} (H_2 Volume fraction equation (mol/m^3)	N/A	$m_{H_2}\nabla.\vec{J}_{H_2}/_F$
S_{O_2} (O_2 Volume fraction equation (mol/m^3)	$m_{O_2}\nabla.\vec{J}_{O_2}/_F$	N/A

The kinetic properties are given in Table 5.4. Overpotential in current density equations for positive and negative electrode respectively, is given as:

$$\eta_j = \emptyset_s - \emptyset_e - E_{0,j}$$

$$E_{0,+} = E^*_{0,+} + \frac{RT}{F}\ln\left(\frac{c_5 c_{H^+}^2}{c_4}\right) \quad (5.19)$$

$$E_{0,-} = E^*_{0,-} + \frac{RT}{F}\ln\left(\frac{c_2}{c_3}\right)$$

$E^*_{0,+}$and $E^*_{0,-}$ are the open circuit potentials and given in Table C.2. in Appendix C.

Considering the local mass transfer resistance, the surface concentration equations are given as follows for positive and negative electrode respectively:

$$ak_m(c_2 - c_2^s) = \frac{j_-}{F} \qquad ak_m(c_3 - c_3^s) = \frac{-j_-}{F} \quad (5.20)$$

$$ak_m(c_4 - c_4^s) = \frac{j_+}{F} \qquad ak_m(c_5 - c_5^s) = \frac{-j_+}{F} \quad (5.21)$$

The local transfer coefficient is related to the electrolyte velocity [14][126] and is given as,

$$k_m = 1.6 \times 10^{-4} v_l^{0.4} \quad (5.22)$$

State of charge is calculated as a function of concentration of vanadium ions as follows:

$$SOC_- = \frac{c_2}{c_2 + c_3}$$
$$SOC_+ = \frac{c_5}{c_4 + c_5} \quad (5.23)$$
$$SOC = \frac{c_2 + c_5}{c_2 + c_3 + c_4 + c_5}$$

4.3.3. Gas evolution in porous carbon electrode

The mass balance equation for gas evolution in electrode is given by:

$$\epsilon\rho_g \frac{\partial \beta_g}{\partial t} + \epsilon\rho_g \nabla.\left(\beta_g \overrightarrow{v_g}\right) = S_g \quad (5.24)$$

S_g is given in Table 5.1. The bubbles do not form a continuous phase. They are dispersed in the liquid. The volume fraction of the gas 'β_g' and the liquid electrolyte 'β_l' in a pore satisfies the following equation:

$$\beta_l = 1 - \beta_g \quad (5.25)$$

The liquid phase velocity was assumed to be constant in the electrodes. Gas phase velocity is estimated using slip velocity [136] and constant liquid phase velocity as follows:

$$\vec{v}_{slip} = \overrightarrow{v_g} - \overrightarrow{v_l} \quad (5.26)$$

$$\vec{v}_{slip} = \frac{{d_g}^2}{18\mu_l}\nabla p \tag{5.27}$$

The volumetric current density for gas evolution reactions is given in [136] as follows:

$$j_g = \pm a\epsilon\left(1-\beta_g\right)j_{0,g}\exp\left(\pm\frac{F\alpha_g\eta_g}{RT}\right) \tag{5.28}$$

,where $j_{0,g}$ is the exchange current density for the gas evolution reactions.

Total current density in negative electrode is equal to sum of current densities of the hydrogen gas evolved and the redox reactions.

$$\vec{j} = \vec{j}_- + 2\vec{j}_{H_2} \tag{5.29}$$

Total current density in positive electrode is equal to sum of current densities of the oxygen gas evolved and the redox reactions.

$$\vec{j} = \vec{j}_+ + 4\vec{j}_{O_2} \tag{5.30}$$

4.3.4. Water transport equations

Water transfer is introduced to investigate the effect of water transfer using Equation 5.10. The source term S_w is given in Table 5.1. However, for water the migration term is neglected in the concentration flux equation (Eq. 5.11).

4.3.5. Equations in membrane

Mass balance equation for concentration of charged species permeating through the membrane is given by:

$$\frac{\partial {c_i}^m}{\partial t} + \nabla.\vec{N_i}^m = 0 \tag{5.31}$$

,where ${c_i}^m$ is the concentration of species V(II), V(III), V(IV), V(V), H^+, H_2O in the membrane. Assuming the dissociation of ${HSO_4}^-$ is completely suppressed by the presence of the fixed charge in the membrane, ${SO_4}^{-2}$ is not present in the membrane. Concentration of ${HSO_4}^-$ is calculated using electroneutrality condition.

$$\sum_i z_i {c_i}^m = -z_f c_f \tag{5.32}$$

Current conservation equation in the membrane is used to find the ionic potential in the membrane:

$$\nabla j^m = F \sum_i z_i \nabla \vec{N_i}^m = 0 \tag{5.33}$$

4.3.6. Equations in pump

The change in concentration of species in the reservoir is given by:

$$V \frac{dC_i{}^{in}}{dt} = -w\left(C_i{}^{in} - C_i{}^{out}\right) \tag{5.34}$$

4.3.7. Boundary Conditions

Locations of the boundary are specified with respect to Figure 5.1. At the electrode current collector interface ($x = x_1$ and $x = x_4$) and along the top and bottom ($y = 0$ and $y = L$) of the membrane, the species flux is assumed to be zero.

$$0 = \begin{cases} -\vec{n}.\vec{N_i}^e, & x = x_1 \text{ and } x = x_4 \\ -\vec{n}.\vec{N_i}^m, & y = 0 \text{ and } y = L \end{cases} \tag{5.35}$$

At the bottom, at the inlet of the electrode ($y = 0$),

$$y = 0\ (inlets) \qquad c_i{}^e = c_i{}^{in}(t) \tag{5.36}$$

At the top, at the outlet of electrode ($y = L$),

$$y = L\ (outlets) \qquad 0 = \begin{cases} \vec{n}.D_i \epsilon^{3/2}\left(1 - \beta_g\right)^{3/2} \nabla c_i \\ \beta_g = 0 \end{cases} \tag{5.37}$$

The remaining cell, top and bottom of the electrode and membrane is considered to be electrically insulated.

$$0 = \begin{cases} -\vec{n}.\overrightarrow{j_s^e} \\ -\vec{n}.\overrightarrow{j_l^e} \\ -\vec{n}.\overrightarrow{j_l^m} \end{cases} \quad (y = 0 \text{ and } y = L) \tag{5.38}$$

Considering galvanostatic mode, the current is assumed to leave or enter uniformly through the current collectors. Therefore, at the electrode current collector interface the potential boundary condition is as follow:

$$-\vec{n}.\overrightarrow{j_s^e} = \begin{cases} 0, & x = x_1 \\ \dfrac{\pm I}{L w_{cell}}, & x = x_4 \end{cases} \tag{5.39}$$

Equation 5.39 is positive for charging and negative for discharging. At the negative electrode current collector interface ($x = x_1$), the solid potential is set to zero to use as reference potential.

As mentioned before, due to the Donnan effect at the membrane-electrode interface, though current and species flux are continuous, the ionic potential and species concentrations become discontinuous. Therefore, a set of boundary conditions have been developed to describe the mass transport at the interface. The electrochemical potentials at both sides of each ion are equal at the membrane electrode interface, which is given as:

$$\frac{c_i^m}{c_i^e} = \exp\left(z_i F \frac{(\emptyset_e - \emptyset_m)}{RT}\right) \tag{5.40}$$

The Donnan potential can be described as the difference between the ionic potential in membrane and the electrolyte at the interface.

$$\Delta\emptyset_d = \emptyset_e^m - \emptyset_e^e \tag{5.41}$$

Also, the concentration flux at the interfaces for all ions must be equal and is given as:

$$-D_i \epsilon^{3/2}\left(1-\beta_g\right)^{3/2}\nabla c_i - \frac{z_i c_i D_i F}{RT}\nabla\emptyset_e + \vec{v}_l c_i = -D_i^m \nabla c_i^m - \frac{z_i c_i^m D_i^m F}{RT}\nabla\emptyset_m + \vec{v}_i^m c_i^m \tag{5.42}$$

Since, electronic potential does not exist in the membrane, the interfacial conditions at membrane electrode interface ($x = x_2$ & $x = x_3$) are as follows:

$$-\vec{n}.\nabla\emptyset_s^e = 0 \quad (x = x_2 \text{ and } x = x_3) \tag{5.43}$$

The ionic potential as mentioned before is discontinuous, but the ionic flux is continuous at the membrane electrode interface. Therefore, the interfacial conditions for ionic potential at membrane electrode interface ($x = x_2$ & $x = x_3$) and the electrode current collector interface ($x = x_1$ & $x = x_4$) are as follow:

$$-\vec{n}.\overrightarrow{j_l^e} = \begin{cases} 0 \ , \ x = x_1 \text{ and } x = x_4 \\ -\vec{n}.\overrightarrow{j_l^m}, \ x = x_2 \text{ and } x = x_3 \end{cases} \tag{5.44}$$

4.4. Results and discussions

Three models were developed in Aspen Custom Modeler® V.8.4. One model considered the effect of ion-crossover mechanism, second considered the effect of ion-crossover and water transfer mechanisms and the third considered the effect of ion-crossover, water transfer and side reactions. Geometric details and operating conditions of the specific cell modeled are given in Table 5.2. In this work, the direction from negative electrode side to positive electrode side is believed as positive direction.

Table 4.2. Geometric properties and Operating conditions

Property	***Value***	***Units***	***References/ Comments***
Electrode thickness (l_e)	4	mm	[14]
Membrane thickness (l_m)	140	μm	[14]
Electrode height (h_e)	0.035	m	[161]
Electrode surface area (A)	10	cm^2	[14]
Electrode specific surface area (a)	10^4	m^2/m^3	[14]
Electrode porosity (ε)	0.93	N/A	[161]
Operating temperature (T)	25	^{0}C	[14]
Current (I)	± 0.4	A	[131]
Fixed charge concentration in membrane (c_f)	1280	mol/m^3	[160]
Fixed charge in membrane (z_f)	-1	N/A	[136]
Each tank volume (V)	60	mL	[14]

4.4.1. Model Validation

The model of a cell is validated with the data available in the literature. Figure 5.2.(a) shows the resemblance between the simulation and experimental under same operating conditions as those considered in ref [126] for an anion exchange membrane. During charging the cell potential increases with SOC and during discharge it decreases with the SOC. The calculated voltage is in good agreements with the measured data. The root mean squared error (RMSE) value between the model developed here and the experimental data [126] is ~0.00914 V.

Figure 5.2.(b) shows the comparison of the voltage for the model during charge/discharge cycling with experimental data [131] for cation-exchange membrane. To validate this model the operating and initial conditions are maintained same as the literature with a current density of 40 mA/cm^2 and the electrolyte composition of total vanadium concentration of 1040 mol/m^3 and total sulphate concentration of 5080 mol/m^3. It can be seen that the results agree well with the experimental data. The RMSE value during charging is ~0.0076 V whereas during discharge the RMSE is ~0.0124 V.

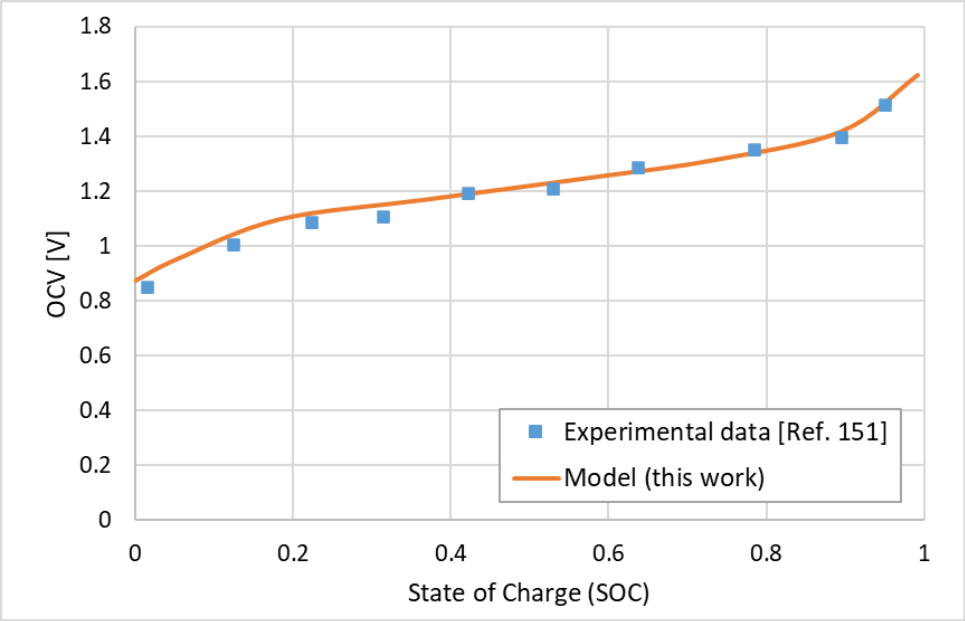

(a)

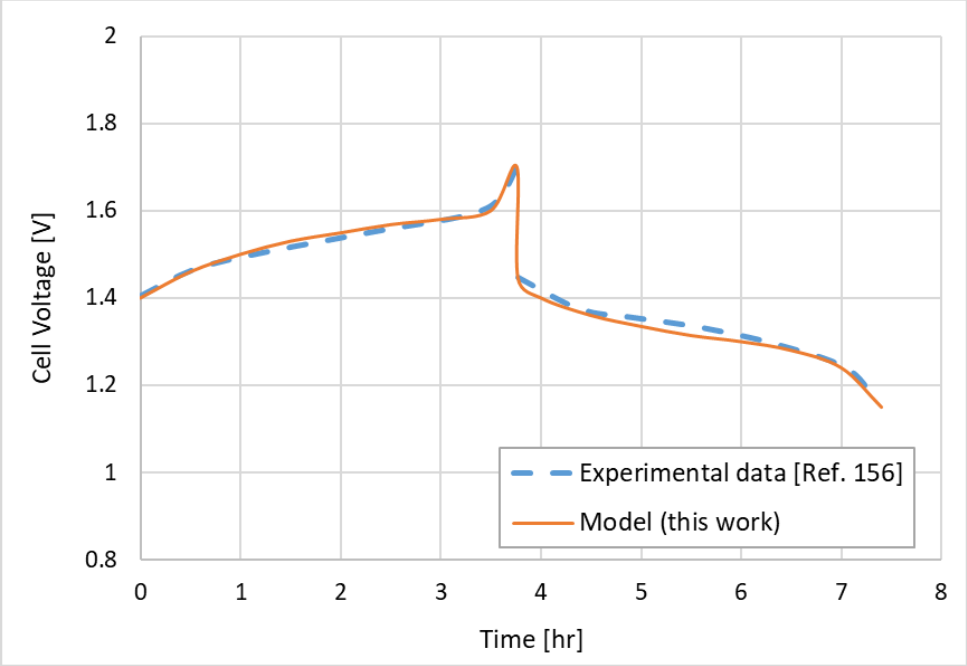

(b)

Figure 4.2. Comparison between model results and experimental data (a) from Wandschneider [126] **for OCV vs SOC (b) Knehr et al.** [131] **for cell voltage vs time during discharge/charge at +/- 0.4 A corresponding to a current density of 40 mA/cm^2 under same operating conditions as the measured**

4.4.2. Ionic potential distribution

Ionic potential profile at 0.5 SOC across the cell for a discharge current density of 40 mA/cm^2 is shown in Figure 5.3 under the open circuit condition. The dotted lines on figure represents the electrode membrane interface. It can be seen that the ionic potential at the positive electrode is less when compared to the negative electrode. This is because of the higher valency of cations at the negative side than the positive side, which increase the right-hand term in equation (5.15) for negative electrode compared to positive electrode.

The effect of Donnan potential jump at the membrane/electrode interface can also be seen clearly. There is a sharp decrease in the potential from both the electrodes to membrane side. This is because of the electroneutrality equations (5.12) and (5.32), which shows the effect of the presence of fixed charge in the membrane.

The undershoot is mainly to satisfy the equivalent ionic potential at the interface, where the potential is discontinuous. However, the effect of this undershoot appears only at the membrane electrode interface and does not affect the ion-crossover or water transfer behavior through the membrane.

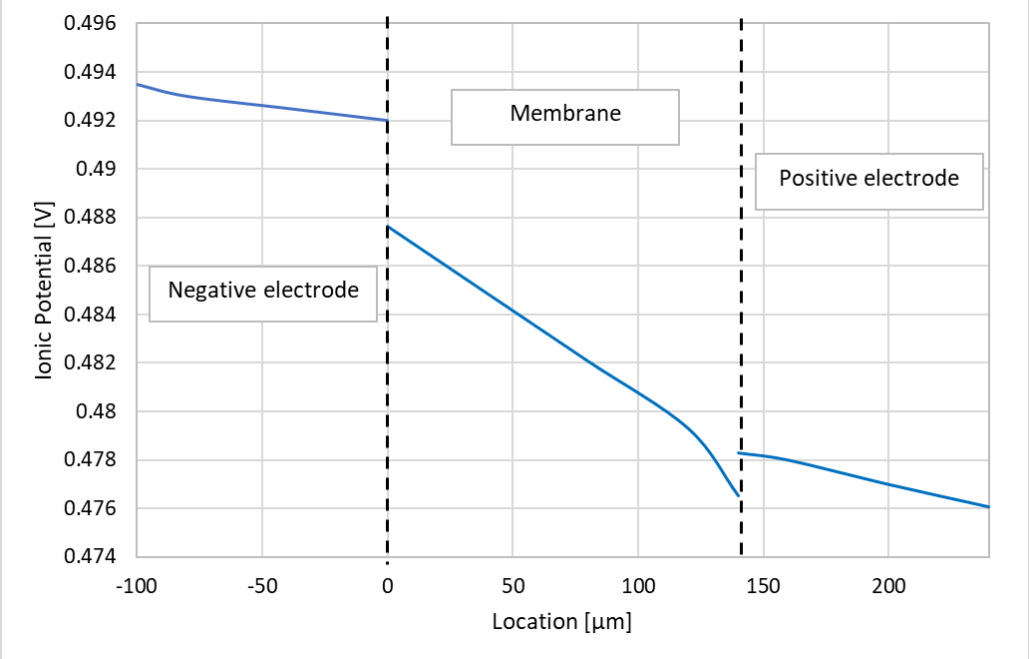

Figure 4.3. Ionic potential profile along the axis for 40 mA/cm^2 discharge current density at 0.5 SOC

4.4.3. Concentration distribution

The ion concentration profile in the membrane and electrodes is studied at a SOC of 0.5. Figure 5.4.(a) and (b) shows the concentration distribution for proton, HSO_4^- and the vanadium ions at a discharge current density of 40 mA/cm^2 and SOC of 0.5. The dotted lines on figure represents the electrode membrane interface. As mentioned before, the overshoot or undershoot of the concentration at the interface is due to the Donnan potential shown in equation (5.41) and considered in equation (5.40) while calculating the concentration at the interface. Vanadium ions transported through the membrane are assumed to be depleted at the opposite electrode interface.

It can be seen in figure 5.4.(a) that the positive side has higher proton and bi-sulphate concentrations than the negative side. This is because of the higher valence of the cations in the negative electrolyte, to satisfy the electroneutrality condition (equation (5.12)) on positive side the protons and bisulfate concentration becomes higher. Transfer of protons is dominated in cation exchange membrane. The proton diffusion movement towards the negative side is balanced by the electro-migration flux from the potential gradient in the reverse direction. This helps to keep the net current density zero at the open circuit condition.

Moreover, the positive current density during discharge promotes the V^{+2} and V^{+3} transfer through the membrane. Due to the opposite concentration gradient to the potential gradient under same operating conditions, the electric field will restrain the H^+transfer from the diffusion. This explains the reason for the convex concentration profile for V^{+2} and V^{+3} and concave concentration profile for H^+ in the membrane. Similarly, the profile shapes of the V^{+4}, V^{+5} and HSO_4^- can be evaluated based on the direction of the current and gradients.

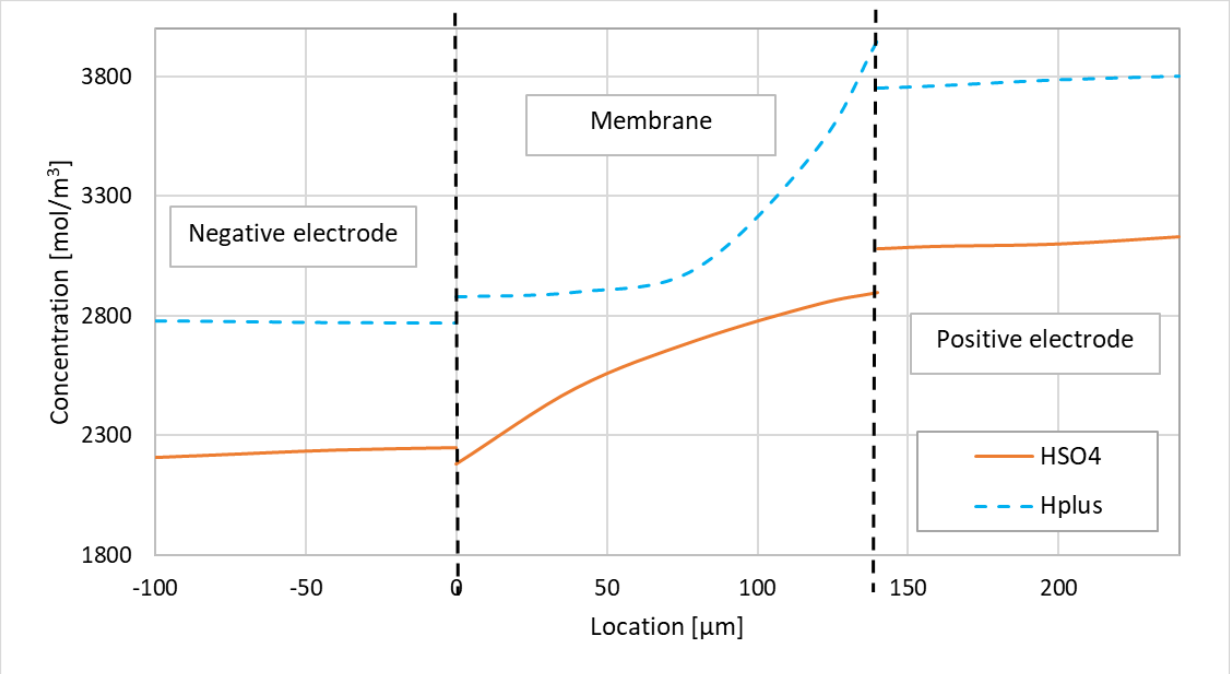

(a)

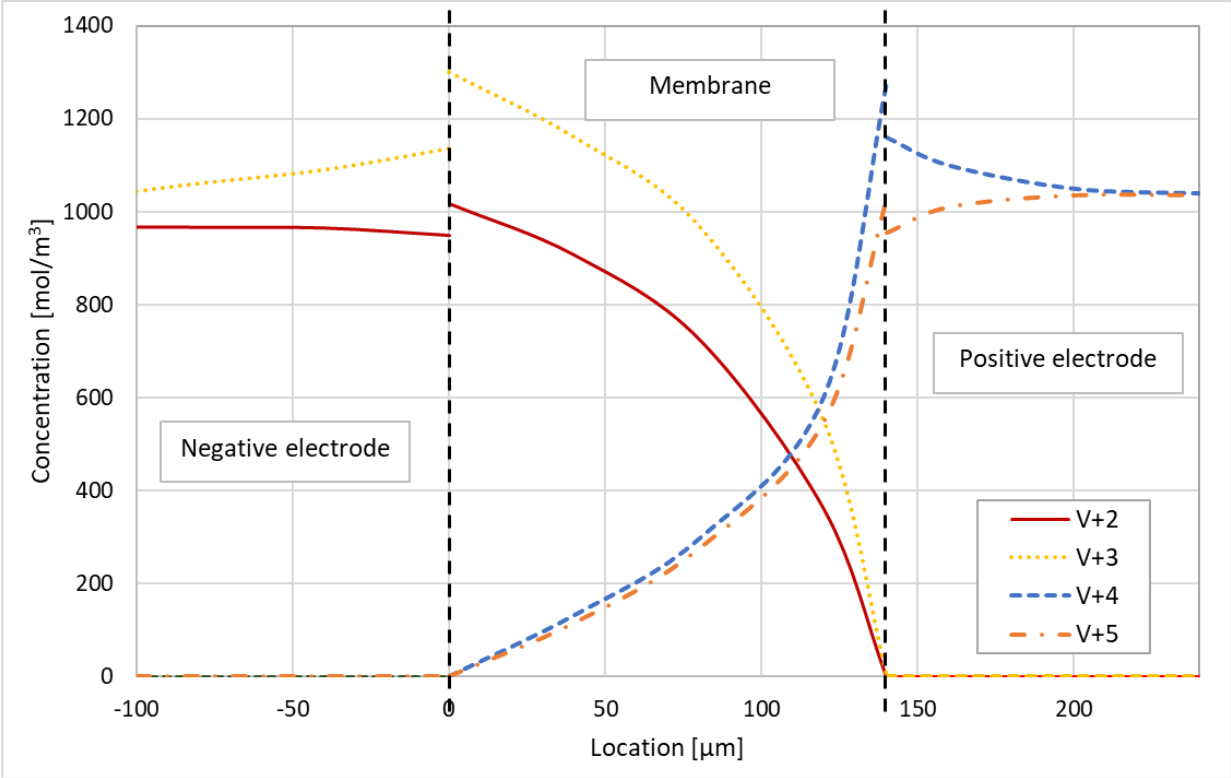

(b)

Figure 4.4. (a) H^+, HSO_4^- and (b) vanadium ions concentration distributions across the membrane for 40 mA/cm^2 discharge current density at 0.5 SOC

Figure 5.5. shows the vanadium ions profile during charge/discharge cycling during first 3 cycles at a current density of 40 mA/cm^2. It can be seen that the net vanadium concentration increases in negative side and decreases in positive side during charging. This shows a net vanadium crossover from positive to negative side. During discharging, reverse of this happens as a result of reverse electric field. As expected from equation (5.11), the species transport is governed by diffusion, migration and convection not only in the electrode but also through the membrane. The diffusivities of V^{+2} and V^{+3} are higher in membrane compared to V^{+4} and V^{+5}. This shows that the net diffusion is towards positive side during both charging and discharging. However, the migration and convective flux for positive ions is along the direction of ionic current, which is towards the negative side during charging and positive side during discharge. The net flux in equation (5.11) indicates the sum of diffusive, migrative and convective fluxes. Therefore, the net vanadium crossover flux towards negative side during charging is due to the higher value of combined flux due to migration and convection compared to the diffusive flux. Whereas, during discharge all three flux are in same direction resulting in a higher net flux compared to charging. This leads to an accumulation of vanadium ions in the positive side at the end of a cycle. As a result, the total vanadium ions concentration on positive side increases whereas for negative side it decreases as shown in Figure 5.5.

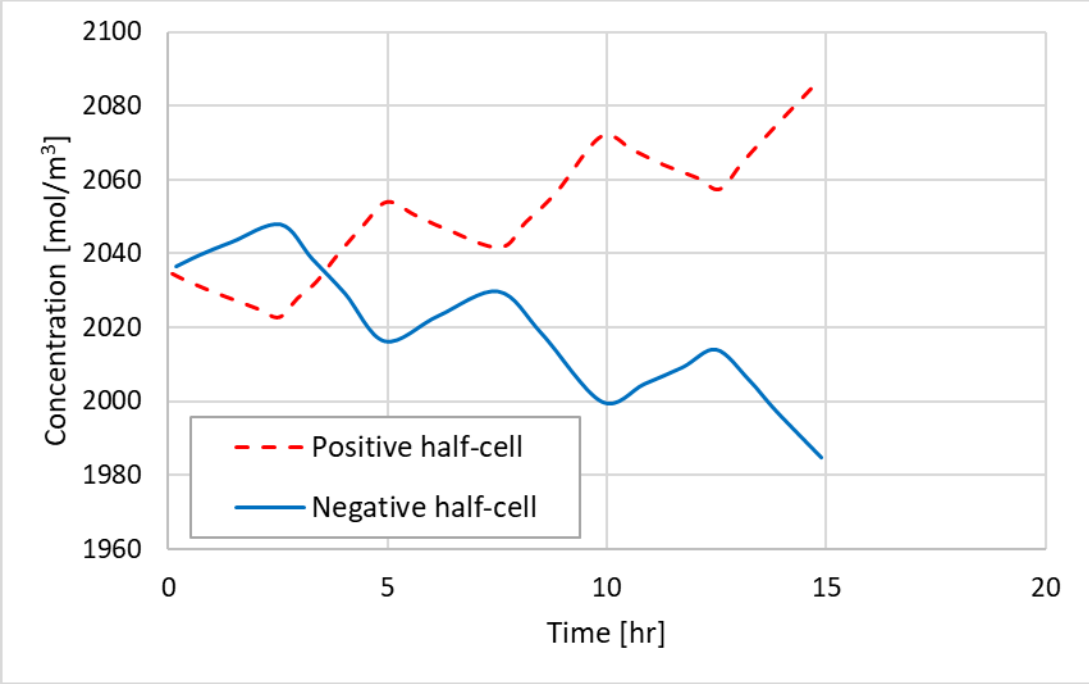

Figure 4.5. Net vanadium concentration profile over time in each half-cell during consecutive charging and discharging under 40 mA/cm^2 current density.

4.4.4. SOC distribution

Figure 5.6.(a) shows the SOC profile with time. As mentioned before in section 5.4.3, there is an imbalance in the net flux during charge and discharge. SOC is inversely related to the net vanadium concentration in the electrode respectively as shown in equation (5.23). As a result of the accumulation of ions at the end of a cycle, and increased ion concentration on the positive side results in a decreased value of SOC after each cycle as shown in figure 5.6.(a). There is higher increase in SOC for the negative side compared to the positive side as shown in figure 5.6.(b). This is mainly due to the accumulation of ions in positive side which decreases the net SOC value for positive electrode while increasing the SOC for negative electrode as expected.

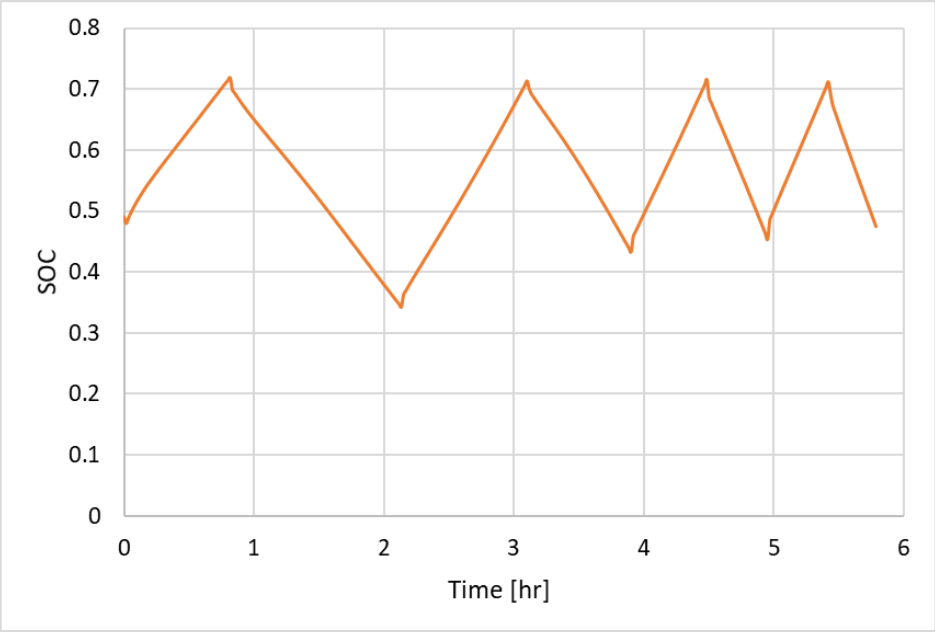

(a)

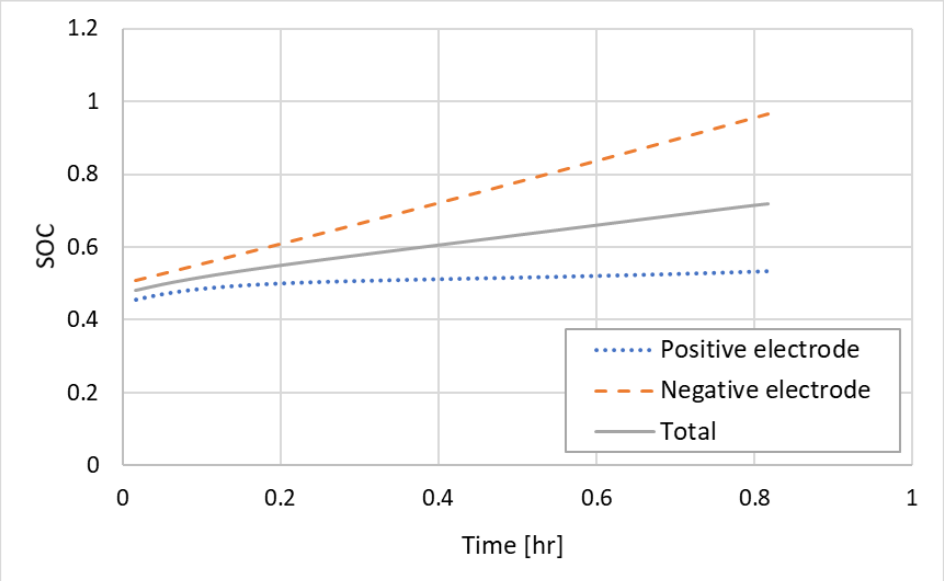

(b)

Figure 4.6. SOC distribution (a) for simultaneous charge discharge cycles at +/- 0.4 A (b) for positive electrode, negative electrode and the net SOC for charging at -0.4 A corresponding to a current density of 40 mA/cm^2

4.4.5. Sensitivity studies

Operating conditions can affect the dynamics of the VRFB cell. First, the impact of different current density is evaluated. Second, the impact of different flowrates is evaluated. Finally the impact of higher tank volume is evaluated.

4.4.5.1. Impact of current density

Current density is varied keeping the electrolyte flowrate constant. Figure 5.7 shows the variation of voltage and SOC with changing current density. It can be seen that as current density decreases during charging, the cell voltage increases and for higher current density the voltage decrease. This is because at high current density, higher flux of ions is required leading to an increase in the concentration and potential gradient leading to a decrease in the cell terminal voltage as would be expected by analyzing equations (5.10, 5.11 and 5.19). The profiles become opposite o during discharging.

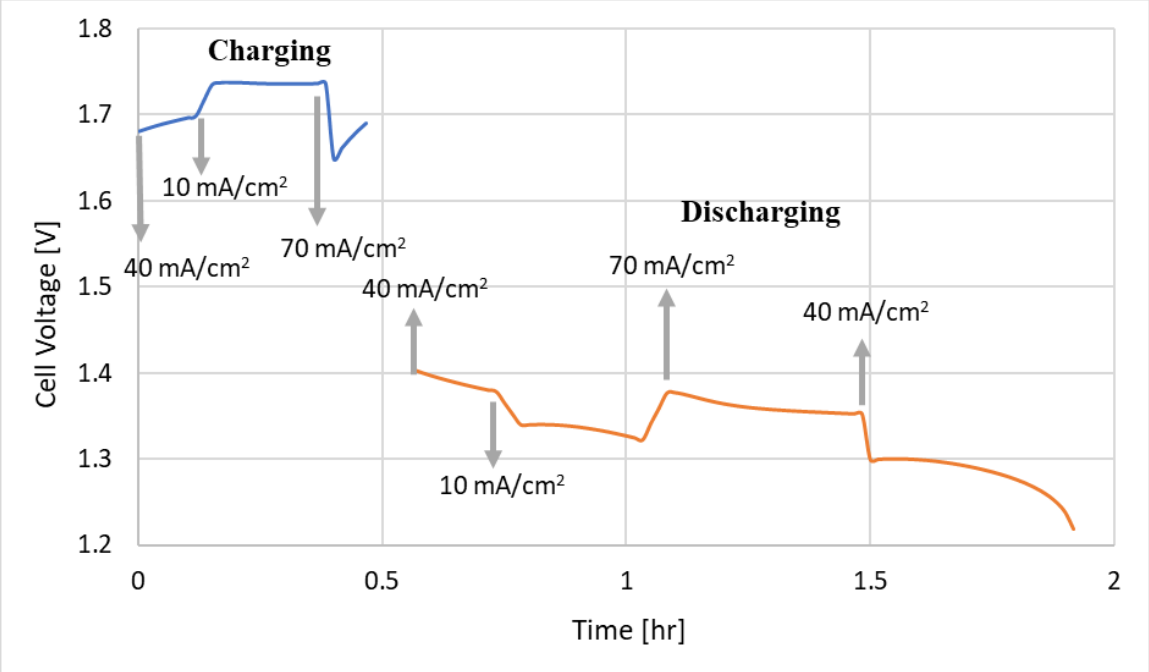

Figure 4.7. Cell Voltage with time for varying current density at 30 ml/min electrolyte flowrate

4.4.5.2. Impact of flowrate

Flowrate of electrolytes is varied keeping other variables constant to understand the dynamic dependence of flowrate on voltage. The flowrate is directly proportional to the rate at which vanadium ions enter the electrode. Thus, during charging, an increase in flowrate at the same current density leads to decrease in the concentration overpotential and therefore decrease in the cell voltage. Whereas during discharge reverse of this happens increasing the cell voltage. Moreover, for a higher flowrate, the contact time for the reactions in the electrode reduces, resulting in extended time for desired SOC. The reactants in the electrode are replaced more quickly from the reservoir, resulting in uniform overpotential and lower cell voltage at the end of charge.

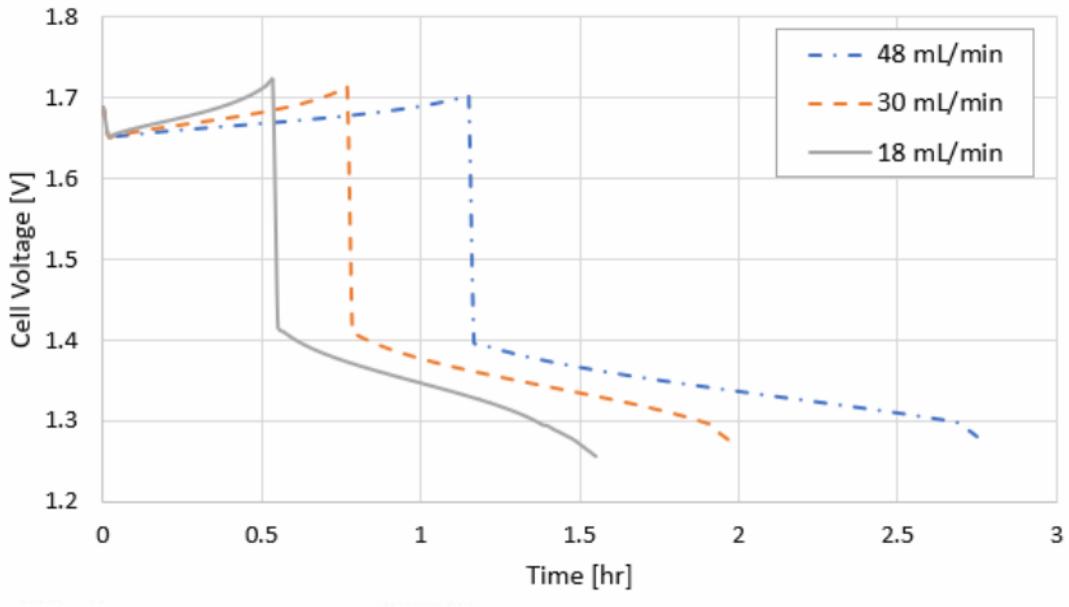

Figure 4.8. Cell Voltage with time for varying electrolyte flowrate at 40 mA/cm^2 current density

4.4.5.3. Impact of tank volume

For a current density of 40 mA/cm^2, with an electrolyte flowrate of 30 mL/min, the tank volume was varied to understand the sensitivity of the model with respect to the tank volume. Figure 5.9 shows the cell voltage profile for different tank volumes. The tank volumes considered here are same as the validated lab-scale model. The system sensitivity is tested based on the lab-scale

model. The model for both volumes of the reservoir is charged from 50% SOC to 73% SOC and then discharged from 73% to 35% SOC.

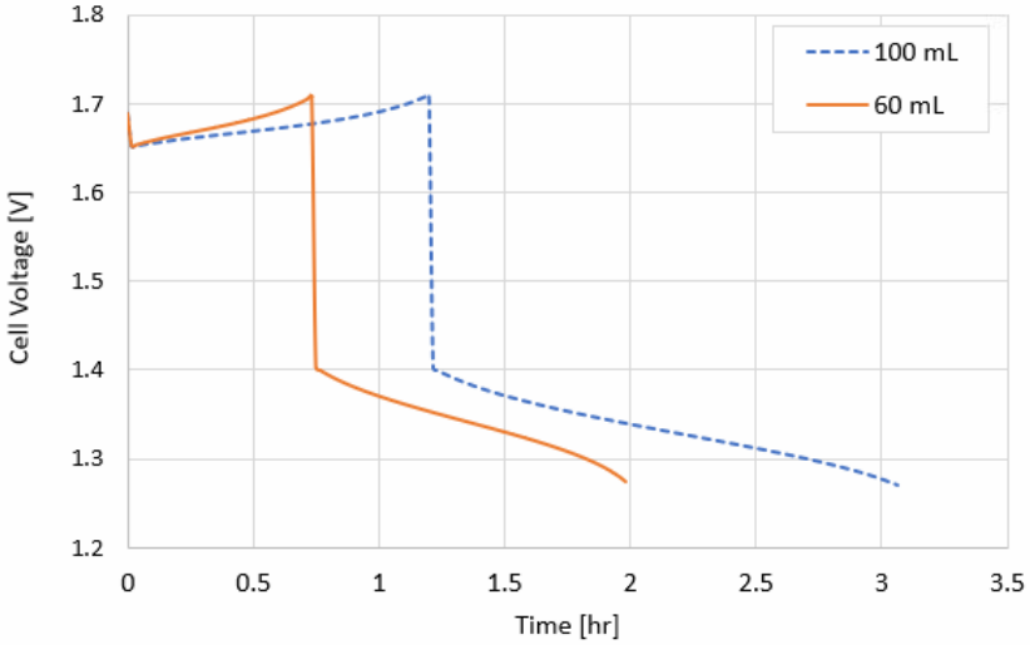

Figure 4.9. Cell voltage profile for different electrolyte tank volumes at 40 mA/cm^2 current density with a flowrate of 30 mL/min

It can be seen that during charging for higher tank volume the cell voltage is lower compared to the low tank volume. Whereas during discharge the cell voltage is higher for high tank volume. Moreover, it can be seen that as tank volume increases the time taken for charge and discharge increases. This is because, as the tank volume increases the vanadium ions available for the reaction increases.

4.4.6. Capacity loss

Capacity loss for three different mechanisms is shown in Figure 5.10. For this study, the tank capacity is 60 ml with a volumetric flow rate of 30 ml/min for both catholyte and anolyte and current density of 40 mA/cm^2 for a surface area of 10 cm^2 electrode. The model was simulated for more than 90 cycles and once the capacity was equal to 50%, the cell was considered to have reached the minimum capacity. This is often referred to in the literature as a capacity fade fault. Figure 5.10 shows the capacity as a function of charge discharge cycles. Initially only one mechanism, the self-discharge mechanism due to the crossover of vanadium ions, is considered.

In this case after 90 cycles the capacity was found to be nearly 76%. In the second case, self-discharge and gas evolution side reactions were considered. In this case after 90 cycles the capacity was found to be nearly 57%. In the last case three mechanisms, self-discharge, gas evolution and the water transport through the membrane were considered. In this case, after 90 cycles the capacity was found to be nearly 48%. Therefore, when we consider all the three capacity fade mechanisms the fault was detected at 87th cycle, if the cell is considered to be faulty when its capacity drops to below 50% for the first time.

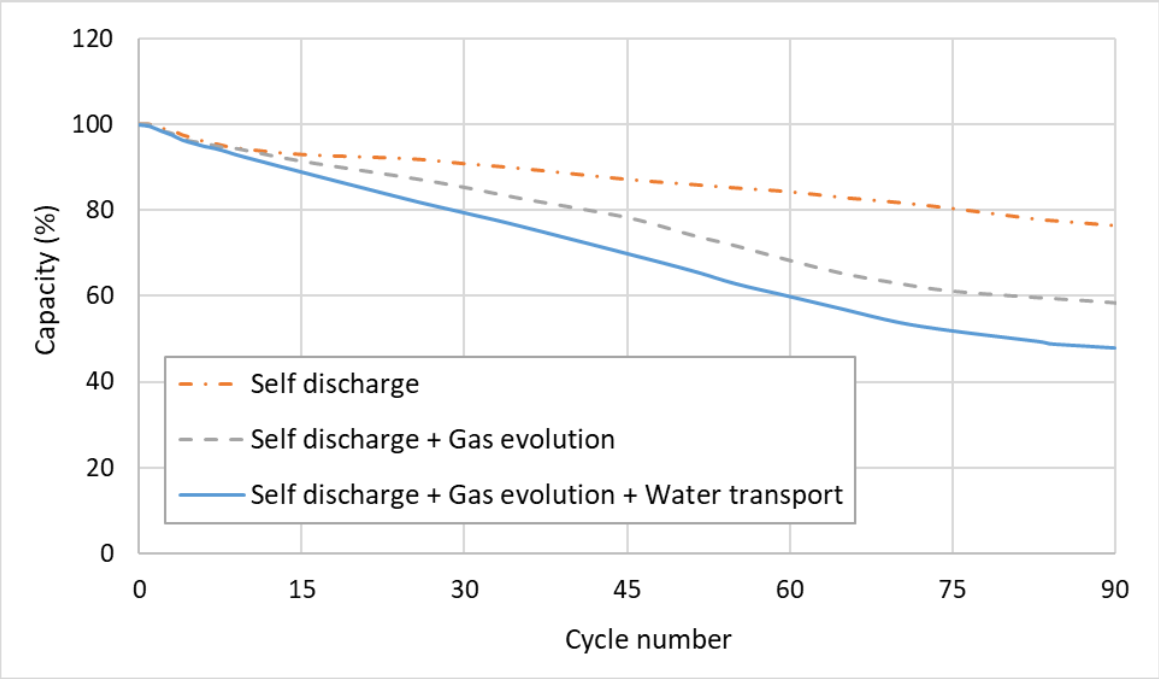

Figure 4.10. Comparison of capacity loss for different models considering different capacity loss mechanisms

In calculating the capacity, we assumed the tank capacity is 60 ml with a volumetric flow rate of 30 ml/min and current density of 40 mA/cm^2 for a surface area of 10 cm^2 electrode. Changing any of these values will affect the capacity of the battery. As discussed in sections 5.4.5.1 and 5.4.5.2, the current density and electrolyte flowrate also effects the performance of the cell. Therefore, an online model-based approach can be helpful to estimate/predict the time when the cell will become faulty. At the faulty condition, cell operation needs to be stopped and tanks mixed up, redistributed. This helps to bring back the concentration as before [111].

4.5. Conclusions

An isothermal, a transient model of a VRFB with an ion-exchange membrane considering ion-crossover, water transfer through the membrane and side-reactions was developed. The dynamic model considering ion-crossover mechanism was validated for anion-exchange membrane and cation exchange membrane over SOC. The results from the model were found to agree well with the experimental data. Due to the difference in valances, the ionic potential at the positive electrode is less when compared to the negative electrode. The effect of Donnan potential drops the ionic potential at the membrane electrode interfaces compared to the electrode ionic potential. This drop satisfies the equivalent ionic potential at the interface, where the potential is discontinuous. The positive side has higher proton and bi-sulphate concentrations than the negative side, because of the higher valence of the cations in the negative electrolyte compared to positive electrolyte. The proton diffusion towards the negative side is balanced by the electro-migration flux. The concentration profile for HSO_4^-, V^{+2} and V^{+3} are convex and concave for H^+, V^{+4} and V^{+5} in the membrane. There is an accumulation of vanadium ions in the positive side as the cell keeps cycling. This is because of the imbalance in the net flux during charging and discharging.

It was observed that cell voltage profile can change considerably depending on the current density, electrolyte flow rate and whether the cell is charging or discharging. The cell voltage profile was observed to increase during charge and decrease during discharge. It was observed that as the current density is increased, cell voltage can decrease or increase if the cell is charging or discharging. If the electrolyte flowrate is increased keeping the current density constant, the cell voltage decreases during charging and increases during discharging. It was observed that as the tank volume increases, the time taken to charge/discharge increases as expected for a given current density.

When all three capacity fading mechanisms are considered, it leads to considerably faster fading of capacity reaching a capacity less than 50% after 87th cycle considering a lab-scale storage of 60 ml, a volumetric flow rate of 30 ml/min, and current density of 40 mA/cm^2 for a surface area of 10 cm^2 electrode.

Chapter 5. Condition Monitoring of Vanadium Redox Flow Batteries through Co-estimation of Capacity Fade and State of Charge

5.1. Literature Review

As mentioned in chapter 5, VRFB has high potential especially for grid level energy storage. Till date, lots of efforts have been made to improve the efficiency and performance of VRFB, mostly considering different electrolytes, membranes and optimizing the design [122], [164], [165]. However, one of the challenges of VRFBs are faster capacity fade than many other secondary batteries like Li-ion, NaS batteries. While much of the capacity fade can be reversed be remixing electrolyte or electrolyte balancing, the cell may not be available for charging/discharging during that operation. Thus, for grid connected VRFBs where reliability and availability are of utmost importance, it would be desired to estimate capacity fade and state of the system simultaneously. This helps in avoiding complete damage to the system by remixing the electrolytes [111], [139] before the fault condition is obtained. Fault, in this work, is defined as the condition where the capacity has faded below certain range, when normal functioning of the cell is not possible anymore.

(Maximum) Capacity and SOC are critical to indicate the remaining life of the battery and they depend on each other. SOC is the percentage of residual capacity to maximum capacity. As mentioned in Chapter 5, many factors, like side reactions, ion crossover, water transport through the membrane, result in capacity degradation. Firstly, due to the ion crossover of vanadium ions, self-discharge reactions occur at the membrane electrode interface. The different diffusivities and valences of ions causes an increase of vanadium ions in one half cell and decrease in other [111], [129], [166]. This imbalance of vanadium ions results in asymmetric profile of SOC and decrease in capacity. Secondly, along with the vanadium ions, water bound to the vanadium ions, transfers through the membrane which can cause flooding in one of the half-cells due to the imbalance created by crossover of vanadium ions [111], [129], [166], [162]. Thirdly, gaseous side reactions decrease the available surface area for the electrochemical reactions affecting the imbalance in vanadium ions oxidation states and therefore the SOC, which results in capacity loss [111], [136]. The capacity loss in VRFB can be restored by partially remixing the two half-cells, operating within optimal SOC limits and preventing oxidation in negative half-cell by sealing the reservoir

[139]. However, poor design or operating conditions leads to side gaseous reactions, resulting in imbalance in SOC's and degradation in capacity which could be irreversible by remixing of electrolytes. This needs further geometric modifications and electrochemical rebalancing. Therefore, monitoring/estimating the capacity loss and SOC, helps in making a decision on when to instruct the remixing or rebalancing of electrolytes.

The coulomb counting (CC) is a traditional way to estimate SOC. However, as an open loop method, this method can suffer from initialization and measurement error. Skyllas-Kazacos et al. [121] evaluated electrolyte conductivity and spectrophotometric properties to determine the SOC. However, this approach is not suitable for real-time applications. Li et al. [167] used electrolyte viscosity, that could be estimated based on pressure drop, to estimate the SOC. Though this model is insightful for online monitoring, change in operating conditions and properties other than viscosity can also lead to an increase the pressure drop resulting in inaccurate measurements. The model-based observers can be very accurate in estimation of SOC. In this method, a battery model of varying level of complexity is used [168], [169]. Using the measured inputs and outputs, desired state variables are estimated [170]. Depending on the type of model and observer algorithms, tradeoffs between computational speed and accuracy can be considered for real-time application. Physics based mathematical models can be used in observed-based approaches for condition monitoring [134], [135], [171]. However, if the models are computationally expensive, that can restrict their use in real-time. Tang et al. [172] proposed a simplified mathematical model by considering the key processes of VRFB. But the model parameters are to be determined analytically based on many factors like SOC, current direction, operating temperature etc.,. Overlooking the physics and chemistry of battery systems, one popular approach is to use equivalent circuit models [ECM] [144]–[146]. Lately, taking into account the polarization effects of VRFB, first-order [150]–[152] and second order [147], [149], [173] RC (resistance capacitance) equivalent circuit models were developed. Skyllas-Kazacos and Wei [148] developed an extended Kalman filter (EKF) approach to estimate SOC online using an ECM model. Following this, Skyllas-Kazacos and Wei [121] also estimated capacity fade utilizing a sliding mode observer (SMO). However, the effect of operating conditions and capacity fade on model parameters was not considered in these papers, which can result in inaccuracy in the prediction.

As mentioned before, capacity is another important variable to be monitored. To date many mathematical models have been developed to predict the capacity loss [11], [130], [134], [135], [137], [174]. The effects of hydrogen evolution [134] and oxygen evolution [135] were modelled. Further Skyllas-Kazacos and Goh [130] developed a model considering the diffusion of vanadium ions across the membrane to predict the capacity loss. Following this, a model incorporating both ion crossover and side reactions was developed [11]. The SMO developed by Skyllas-Kazacos and Wei [121] was evaluated for estimating the capacity fade. However, for all these models, the accurate calibration of model parameters is difficult within different operating conditions. The battery systems contain large noise, sensor flaws and electromagnetic interference. Moreover, these models used experimental data to determine the parameters. This leads to inaccuracies since the effect of capacity fade on the model parameters is neglected. Therefore, the real-time co-estimation of SOC and capacity should be further elaborated for safe and efficient operation of VRFB.

A detailed 2D electrochemical model developed in Chapter 5 incorporating the capacity fading mechanisms is used here for developing a filtering approach for simultaneously estimating SOC and capacity. An autoregressive exogenous (ARX) model is developed where the order of the model is selected based on the Akaike information criterion (AIC) that penalizes overfitting. The state space model is used in the Kalman filter (KF) to co-estimate the SOC and capacity fade. The model developed in Chapter 5 is used to study the accuracy and effectiveness of the proposed method.

5.2. Battery modelling and identification

5.2.1. Battery model

The VRFB considered in this study consists of an ion-exchange membrane, separating the positive electrode and negative electrode. The system contains two tanks and two pumps connected to the negative electrode and positive electrode respectively, for the electrolyte flow. A detailed 2D model is developed considering the capacity degradation because of ion crossover, gaseous side reactions and water transfer through the membrane. More details regarding the model are available in Chapter 5. A summary of the governing equations is given in Table 6.1.

The half-cell reactions that take place in the positive and negative electrodes, respectively, are given by:

$$VO^{+2} + H_2O \leftrightarrow VO_2{}^{+} + 2H^{+} + e^{-} \qquad E^0 = 1.00V \quad (6.1)$$

$$V^{+3} + e^{-} \leftrightarrow V^{+2} \qquad E^0 = -0.26V \quad (6.2)$$

The overall cell reaction is given by:

$$VO^{+2} + H_2O + V^{+3} \leftrightarrow VO_2{}^{+} + 2H^{+} + V^{+2} \qquad E^0 = 1.25V \quad (6.3)$$

The following crossover reactions occur due to the transport of vanadium ions through the membrane:

Negative electrode:

$$VO^{+2} + V^{+2} + 2H^{+} \rightarrow 2V^{+3} + H_2O \quad (6.4)$$

$$VO_2{}^{+} + 2V^{+2} + 4H^{+} \rightarrow 3V^{+3} + 2H_2O \quad (6.5)$$

Positive electrode:

$$V^{+2} + 2VO_2{}^{+} + 2H^{+} \rightarrow 3VO^{+2} + H_2O \quad (6.6)$$

$$V^{+3} + VO_2{}^{+} \rightarrow 2VO^{+2} \quad (6.7)$$

Gaseous side reactions notably, the evolution of oxygen at the positive electrode and evolution of hydrogen at negative electrode takes place.

$$2H_2O \leftrightarrow O_2 + 4e^{-} + 4H^{+} \quad (6.8)$$

$$2H^{+} + 2e^{-} \leftrightarrow H_2 \quad (6.9)$$

Along with these ion-crossover and side reactions, water transport through the membrane causes membrane degradation.

These equations were used to develop three models, one with ion crossover mechanism, one with ion crossover and water transport and last with ion crossover, water transport and side reactions. In this work the ion crossover model is used.

Table 5.1. Governing equations for VRFB

Equations	Governing equations	Boundary conditions
Electrode		
Volume averaged mass balance equation	$\frac{\partial}{\partial t}\left(\epsilon\left(1-\beta_g\right)c_i\right)+\nabla.\vec{N}_i=S_i$	$@\ y=0$ $c_i{}^e=c_i{}^{in}(t)$ $@\ y=L$ $\vec{n}.D_i\epsilon^{3/2}\left(1-\beta_g\right)^{3/2}\nabla c_i=0$ $@\ x=\ x_1$ and $x=\ x_4$ $-\vec{n}.\vec{N}_i{}^e=0$ $@\ x=\ x_2$ and $x=\ x_3$ $-D_i\epsilon^{3/2}\nabla c_i-\frac{z_ic_iD_iF}{RT}\nabla\emptyset_e+\overrightarrow{v_lc_l}=$ $-D_i^m\nabla c_i^m-\frac{z_ic_i^mD_i^mF}{RT}\nabla\emptyset_m+\overrightarrow{v_i^mc_l^m}$
Charge conservation equations	$\nabla.\overrightarrow{J_e}=-\nabla.\overrightarrow{J_s}=j_\pm$ $\overrightarrow{J_e}=F\sum_i z_i\vec{N}_i$ $\overrightarrow{J_s}=\sigma_s\nabla\emptyset_s$	$@\ y=0$ and $y=L$ $-\vec{n}.\overrightarrow{J_l^e}=0$ $-\vec{n}.\overrightarrow{J_s^e}=0$ $-\vec{n}.\overrightarrow{J_s^e}=\begin{cases}0\ , & x=\ x_1\\ \frac{I}{Lw_{cell}}, & x=\ x_4\end{cases}$ $@\ x=\ x_2$ and $x=\ x_3$ $-\vec{n}.\overrightarrow{J_l^e}=-\vec{n}.\overrightarrow{J_l^m}$
Mass balance equation for gas evolution	$\epsilon\rho_g\frac{\partial\beta_g}{\partial t}+\epsilon\rho_g\nabla.\left(\beta_g\overrightarrow{v_g}\right)=-S_g$	$@\ y=0$ $\beta_g=0$
Membrane		
Volume averaged mass balance equation	$\frac{\partial c_i{}^m}{\partial t}=-\nabla.\vec{N}_i{}^m$	$@\ y=0$ and $y=L$ $-\vec{n}.\vec{N}_i{}^m=0$ $@\ x=\ x_2$ and $x=\ x_3$ $\frac{c_i^m}{c_i^e}=\exp\left(z_iF\frac{(\emptyset_e-\emptyset_m)}{RT}\right)$

(‘contd.)

Charge conservation equation	$\nabla {j_l}^m = F\sum_i z_i \nabla {\vec{N}_i}^m = 0$	@ $y = 0$ and $y = L$ $-\vec{n}.\overrightarrow{j_l^m} = 0$ @ $x = x_2$ and $x = x_3$ $\emptyset_m = \emptyset_e + \frac{RT}{Fz_i}\ln\left(\frac{c_i^m}{c_i^e}\right)$
Pump		
Change in concentration of species	$\frac{d{C_i}^{in}}{dt} = \frac{w}{V}\left({C_i}^{out} - {C_i}^{in}\right)$	N/A

5.2.2. Reduced Order Model Development

As mentioned before, model parameters are affected by several operating factors, SOC, capacity fade etc. System identification is crucial to mitigate the uncertainties and to maintain modeling efficiency and accuracy. This also helps to identify the order of the model.

The regression model is solved using ARX model which is implementable in real-time entrenched systems due to low computational efficiency. Akaike information criterion (AIC) helps in overfitting. The algorithmic procedure of ARX is given in Table 6.2.

Table 5.2. Algorithmic procedure for ARX

Step 1: ARX dynamic form For $k = 1,2, \ldots..$ $$x(k) = \sum_{i=0}^{n} H_1(i)u(k-i) + \sum_{j=1}^{r} H_2(j+n)x(k-j)$$
Step 2: Linear least square estimate formulation $$H = {(\varphi^T\varphi)}^{-1}\varphi^T X$$ $$x(k) = \varphi(k)H$$
Step 3: AIC criterion (after system identification, to find the good fit) $$AIC = Nln\left(\frac{TSE}{N}\right) + 2K$$

5.3. Co-estimation of capacity and SOC

The essential and functioning techniques of KF are introduced followed by a closed loop observer based on KF is developed for estimating capacity and SOC.

5.3.1. Kalman filtering

The Kalman filter helps to estimate the states such as SOC and capacity given the measurement of voltage. Since the process is very well represented by a linear model, the traditional KF is adequate for the state estimation. This is also reflected by the excellent performance of the KF. Kalman filtering uses a sequence of measurements observed over time, with a noise to produce a prediction of unknown variables. The algorithm includes a set of recursive mathematical equations to estimate the values of state variables. By minimizing the mean squared error, the obtained estimation is assumed to be optimum for a linear system. The estimation framework for KF is formulated as follows:

$$x_k = Ax_{k-1} + Bu_{k-1} + \omega_{k-1} \tag{6.10}$$

$$y_k = Cx_k + v_k \tag{6.11}$$

,where ω_k and v_k are the process and measurement noise that are assumed to be normally distributed and are independent. The algorithmic approach for KF is given in Table 6.3.

5.3.2. State estimation using KF

The state vector considered here is as follows: $x = [Q_k \quad V_k \quad SOC_k]$, where Q is the capacity of the cell and V is the voltage of the cell, with input vector as $u = [I_k \quad I_{k-1} \quad w_k \quad w_{k-1}]$, where I is the current and w is the electrolyte flowrate. Voltage is considered to be the only output for this system.

With the estimated parameters the state space model can be written as:

$$\begin{bmatrix} x_Q(k) \\ x_V(k) \\ x_{SOC}(k) \end{bmatrix} = \begin{bmatrix} a_q & a_{q,v} & 0 \\ 0 & a_v & 0 \\ 0 & a_{s,v} & a_s \end{bmatrix} \begin{bmatrix} x_Q(k-1) \\ x_V(k-1) \\ x_{SOC}(k-1) \end{bmatrix} + \begin{bmatrix} b_{q,I(k)} & b_{q,I(k-1)} & b_{q,w(k)} & b_{q,w(k-1)} \\ b_{v,I(k)} & b_{v,I(k-1)} & b_{v,w(k)} & b_{v,w(k-1)} \\ b_{s,I(k)} & b_{s,I(k-1)} & b_{s,w(k)} & b_{s,w(k-1)} \end{bmatrix} \begin{bmatrix} I_k(k) \\ I_k(k-1) \\ w_k(k) \\ w_k(k-1) \end{bmatrix} + w_k \tag{6.12}$$

$$y_V(k-1) = [0 \quad 1 \quad 0] \begin{bmatrix} x_Q(k-1) \\ x_V(k-1) \\ x_{SOC}(k-1) \end{bmatrix} + v_k \tag{6.13}$$

All the parameters are determined by fitting the data as discussed in section 6.2.2.

Table 5.3. Algorithmic procedure for Kalman filter

Define parameters:	
A, B and C	
Initialize x_{k-1}, P_{k-1}	
For $\boldsymbol{k = 1, 2}$, ...	
a priori state estimate:	$x_k^- = Ax_{k-1} + Bu_{k-1}$
a priori error covariance:	$P_k^- = AP_{k-1}A^T + Q$
Kalman gain:	$K_k = P_k^- H^T (HP_k^- H^T + R)^{-1}$
a posteriori state estimate:	$x_k = x_k^- + K_k(z_k - Hx_k^-)$
a posteriori error covariance:	$P_k = (I - K_k H)P_k^-$

This algorithm can simultaneously predict the state variables. Since we included SOC and capacity in our state variables, we can co-estimate them. This method is based on assumption that measurements of inputs, i.e., current, electrolyte flowrate, and output, the voltage, are available.

5.4. Results and discussions

MATLAB was used in simulation of these models.

5.4.1. Model development and validation

A 2D electrochemical model was developed considering ion-crossover through the membrane in previous chapter. More details about model validation are given in section 5.4.1.

5.4.2. ARX model development

5.4.2.1. Input-Output data

To identify the ARX model, a pseudorandom binary sequence (PRBS) is generated. PRBS is a binary sequence, which is generated using a deterministic algorithm and can show geometric behavior similar to a true random sequence. The generated PRBS is implemented for the inputs current and electrolyte flowrate with an amplitude of 0.1 A and 10^{-7} m^3/sec, respectively. Parameter estimation was performed in MATLAB. Figure 6.1 shows the input and output data generated from the 2D model in ACM.

It can be seen that as the current and flowrate fluctuates the voltage also changes correspondingly as discussed in section 5.4.5. This in turn affects the SOC and capacity. The change is SOC as voltage changes is visible in Figure 6.1, whereas for the capacity reduction the change is with respect to the rate at which the capacity decreases.

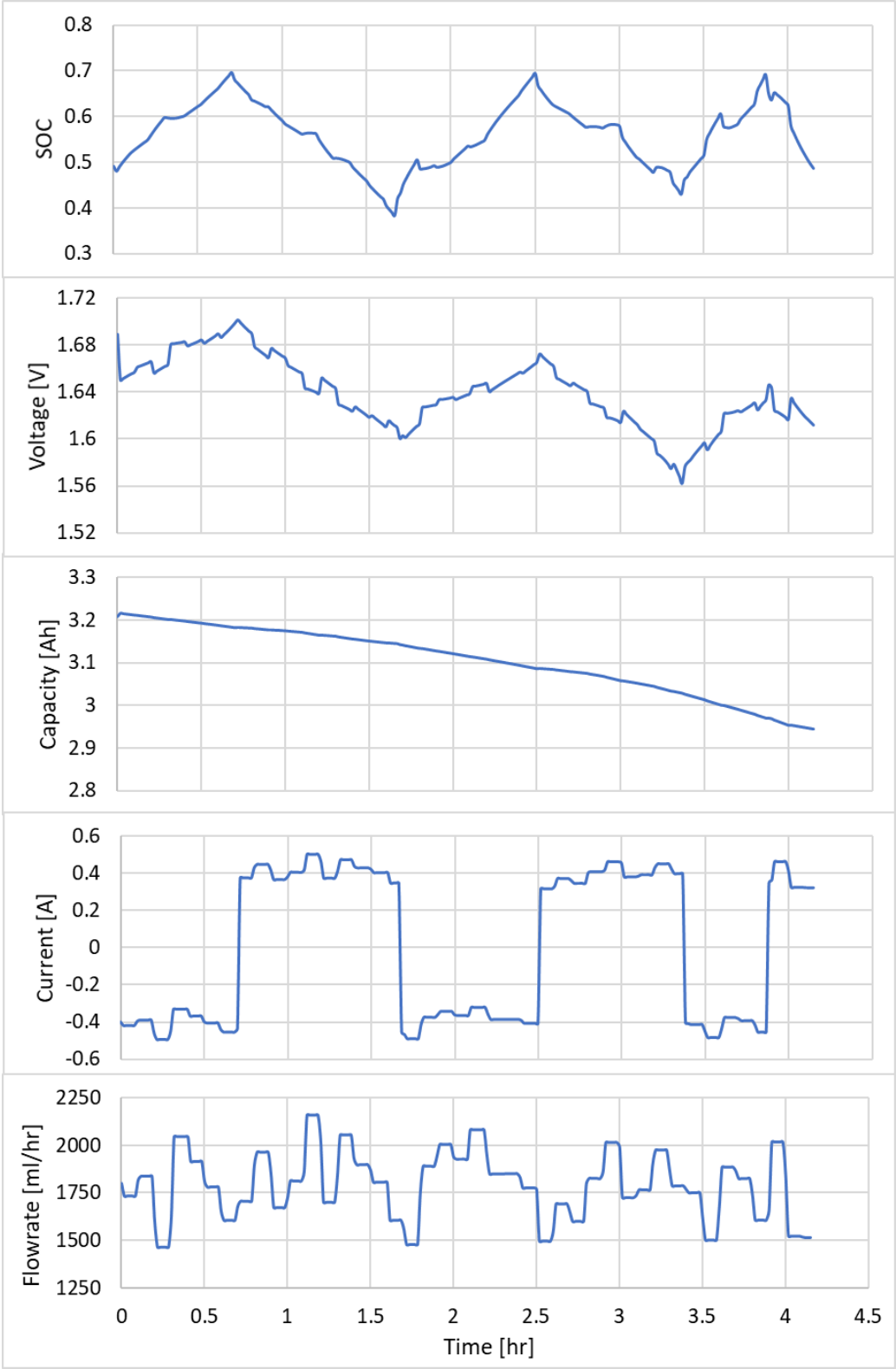

Figure 5.1. Input-Output data from the validated 2D model in ACM for varying current and electrolyte flowrate

5.4.2.2. Model validation

The input-output data presented in the previous section is used for linear lest squares parameter estimation.

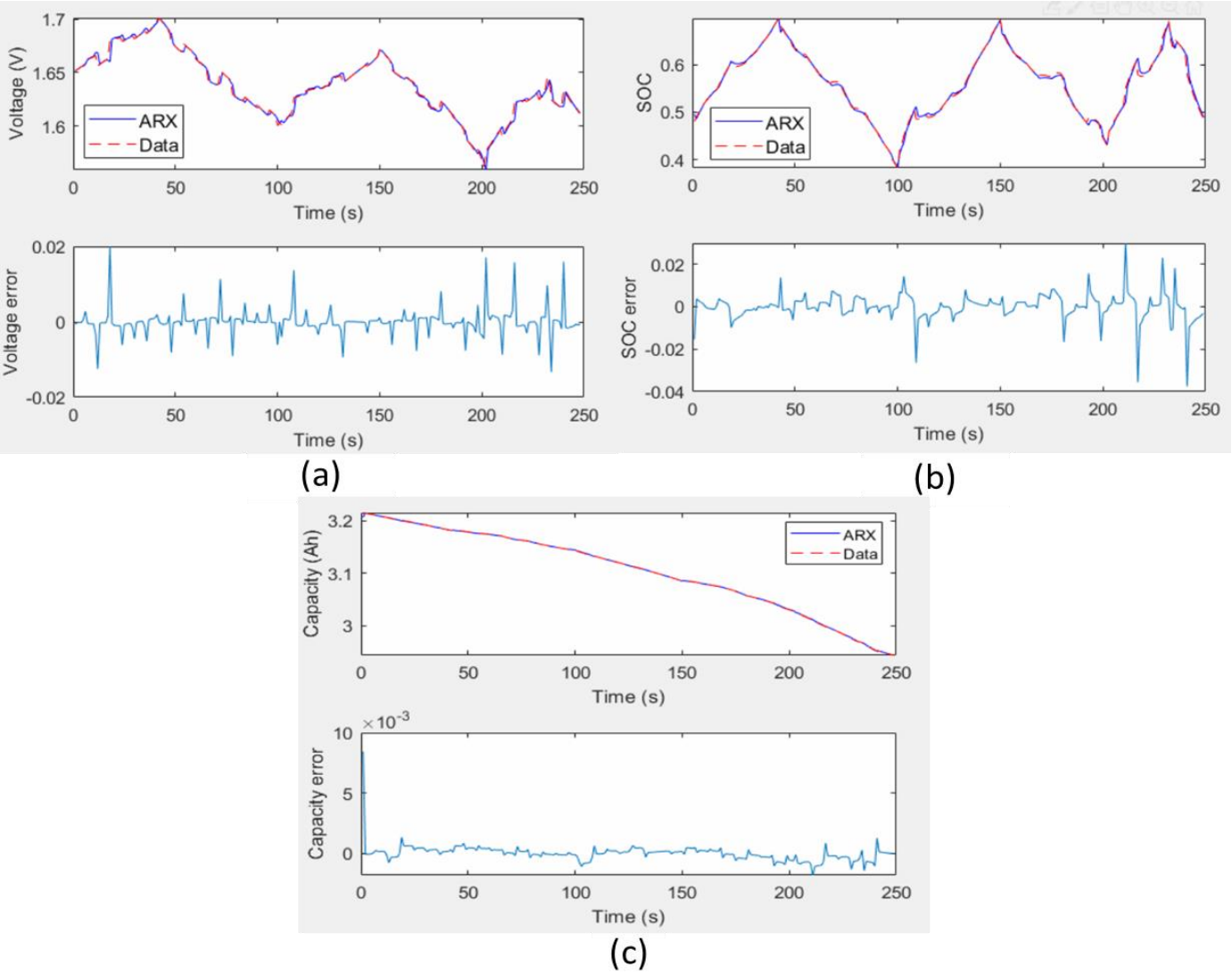

Figure 5.2. Comparison of the modeling results for the ARX model with the full order 2D model for (a) voltage, (b) SOC and (c) capacity

The comparison of two models is shown in Figure 6.2. It can be seen that the modeling results are in good agreement with the data developed from the validated 2D model. The error between two models is between ± 0.02 V for voltage as shown in Figure 6.2.(a) and for SOC the error is between

0.02 to −0.04, whereas the error for capacity is ~0.005 Ah. The error obtained in three cases is in an acceptable range.

5.4.3. Kalman filter modeling validation

For co-estimating SOC and capacity, a set of random input are simulated under cyclic charging /discharging. The developed Kalman filter model is ~25 times faster compared to the real-time model.

5.4.3.1. Voltage

Figure 6.3.(a) shows the true voltage, measured noisy voltage profile, and the estimates from Kalman filter. It is assumed that the cell voltage measurement has a standard deviation of 10 mV [173]. For both capacity and SOC, the process noise is assumed to be 1%. Figure 6.3.(b) shows the error in the Kalman filter estimate, which is found to be very small. The estimates are found to be satisfactory.

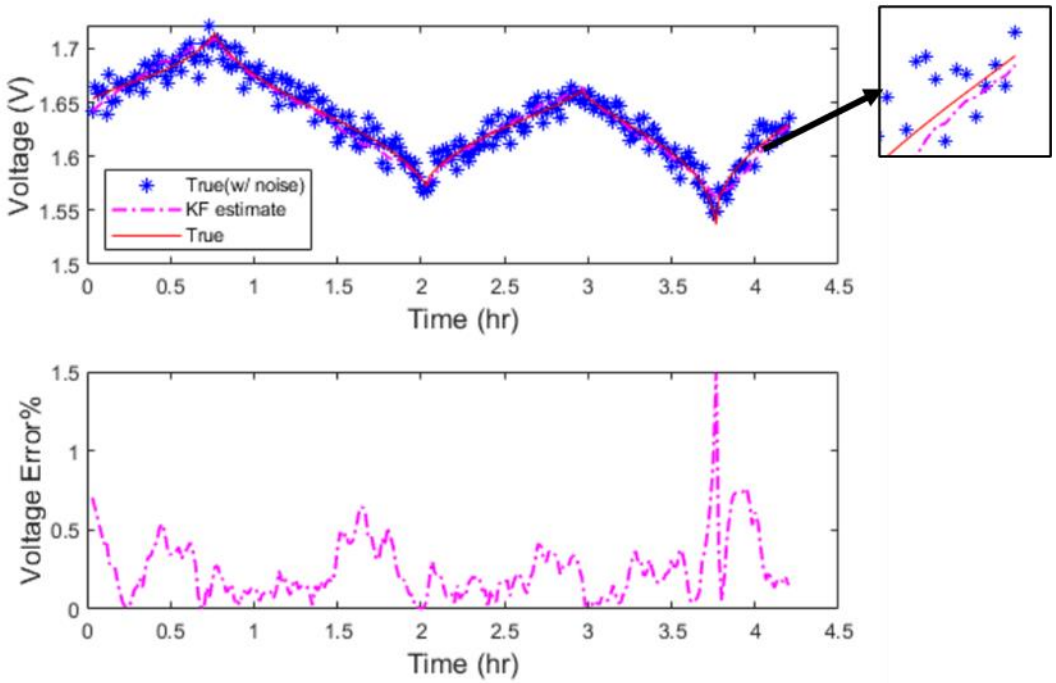

Figure 5.3. (a) Voltage profile showing comparison between true model, true model with noise and the Kalman filter model. (b) Voltage error % for Kalman filter with true model

5.4.3.2. SOC and Capacity

Co-estimation of capacity and SOC is shown in Figure 6.4 (a) and (c). It can be seen from the figure that the estimated initial value converges very fast with the true value. After that the predicted value tracks the true value almost with high accuracy with an average estimation error of 4.2% for SOC and 0.5% for capacity as shown in Figure 6.4 (b) and (d). This shows the robustness and validation of the proposed Kalman filter model when compared to the high fidelity 2D model.

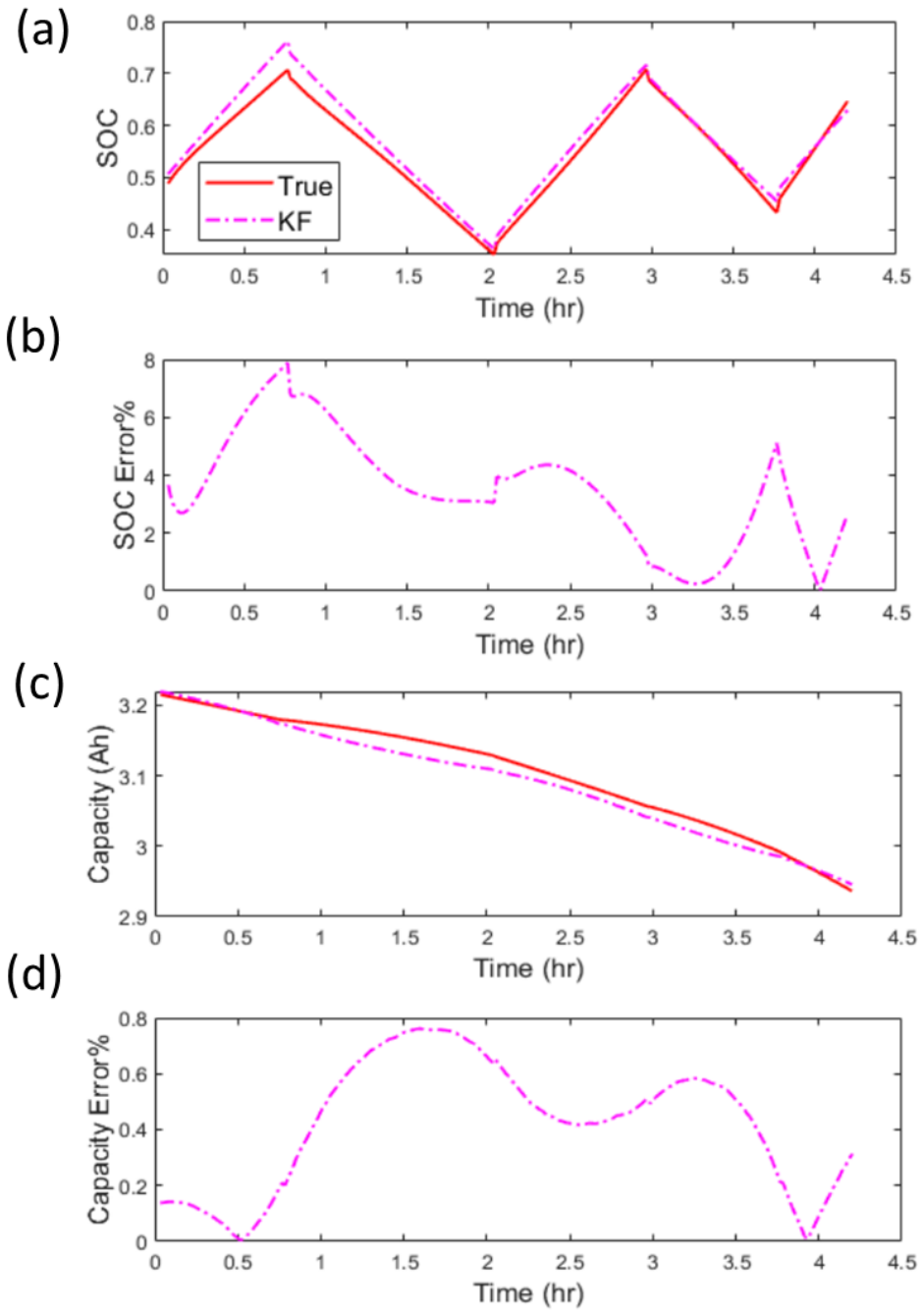

Figure 5.4. Comparison of proposed Kalman filter model with the true 2D model for (a) SOC and (c) Capacity for variable inputs and model error % for Kalman filter with true model for (b) SOC and (d) Capacity

5.5. Conclusions

For simultaneous estimation of SOC and capacity fade, a Kalman filter based method is developed. Output data generated by PRBS of current density and electrolyte flowrate were generated by perturbing a 2D validated ACM model that was presented in the last chapter. A linear ARX model is considered and linear least squares estimate of model parameters are obtained. The reduced order model is found to agree well with the detailed model in the range that was studied. The linear model is used in a Kalman filter. The performance of the estimator is evaluated by simulating some arbitrary charging/discharging scenario. Using the noisy voltage signal, the estimator could satisfactorily estimate the SOC and capacity fading. The filter can be executed ~25 times faster than real time and therefore can be used in real-time condition monitoring application. Overall, this approach shows that even though the SOC and capacity fading are complex phenomena for VRFB, and they cannot be directly measured, the proposed estimator-based approach can be successfully used for monitoring the temporal change.

Chapter 6. Development of a Dynamic Model of Pumped Hydro Storage System

6.1. Literature Review

To store energy in bulk, pumped hydro-electric storage system (PHS) is a promising option. This system helps to address the high electricity production cost and the increasing demand [8][175] [176][177]. Moreover, PHS have an efficiency in the range of 70% to 80% [103][104][180] with some having an efficiency as high as 87% [181].

PHS stores and generates energy by transporting water between two reservoirs at different elevations. Energy is stored in the form of gravitational potential energy and converted to electrical energy during demand. During off-peak period, water is pumped from lower reservoir to the higher reservoir (charging), by spinning of the turbines in backward direction, storing the electric energy in the form of hydraulic potential energy. During peak period, water moves down which causes the turbines to spin forward (discharge) generating mechanical energy. The turbine then activates the generator that converts mechanical energy to electricity, satisfying the demand. A PHS system can be classified as either an open-loop system or a closed-loop system depending on the type of reservoirs used [182]. In an open-loop system, at least one reservoir uses a free-flowing water source to a natural body of water. In contrast, in a closed-loop system, either reservoirs do not use/ are connected to, a free-flowing water source. This minimizes the influence on the environment and does not obstruct the natural water flow. PHS systems offer several advantages such as, flexible start/stop and fast response speed, ability to track and adapt to load changes, can modulate the frequency [12][108][109]. However, the relatively low energy density of PHS systems requires either a very large body of water or a large variation in height.

PHS is the only proven largescale (>100 MW (~4100MW)) energy storage technology [185]. There has been an increased trend of installations and operation of these schemes [186]. Technically feasible, commercially and socially acceptable site selection is a critical issue for PHS. Besides, the suitable locations to construct PHS are becoming scarce [187]. Connolly [188] developed a computer-based program to scan and identify the feasible locations for PHS.

The first PHS appeared in 1890s, contained separate pump impellers and turbine generators. In 1950s, a single reversible pump-turbine has become available for pumped hydroelectric storage [189]. From 1960's to 1980's there was a significant development of PHS systems, mainly due to the deployment of nuclear power plants [186]. However, by 1990's the increasing difficulty to identify suitable locations along with the reduced growth of nuclear plants limited the development of PHS. But, in recent years there has been an increasing interest towards PHS as a mature and large-scale energy storage technology to support green energy production. In this context, research is being done on different types of PHS technologies to improve the overall pump-turbine efficiency over a wide range of operating conditions.

Many studies have reported the dynamics of the PHS model [115]–[119]. These models considered water conduit as both rigid and elastic. These models use reversible turbine/pump head-flow. The effect of using multiple penstocks (which combines the hydraulic dynamics of multiple pump/turbine units) has been modeled [118][119]. Hitachi [195] designed a model to control the power level in both pumping and generation modes with a faster response time.

To date many efforts have been made to model PHS [191], [196]–[198]. However, these models are based on ordinary differential equations (using Laplace transform PDE's are converted to ODE's), which may not be sufficient to study the transients. The main reason is the coefficients of the transfer function, obtained from ODE's are not valid in the millisecond time periods. A coupled partial differential equations model has been used for a co-simulation in a real-time environment [199]. However, there is no model in literature considering the partial differential algebraic equations (PDAE) to design the complete model of PHS.

In this chapter, a PDAE-based dynamic model of a PHS system will be developed in Aspen Custom Modeler V.8.4. The model will be used to study transient performance of the PHSs under rapid load-following operation.

6.2. Model Development

As mentioned in section 4.1, pumped hydro storage system has two reservoirs located at different elevations. During discharging (peak period), the water flows down from upper reservoir, through the turbine. This causes the turbine to rotate in forward direction, generating mechanical energy and activating the generators to convert mechanical energy to electricity. During charging (off-

peak period), water from the lower reservoir is pumped back to higher reservoir by spinning turbine in backward direction. This stores the electrical energy in the form of hydraulic potential energy.

Two basic types of PHS are: fixed speed conventional pumped hydro system (C-PHS) and adjustable speed pumped hydro storage (AS-PHS). C-PHS is the traditional technology which utilizes a synchronous electric machine, which allows the unit to operate in both pumping and generating modes by changing the rotational direction of the motor. However, during pumping mode, single speed units are unable to provide frequency regulation. AS-PHS uses a conventional synchronous generator or doubly fed induction machine (DFIM) based on the net operating power. AS-PHS has the advantage to vary the pump and turbine rotation speed for more efficient overall operation and better integration with the power grid. The frequency of the rotor voltage and current can be adjusted to control the speed of the rotor. However, these two models can't operate simultaneously in pumping and generating mode. A new PHS being developed is the ternary PHS (T-PHS), which can operate simultaneously in HSC mode. A T-PHS unit is typically divided into three parts: a synchronous machine, an exciter to regulate the reactive power or voltage, and a governor to regulate the hydropower or indirectly regulate the electrical power. Despite the advantages, T-PHS incurs high investment costs, high maintenance due to electromechanical complexity, lower efficiency in HSC mode and low stability of the rotating shaft due to low pump submergence. Each model has its own advantages and disadvantages. In this work a reversible pump turbine unit is modeled to develop a fully working pumped storage system, which is made to follow the load requirements using PID controller for pump and turbine.

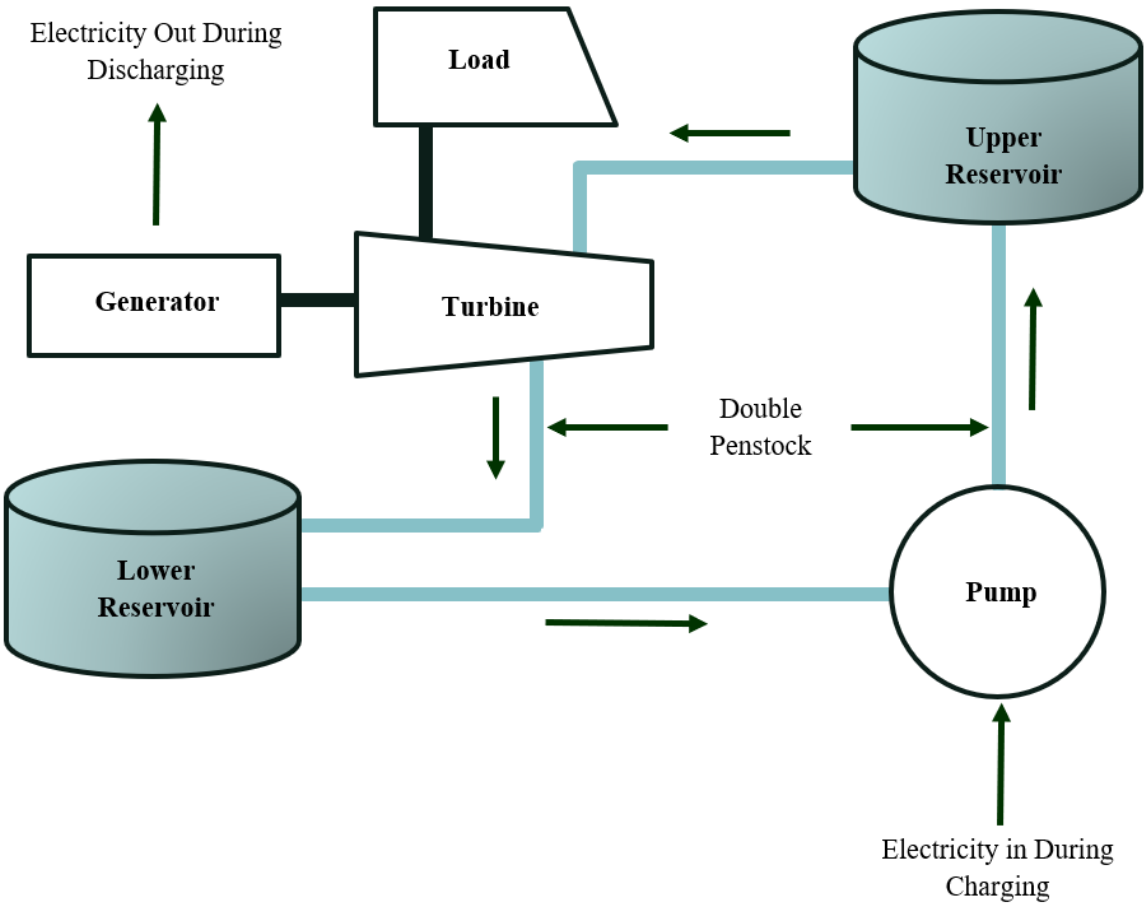

Figure 6.1. Principle of Pumped Storage Hydro Power Plant

A system of PDEs for pipeline system and pump/turbine are modeled in ACM V.8.4. PID controllers are used to control the power produced/consumed. This is done by manipulating the guide vane opening, which controls the flowrate. Signal selector is used to select the respective controller depending on the mode of operation.

6.2.1. Modelling Equations

Pipeline system (Basic hydraulic equations):

Equation of Motion:

Applying the Newton's second law for a fluid element inside a tube gives a differential motion equation for a transient flow:

$$g\frac{\partial H}{\partial x} + V\frac{\partial V}{\partial x} + \frac{\partial V}{\partial t} + \frac{fV|V|}{2D} = 0 \tag{6.1}$$

where V is the velocity (m/s), f is the coefficient of friction, H is the pressure head (m) and D is the pipe diameter (m).

Continuity Equation:

The continuity equation is given by:

$$V\frac{\partial H}{\partial x} + \frac{\partial H}{\partial t} - VSin\alpha + \frac{a^2}{g}\frac{\partial V}{\partial x} = 0 \tag{6.2}$$

where α is the pipe inclination angle. In both Equations (6.1) and (6.2), $H(x,t)$ and $V(x,t)$ are dependent variables and represent the head and average velocity, and the variables 'x' (displacement) and 't' (time) are independent variables.

Using the hydraulic transients, the convective terms $V\frac{\partial V}{\partial x}$ and $V\frac{\partial H}{\partial x}$ and the tube inclination effect can be neglected. By assuming uniform pressure and velocity distributions in the cross section, the one-dimensional momentum and continuity balances for an elementary pipe filled with water of length 'dx', cross-sectional area 'A' and wave speed 'a' yield the following set of hyperbolic partial differential equations:

$$\begin{cases} \frac{\partial H}{\partial t} + \frac{a^2}{gA}\frac{\partial Q}{\partial x} = 0 \\ \frac{\partial H}{\partial x} + \frac{1}{gA}\frac{\partial Q}{\partial t} + \frac{\lambda|Q|}{2gDA^2}Q = 0 \end{cases} \tag{6.3}$$

where Q is the flow in m^3/s.

The hydraulic resistance R, the hydraulic inductance L, and the hydraulic capacitance C, representing energy losses, inertia and storage effects are given by the following equations:

$$R = \frac{\lambda|Q|}{2gDA^2}dx \tag{6.4}$$

$$L = \frac{dx}{gA} \tag{6.5}$$

$$C = \frac{g\,A\,dx}{a^2} \tag{6.6}$$

where λ is the local loss coefficient.

Pump/Turbine:

Reaction turbines contain a runner, through which water passages and it is formed by curved vanes or blades. Rotation of the runner occurs as the water passes through the runner and over the curved surfaces. The rotational motion is transmitted by a shaft to a generator. Assuming a fully developed turbulent flow, the following one-dimensional model is considered.

Hydraulic Equation:

$$T_{wt}\frac{dq}{dt} = h - \frac{q|q|}{\kappa^2} - \sigma|\Omega^2 - 1| \tag{6.7}$$

Torque Equation:

$$T_a\frac{d\Omega}{dt} = |q|(\widetilde{m_s} - \varphi\Omega)\left(1 - \frac{\Delta h}{h}\right) - R_m\Omega^2 - \eta_g \tag{6.8}$$

, where T_{wt} and T_a are the time constants of water and rotational masses respectively in the turbine. $q = \frac{Q}{Q_n}, h = \frac{H}{H_n}, \Omega = \frac{\omega}{\omega_n}$, κ is the guide vane opening degree, $\widetilde{m_s}$ is the dimensionless start torque, R_m is the mechanical loss coefficient, σ and φ are the machine constants, η_g is the efficiency of the generator.

These Euler's equation describes the physics of a Francis turbine. However, the data on the loss factors for hydraulic and mechanical losses is limited. This creates a challenging situation to implement the losses.

Including a pump effect to the Equations (6.7) and (6.8), makes them applicable for reversible pump/turbine unit. Denoting the pumping effect by "P" the equations are written as:

Hydraulic Equation:

$$T_{wt}\frac{dq}{dt} = h - \frac{q|q|}{\kappa^2} - \sigma|\Omega^2 - 1| - \underbrace{r_p\Omega^2 + r_p\Omega q}_{\text{P}} \tag{6.9}$$

Torque Equation:

$$T_a\frac{d\Omega}{dt} = |q|\overbrace{\left(\widetilde{m_s} - \varphi\Omega + \gamma\Omega - r_p q\right)}^{\text{P}}\left(1 - \frac{\Delta h}{h}\right) - R_m\Omega^2 - \eta_g \tag{6.10}$$

r_p and γ are the pumping parameters, Δh is the dimensionless hydraulic loss.

Net torque is calculated as given:

$$T = \rho Q(t_s - r_2{}^2\omega) \tag{6.11}$$

Where t_s is the starting torque at $\omega = 0$.

6.3. Results and discussions

The design parameters of Roanoke Rapids Power Station are considered and tuned to work for a single reversible pump/turbine unit. More information about the dimensional parameters and nominal conditions is provided under results and discussion section in Appendix D.

6.3.1. Transient responses

Transient responses are generated for head, flowrate, and power. Figure 6.2 shows the transient response in head during pumping and generating modes. As expected, the head of water decreases in the upper reservoir during generation of power while the water height increases during pumping as the water is pumped back into the reservoir.

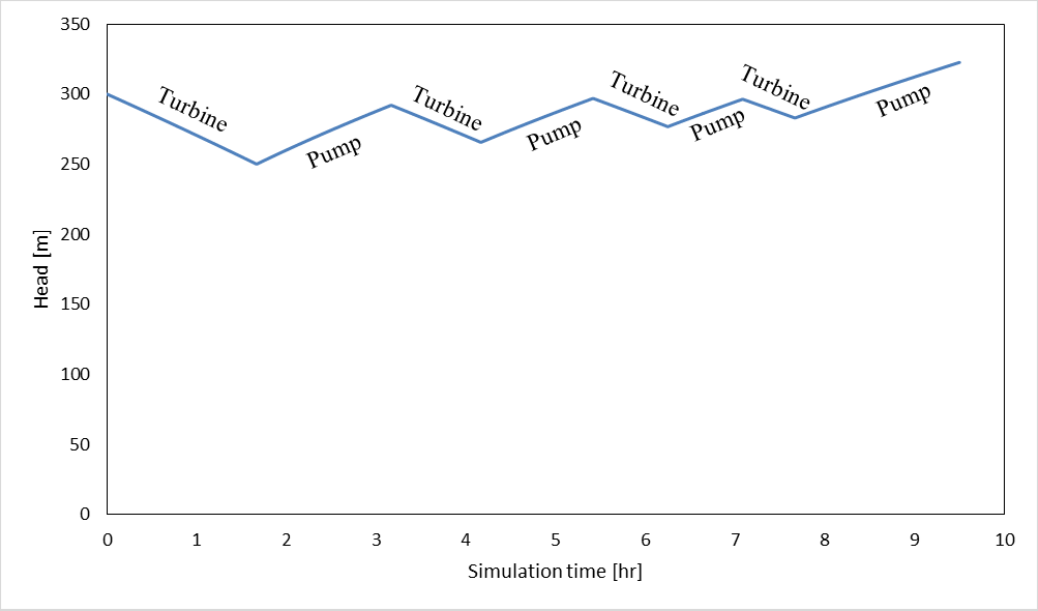

Figure 6.2. Transient response in head during pumping and generation modes

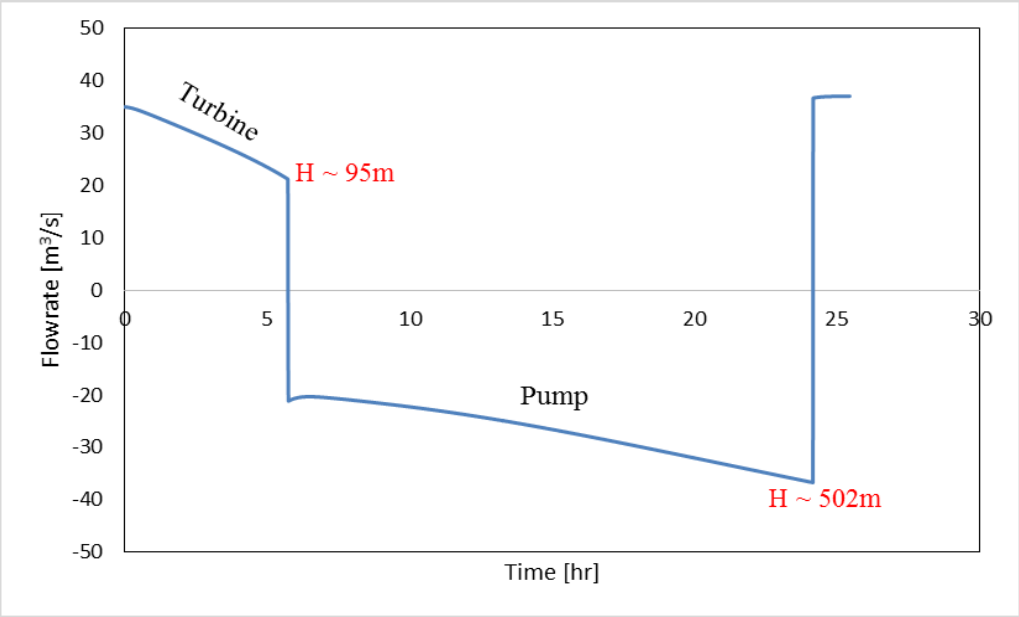

Figure 6.3. Transient response in flowrate during pumping and generation modes.

Similar to the head profile, the flowrate is observed to decrease along with the head during turbine mode and increase during pump mode of operation as shown in Figure 6.3. The change in the flowrate depends on the angle of the guide vane in Equation (6.9), which is manipulated for a desired power to be consumed or generated.

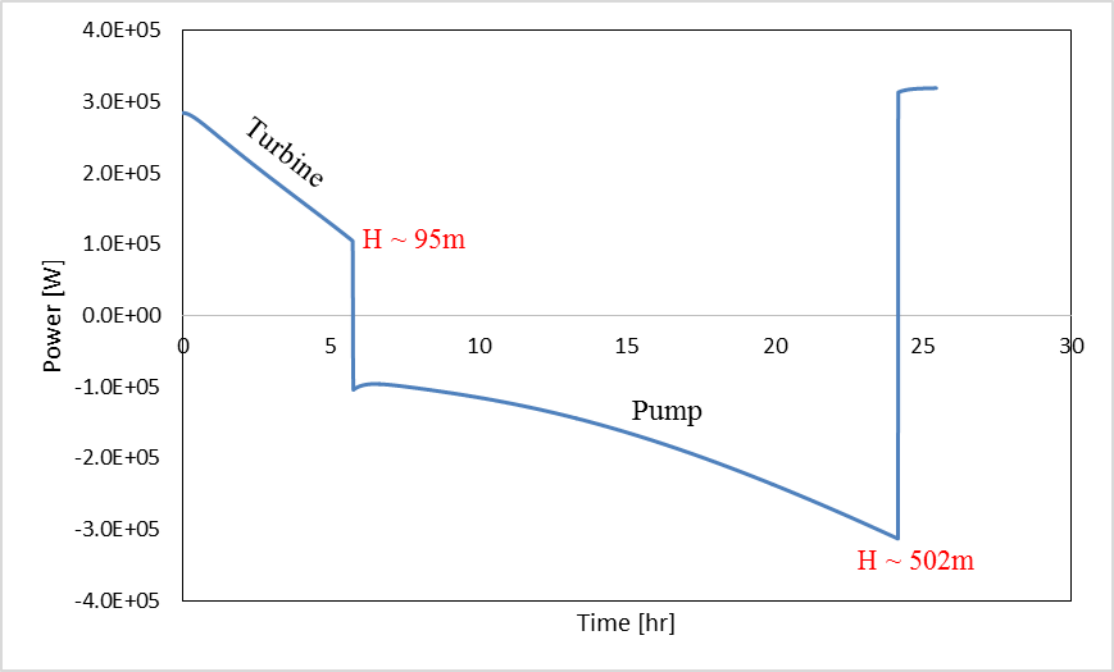

Figure 6.4. Power profile during pumping and generation modes.

The power is produced during turbine mode of operation and is consumed during pumping mode of operation. With time the power produced decreases while the power consumed increases as shown in Figure 6.4.

6.3.2. Load following profile

Using two PID controllers the amount of power produced and consumed is controlled respectively, by manipulating the guide vane opening angle of the turbine gate. Initially the difference between the profiles generated using PID controllers and without PID controllers was generated, which is discussed in results and discussion section in Appendix D. Then the PID controllers were tuned such that the system was able to follow the desired load requirements as shown in Figure 6.5.

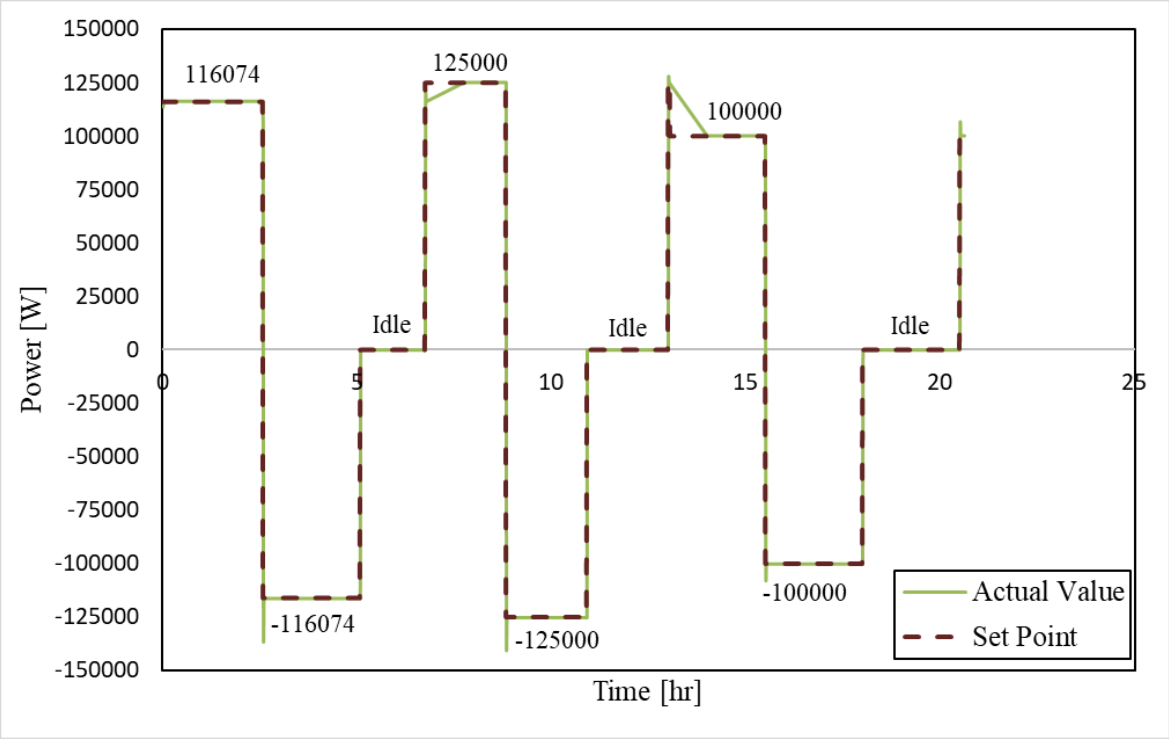

Figure 6.5. Load following power profile during generation and pumping modes with PID controllers

Figure 6.5 shows the load following power profile for model with PID controllers. Initially the power required was set to 116074 W. Later the set point for power was changed to 125000 W and 100000 W. The model was able to meet this required set point power. The generated model was able to follow the load requirements with an overall efficiency of ~97%.

Chapter 7. Final Remarks

In this work, grid-level energy storage systems modeling, and optimization under different operating conditions has been conducted. In addition, thermal management, reduced order modeling, parameter estimation, and Kalman filter modeling has been undertaken for estimating and increasing the efficiency of the storage systems. High-fidelity energy storage process models have been developed, using a multi-software platform that includes Aspen Custom Modeler and Microsoft Excel. Using these models, optimization and estimation processes have been performed in MATLAB to analyze the efficiency of the systems. The model processes have been validated with literature, where possible.

For sodium sulfur battery, the following tasks have been performed and conclusions have been made. A cell model was developed for sodium sulfur battery. Temperature dependent correlations were developed for thermo-physical parameters, by fitting the data available in the literature. A set of governing equations and boundary conditions were developed for each component of the cell. The developed model was validated with the data available in literature. The cell model was studied under different operating conditions to understand the transients and the sensitivity of the model. Temperature distribution across the cell was monitored to study the need for thermal management system. Reduced order model was proposed to decrease the computational efficiency and to design a battery model from the single cell model. Three different thermal management strategies have been proposed. Of the proposed thermal management strategies hybrid cooling was declared as a promising strategy for safe and efficient operation of sodium sulfur batteries.

For pumped hydro storage, a dynamic model considering hydraulic and mechanical concepts was developed. The transient responses were studied under different operating conditions for charging and discharging. A PID controller was implemented to follow the desired load trajectory, with ~98% efficiency.

For vanadium redox flow battery, following tasks have been performed and conclusions have been made. A 2D isothermal model considering three different capacity degradation mechanisms was developed. The model was validated at operating conditions same as the data available in the literature. Transient profiles were generated to understand the mechanisms and the electro-chemistry within the cell. Especially the concentration distribution and the effects on cell voltage,

SOC and capacity were studied. Impact of tank volume, current density and electrolyte flowrate were analyzed to understand the sensitivity of the model. Capacity fade as a result of running the model over several cycles was estimated. To co-estimate the capacity and SOC in real-time, a Kalman filter based condition monitoring approach is developed. The approach can be executed faster than real time yet can provide very accurate estimate of SOC and capacity.

Reduced order models were developed for NaS and VRFB models as a part of techno-economic assessments (TEA) project for an integrated fossil fuel power plant and storage system. More information regarding this can be found in Appendix E.

Chapter 8. Future Work

In this research work grid-level energy storage models were developed and optimized. The model presented here for NaS cell can be readily extended to room temperature NaS cells, especially for studying the deviation in spatial and temporal temperature profile of those cells from the room temperature under charging/discharging conditions and how the deviation affects the cell efficiency and performance. The model presented can also be extended to Li-S cells. In Li-S cells, the anode and the electrolytes are quite different than the Na-S cells. Even though there are certain differences between the cathodes of these two types of cells including the differences in the specific energy density, lowest state of sulfur that the cell can be discharged into, volumetric change during reaction, degradation mechanisms, to name a few, cathode reactions and electronic and ionic transport mechanisms are similar. Therefore, the model of the sulfur electrode presented here can be a very good starting point for modeling the cathode of the Li-S cells.

In developing the thermal management strategies certain quantities like specific heat, heat of fusion etc., for PCM were considered constant. Their dependence on temperature can be considered to understand the effect of surrounding temperature on PCM. Further, though the model is efficient with time the performance degrades. Therefore, an estimation framework can be developed to predict the lifetime of sodium sulfur battery system.

For vanadium redox flow batteries, two different models to estimate the charging and discharging case separately can be developed to minimize the error further. The Kalman filter formulation needs to be updated appropriately if model switching is considered. Considering non-linear estimator-based approaches can be helpful in increasing the accuracy further.

Performance and operation of the power conditioning is an important aspect to consider. Since this research mainly focused on process systems engineering aspect, the power condition system is considered to be the boundary and is not accounted for.

Furthermore, all the reduced order models developed in this work can be used in scheduling optimization such as dispatch can be performed to co-simulate and integrate different energy suppliers (source + storage) to satisfy the demand without curtailment of renewables.

Appendix A: Parameter Correlations for sodium sulfur cell developed by fitting to experimental data in the open literature.

A.1. Sulfur Electrode

The thermal conductivity of the sodium polysulfide melt in the sulfur electrode is assumed to be dominated by the sulfur present in the melt. With this assumption, the thermal conductivity of the melt takes the form as shown in figure A.1. This relation for thermal conductivity, as a function of temperature, comes from the data given in [200] and is shown below:

$$\lambda_{(S)} = 0.4813 - 1.8648 \times 10^{-3} T_{(S)} + 2.4844 T_{(S)}^2 \qquad \text{(A1)}$$

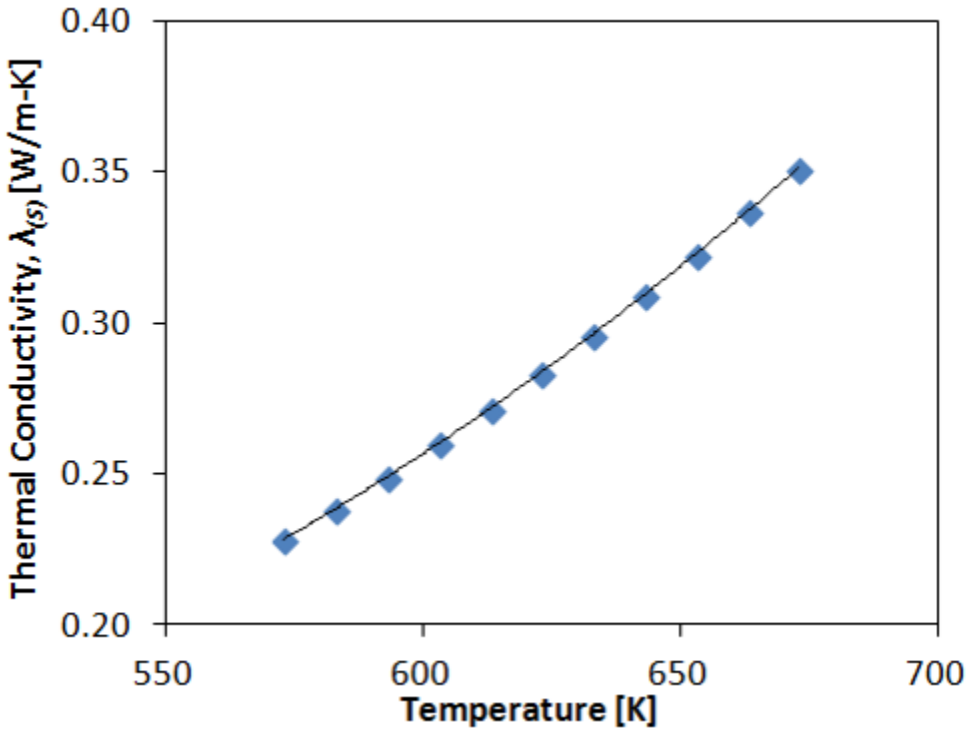

Figure A.1. Thermal conductivity of liquid sulfur as a function of temperature [51]**.**

The density of the melt is based on the experimental data for sodium polysulfides obtained from [30]. Since the operating temperature remains 300-400 °C, the melt density is assumed to be constant, with a value of 1880 kg/m^3.

The specific heat of the sodium polysulfide melt is based on the data for polysulfides obtained from [30]. While the specific heat is a function of the mole fraction of sulfur in the melt, it is assumed to be constant since there is less than 1% variation in the specific heat over the entire operating range. The value of specific heat considered in the model is 1315 J/kgK.

The entropy term, which accounts for the reaction in the sulfur electrode, is a function of the SOD as shown in Figure A.2 obtained based on the literature data [42].

$$T\frac{dE}{dT} = -15.536SOD^5 + 32.652SOD^4 - 22.969SOD^3 + 6.0576SOD^2 - 0.5629SOD - 0.0362 \quad \text{(A2)}$$

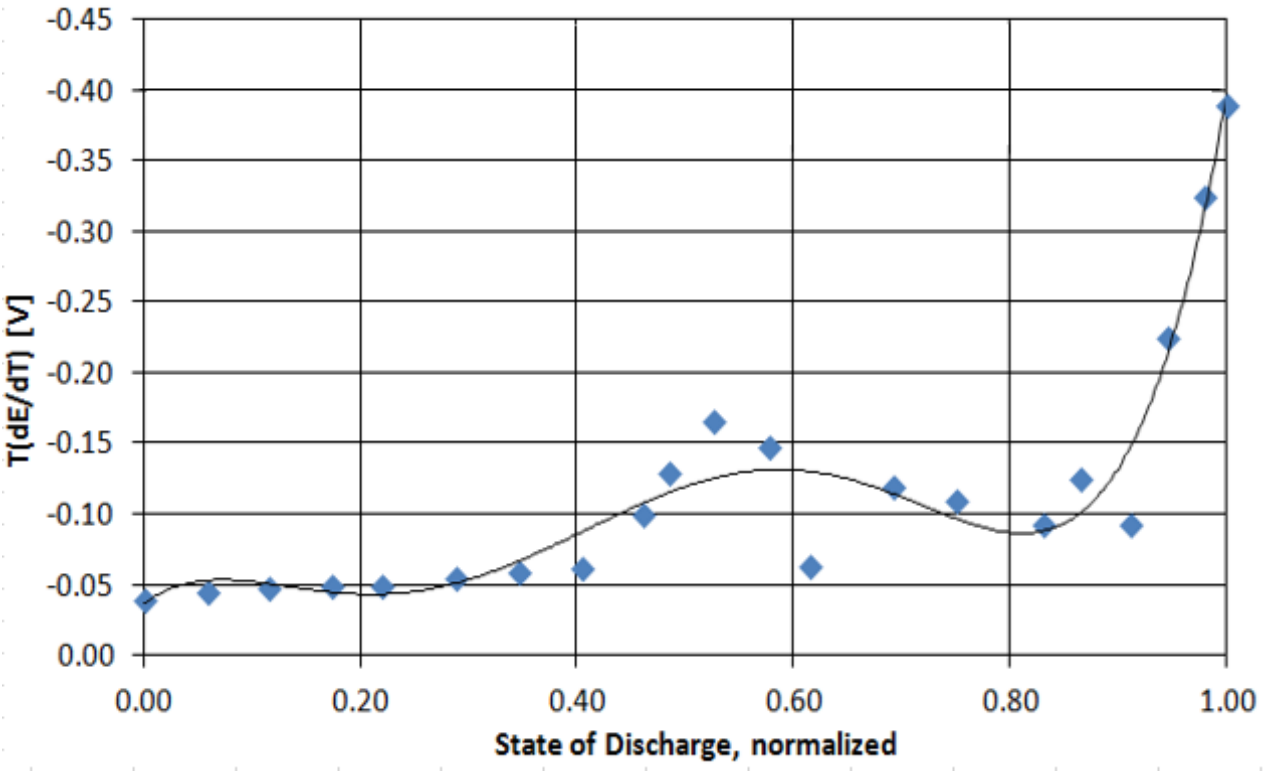

Figure A.2. The entropy term correlation for the sodium sulfur cell [42].

The SOD is a function of the melt composition. Based on the data in the Appendix of [30] for the sodium polysulfide melt, the equation for SOD as a function of melt composition takes the following form:

$$\mathrm{SOD} = \begin{cases} -343.55\mathrm{M} + 304.82, & \text{single phase polysulfide} \\ -202.43\mathrm{M} + 202.23, & \text{two phase sulfur/polysulfide} \end{cases} \quad \text{(A3)}$$

The correlation [51] for the overpotential coefficients with temperature (Table 2.1) is shown below and their profiles are shown in Figure A.3.

$$\alpha_1 = (-8.1667 \times 10^{-5})\left(T_{(S)}\right) + 2.5087 \quad \text{(A4)}$$

$$\beta_1 = (-7.350 \times 10^{-4})\left(T_{(S)}\right) - 1.5600 \quad \text{(A5)}$$

$$\beta_3 = (3.0783 \times 10^{-3})\left(T_{(S)}\right) + 0.0472 \quad \text{(A6)}$$

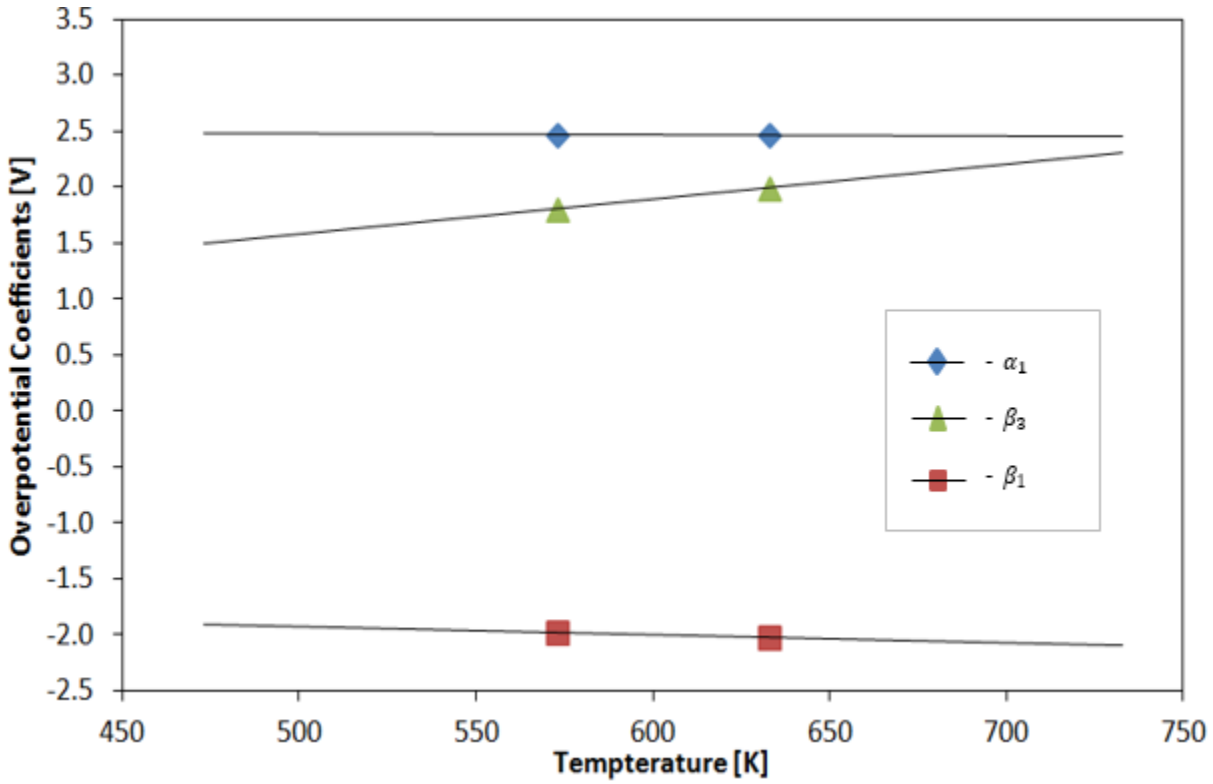

Figure A.3. Overpotential coefficient relations based on experimental data [51].

A.2. Beta”-Alumina Electrolyte

The bulk theoretical density of the electrolyte is assumed to be 3220 kg /m^3 [55]. The density of the solid electrolyte is calculated using the following equation [30]:

$$\rho_{(el)} = 3220 \exp\left(-3\alpha_L\left(T_{(el)} - 25\right)\right) \quad \text{(A7)}$$

, where α_L denotes coefficient of linear thermal expansion for beta”-alumina.

The porosity of the solid electrolyte is approximated using the following relation,

$$p_{(el)} = (3220 - \rho_{(el)})/3220 \tag{A8}$$

where 3220 kg/m^3 is the theoretical density of the electrolyte and $\rho_{(el)}$ is the actual density of the electrolyte. The actual density changes with temperature, therefore making the porosity a function of temperature as well.

The ionic conductivity and diffusion coefficient of sodium ions in the beta"-alumina electrolyte take Arrhenius forms [58] (as in Table 2.2):

$$\sigma_{i(el)} = (\sigma_{0(el)}/T_{(el)})exp\left[-H/(RT_{(el)})\right] \tag{A9}$$

$$D_{(el)} = D_0 exp\left[-H/(RT_{(el)})\right] \tag{A10}$$

A.3. Sodium Electrode

The specific heat capacity for the liquid sodium and stainless-steel wick in the sodium electrode are shown in Figure A.4. **Specific heat of liquid sodium and stainless-steel wick based on the experimental data** [30]**.**, based on the data obtained from the Appendix of [30].

$$c_{p,ss} = -4.591 \times 10^{-4} {T_{(Na)}}^2 + 0.4813 T_{(Na)} + 444.99 \tag{A11}$$

$$c_{p,Na} = 1437.08 - 0.58063 T_{(Na)} + 4.624 \times 10^{-4} {T_{(Na)}}^2 \tag{A12}$$

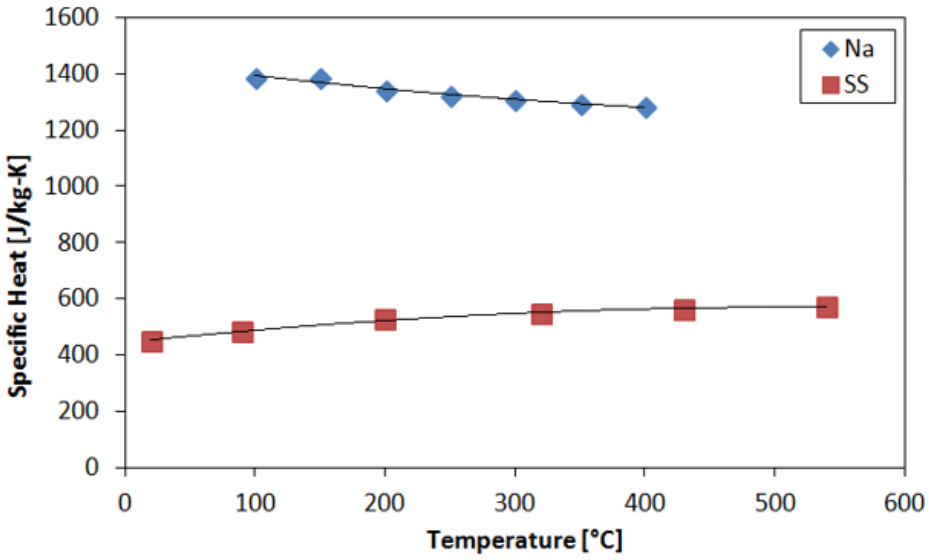

Figure A.4. Specific heat of liquid sodium and stainless-steel wick based on the experimental data [30].

Appendix B: Heat Transfer coefficients, Effect of air velocity and Phase change material for thermal management of sodium sulfur battery

B.1. Heat Transfer

Heat transfer from cell to the surrounding air or PCM varies with velocity and temperature, respectively. The calculation of heat transfer coefficient between cell boundary, PCM and flowing air is shown in Table B.1.

Table B.1. Correlations to calculate heat transfer coefficient

Expression	*Units*	*Reference/Comments*
$h = \frac{Nu * \lambda}{r_o}$	W/m^2K	Heat transfer coefficient
Air:		
$Nu_{air} = 0.683Re^{0.446}Pr^{1/3}$	dimensionless	Hilpert correlation for cylinders [201]
$Re = \frac{r_o v_{air} \rho_{air}}{\mu_{air}}$	dimensionless	Reynolds number
$\mathrm{Pr} = \frac{C_{p,air} * \mu_{air}}{\lambda_{air}}$	dimensionless	Prandtl number
Phase Change Material:		
$Nu_{pcm} = 0.393Ra^{0.267}$	dimensionless	Nusselt number [202]
$Ra = \frac{gb}{vis_{pcm}\alpha}(T_{wall} - T_{PCM})L^3$	dimensionless	Rayleigh number
$\alpha = \frac{\lambda_{PCM}}{\rho_{PCM} C_{P,PCM}}$	m^2/s	Thermal Diffusivity

B.2. Effect of air velocity

As air velocity changes, the variability in temperature during charging and discharging also changes. Figure B.1 shows the difference between maximum cell temperature and air temperature profile at different air velocities. For these studies, the air velocity was kept constant during the

entire charging/discharging cycle. It is observed that when the air velocity is 5 m/s, ΔT is almost 1.3 times less than for the air velocity of 3 m/s and is nearly 2 times less compared to the air velocity of 1.5 m/s. Figure B.1 also shows the standard deviation of heat rejection at different velocities. It is observed that as the velocity increases the variability in the heat rejection rate decreases as would be expected based on the results from Figure B.1.

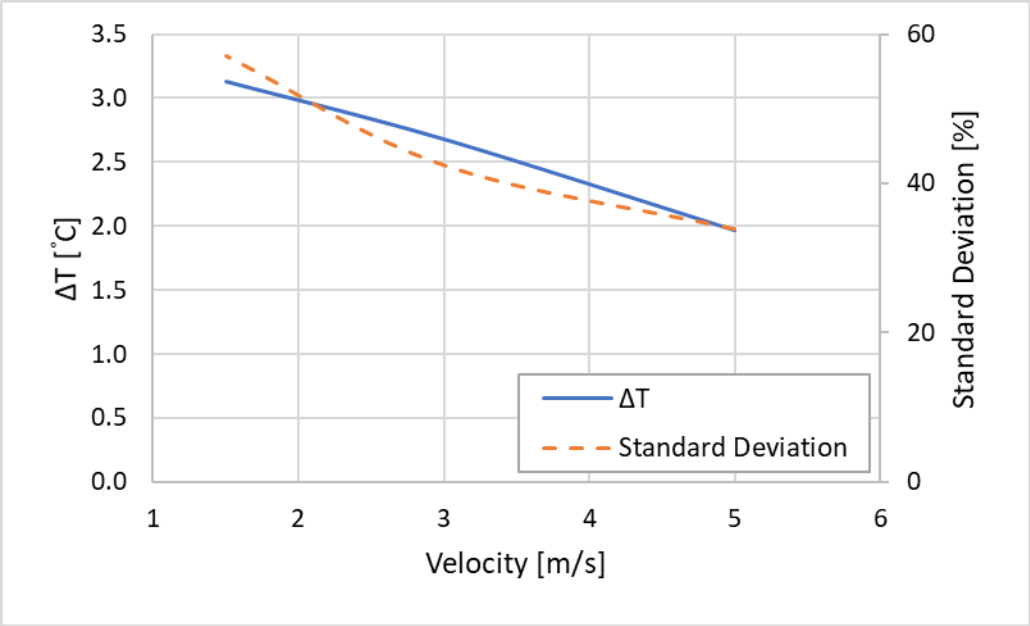

Figure B.1. Difference between maximum cell temperature and air temperature profile and standard deviation of heat rejection profile during continuous charging and discharging at different velocities for ±22 A current for an air inlet temperature of 335 ˚C

Figure B.2 shows the fractional fan power requirement for different air velocities. As the velocity of air increases the fractional power requirement also increases which can incur additional capital costs for the additional power. It was observed that the fractional fan power required for an air velocity of 5 m/s is almost 4.6 times more than for an air velocity of 3 m/s and is nearly 37 times more than for an air velocity of 1.5 m/s. This additional power requirement for air velocity of 5 m/s incurs additional capital cost.

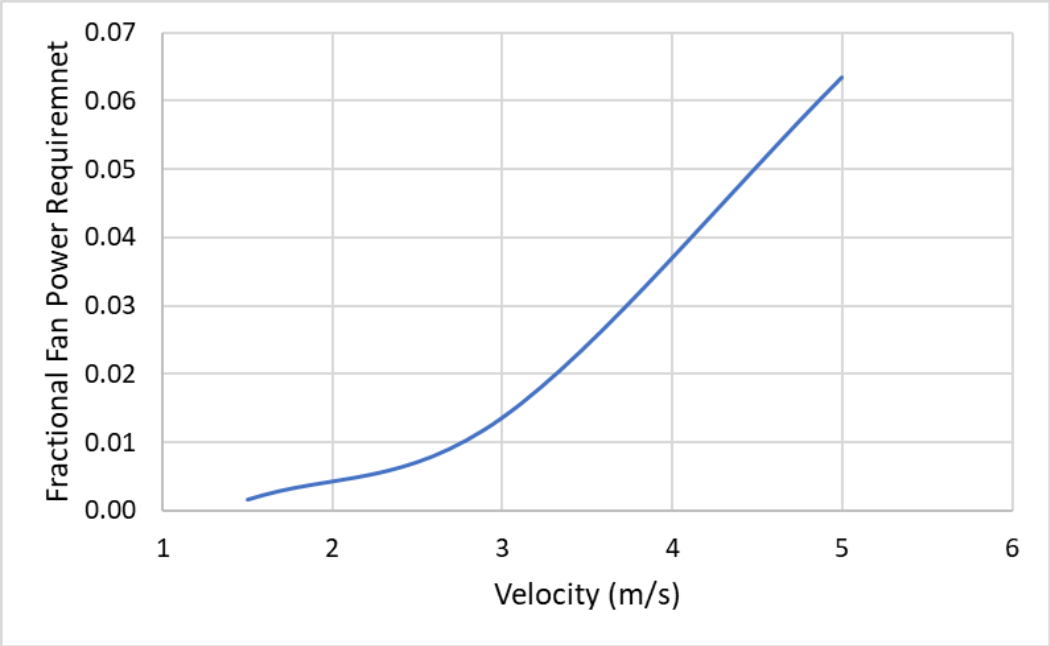

Figure B.2. Fractional fan power requirement profile at different air velocities for 22 A current for an air inlet temperature of 335 ˚C for a single battery module of 320 cells.

B.3. Phase Change Material

Phase change materials (PCM) are also known as latent heat storage materials. They release or absorb energy as phase of the material transitions to deliver required heating or cooling.

In this work, potassium nitrate, KNO_3 [80] is selected as a suitable PCM for sodium sulfur battery, because of its suitable melting point and high heat of fusion. Properties of KNO_3 relevant for application in thermal management of NaS batteries are shown in Table B.2.

Table B.2. Properties of PCM (KNO_3)

Property	Value	Units	Reference
Melting Point	337	˚C	[80]
Thermal Conductivity	$0.6275 - 3.5 \times 10^{-4}T$	W/m k	[203]
Kinematic viscosity	$(7.73 \times 10^{-2}) \times \frac{exp\left(\frac{18468.48}{8.314 \times T_{PCM}}\right)}{\rho_{pcm}}$	m^2/sec	[204]
Specific heat	940.2199	J/kg K	
Heat of fusion	116×10^3	J/kg	
Fractional increase in volume upon melting	0.033	dimensionless	[204]

Appendix C: Transport and Kinetic Parameters for VRFB modeling

C.1. Transport Parameters

Transport properties used in developing the VRFB 2-D model are given in Table C.1.

Table C.1. Transport parameters

Parameter	*Value*	*Units*	*Reference/Comments*
Diffusivity of V^{+2} in electrode (D_{II})	2.4×10^{-10}	m^2/s	[205]
Diffusivity of V^{+3} in electrode (D_{III})	2.4×10^{-10}	m^2/s	[205]
Diffusivity of V^{+4} in electrode (D_{IV})	3.9×10^{-10}	m^2/s	[205]
Diffusivity of V^{+5} in electrode (D_V)	3.9×10^{-10}	m^2/s	[205]
Diffusivity of H^+ in electrode (D_{H^+})	9.31×10^{-9}	m^2/s	[163]
Diffusivity of HSO_4^- in electrode ($D_{HSO_4^-}$)	1.33×10^{-9}	m^2/s	[163]
Diffusivity of SO_4^{-2} in electrode ($D_{SO_4^{-2}}$)	1.065×10^{-9}	m^2/s	[163]
Diffusivity of H_2O in electrode (D_w)	7.35×10^{-5}	m^2/s	[162]
Dissociation coefficient of HSO_4^- (k_d)	1×10^4	$mol/(m^3.s)$	[161]
Degree of dissociation of HSO_4^- (β)	0.1	N/A	[14]

(‘contd.)

Diffusivity of V^{+2} in membrane (D_{II}^{m})	3.39×10^{-12}	m^2/s	[143]
Diffusivity of V^{+3} in membrane (D_{III}^{m})	1.87×10^{-12}	m^2/s	[143]
Diffusivity of V^{+4} in membrane (D_{IV}^{m})	2.84×10^{-12}	m^2/s	[143]
Diffusivity of V^{+5} in membrane (D_{V}^{m})	2.32×10^{-12}	m^2/s	[143]
Diffusivity of H^{+} in membrane ($D_{H^{+}}^{m}$)	3.5×10^{-10}	m^2/s	[161]
Diffusivity of HSO_4^{-} in membrane ($D_{HSO_4^{-}}^{m}$)	4×10^{-11}	m^2/s	[161]
Diffusivity of H_2O in membrane (D_{w}^{m})	5.75×10^{-10}	m^2/s	[206]
Effective conductivity of electrode (σ_f)	164.4	S/m	[15]

C.2. Kinetic Parameters

The kinetic parameters [14], [207] used in developing the VRFB 2-D model are given in Table C.2.

Table C.2. Kinetic parameters [14], [207]

Parameter	Value	Units
Charge transfer coefficient for oxidation in negative electrode (α_{-}^{o})	0.3144	N/A
Charge transfer coefficient for reduction in negative electrode (α_{-}^{r})	0.2588	N/A

(‘contd.)

Charge transfer coefficient for oxidation in positive electrode (α_+^o)	0.131	N/A
Charge transfer coefficient for reduction in positive electrode (α_+^r)	0.1353	N/A
Reaction rate constant for oxidation in negative electrode (k_-^o)	5.47×10^{-7}	m/s
Reaction rate constant for reduction in negative electrode (k_-^r)	8.38×10^{-7}	m/s
Reaction rate constant for oxidation in positive electrode (k_+^o)	3.12×10^{-7}	m/s
Reaction rate constant for reduction in positive electrode (k_+^r)	2.79×10^{-7}	m/s
Standard equilibrium potential for negative electrode ($E_{0,-}^*$)	-0.225	V
Standard equilibrium potential for positive electrode ($E_{0,+}^*$)	1.004	V

Appendix D: Design parameters and additional results for pumped hydro-electric storage system

D.1. Design Parameters

The design parameters are taken from the Roanoke Rapids Power Station and are tuned to work for a single reversible pump/turbine unit. The dimensions and nominal conditions are mentioned in Table D.1 and Table D.2. Using these results are generated for a PHS with reversible pump/turbine system. Table D.3 shows the sign convention used in generating the results.

Table D.1. Main dimensions of the model runner:

$D_1 = 630\ mm$	$\alpha_{1,R} = 10^0$
$D_2 = 349\ mm$	$\beta_1 = 12^0$
$B = 24 \times 10^4\ mm$	$\beta_2 = 12.8^0$

Table D.2. Nominal Conditions of the turbine/pump model are considered as follows:

$H_n = 135\ m$	$H_{max} = 180\ m$
$Q_n = 10\ m^3/s$	$T_n = 4.05 \times 10^6\ Nm$
$\omega_n = 7.5\ /s$	$J = 542000\ kgm^2$

Table D.3. The following sign convention was used in developing the results:

Turbine mode	Pump mode
$Q > 0$	$Q < 0$
$\omega > 0$	$\omega < 0$

D.2. Additional results and discussions

To make this model follow the desired load requirements two PID controllers are attached, one for pump and one for turbine. The guide vane angle is manipulated to control the power

produced/consumed. Following are few results showing the difference between models with and without PID controllers.

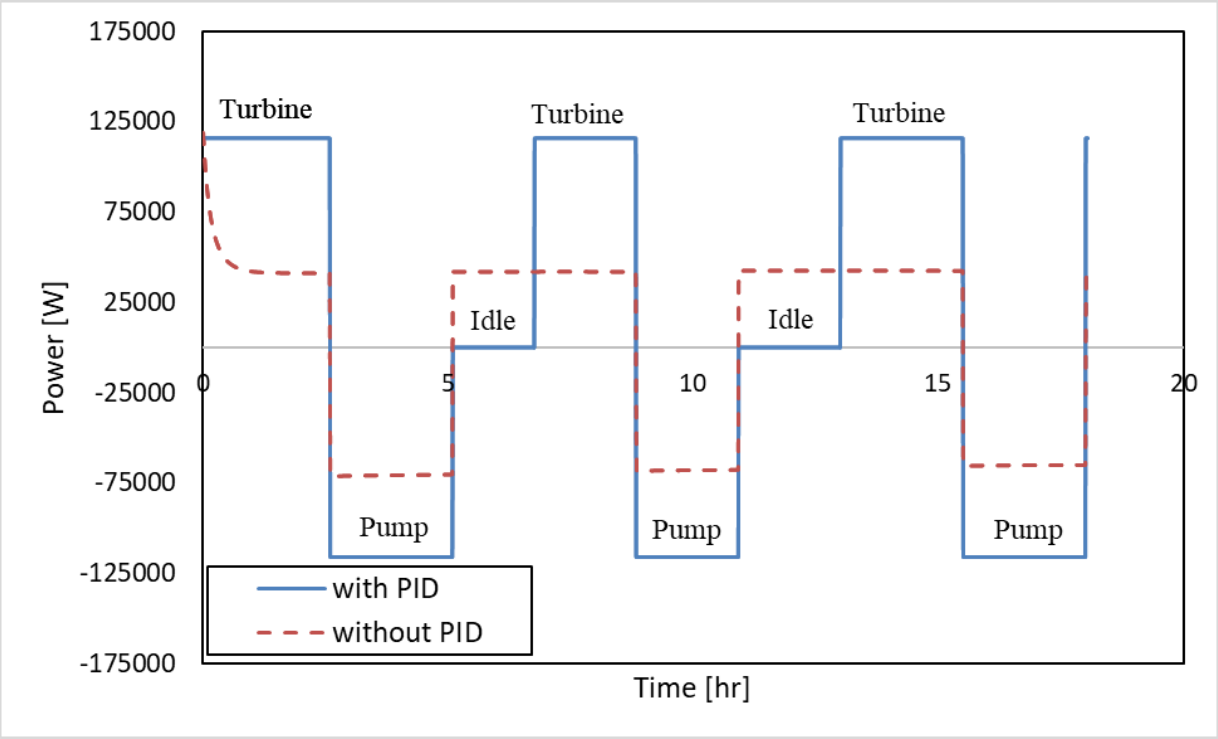

Figure D.1. Power profile during pumping and generation modes with and without PID controllers.

For the model with PID controller, the power is maintained at a value of 116074W, which is positive in turbine mode and negative in pump mode. This will become zero when the equipment is idle.

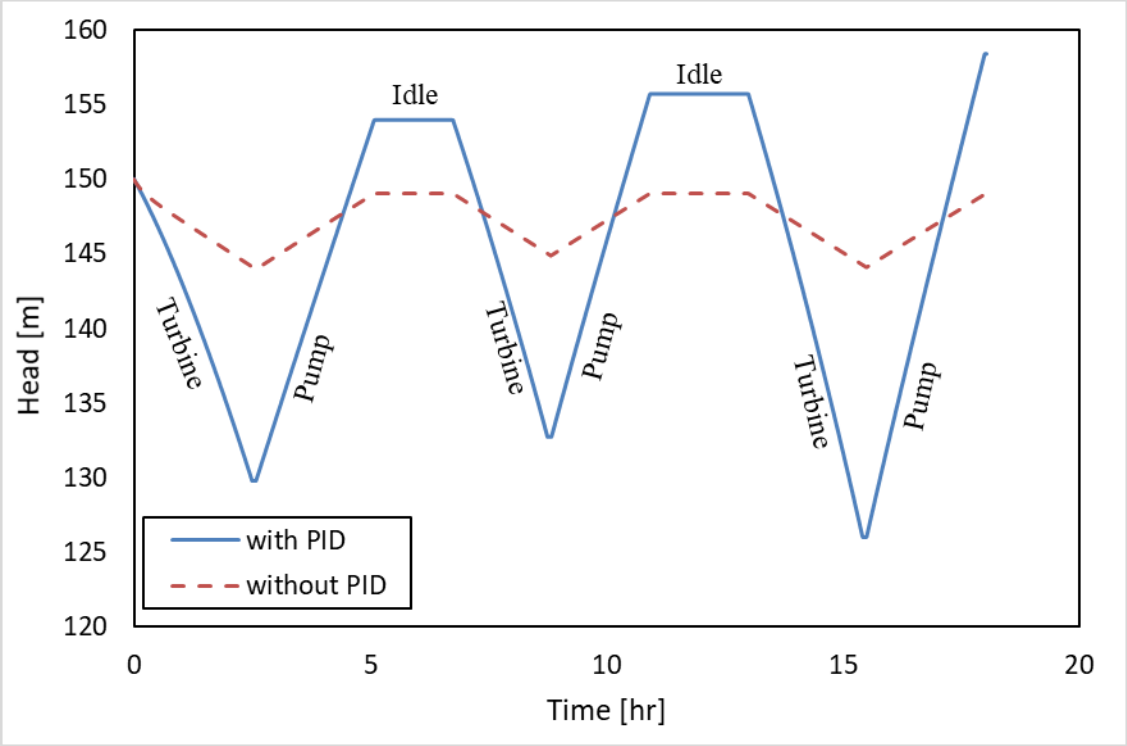

Figure D.2. Transient response in head during pumping and generation modes with and without PID controllers.

The power produced using PID controllers is higher compared to the power produced in absence of the controller. Therefore, to attain the power required the decrease in head is high when the PID controller is used compared to the absence of the controller. This trend can be seen in Figure D.2. It can be observed that during idle state in both the cases the change in head with time is constant. The head decreases in the turbine mode and increases in pump mode.

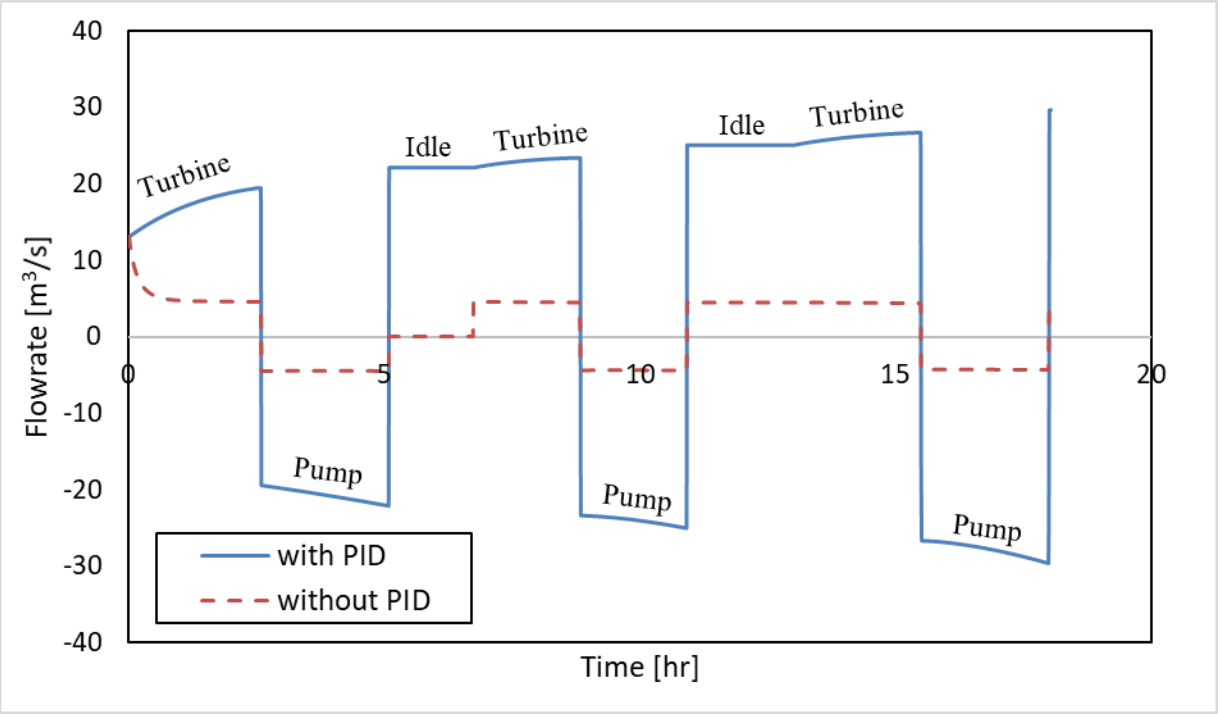

Figure D.3. Transient response in flowrate during pumping and generation modes with and without PID controllers.

As the head decreases the water level in the reservoir decreases, decreasing the net flowrate. However, in PID model to maintain the specific power generated by unit mass flowrate, there needs to be more mass flow for generating the same power. Therefore, the flowrate increases with time to maintain the power produced in turbine mode of operation as shown in Figure D.3.

Appendix E: Reduced order models

Because of high computational tractability and accuracy, reduced order models (ROM) can be used for optimization/scheduling/control of the plant. In this work reduced order models were developed for NaS and VRFB. These ROMs were used in integration with fossil-fueled power plant.

The sodium sulfur cell model developed in Chapter 2 was identified using non-linear additive autoregressive with exogenous input (NAARX).

E.1. Linear MIMO state space model

The nonlinear model of NaS cell developed in ACM is linearized to generate the linear MIMO state-space models.

In the state-space model, input or decision variable is:

1. Current (A)
2. SOD

The outputs are:

1. Cell Voltage (V)
2. Power (W)
3. Air mass flowrate (kg/s)

Since 650 variables are included in the large-scale model, the ROM is useful in reducing the computational cost.

E.2. Reduced order model

Non-linear additive autoregressive with exogenous input (NAARX) model is used to identify the model outputs. In NAARX model, the output variable at time 'k' depends on the input as well as the previous time step (k-1) output and is given as:

$$y(k) = \sum_{i=0}^{n} H_1(i,p)u(k-i)^p + \sum_{j=1}^{r} H_2(j,q)y(k-j)^q\,, \quad p = 1{:}\,P, q = 1{:}\,Q \quad \text{(E1)}$$

Least square estimate for parameter vector is given as:

$$H = (\varphi^T \varphi)^{-1} \varphi^T Y \quad \text{(E2)}$$

The linear output is given as:

$$y(k) = \varphi(k) H \quad \text{(E3)}$$

,where $y(k)$ is the output at time k, $\varphi(k)$ is the regression vector and H is the parameter vector.

Input memory 'n', output memory 'r', and 'p' and 'q' are determined by Akaike information criterion (AIC), which is given as:

$$AIC = N ln\left(\frac{TSE}{N}\right) + 2K \quad \text{(E4)}$$

,where N is the number of data points, TSE is the total squared error and K is the number of fitted parameters (size of the model). Model complexity is increased until the AIC value changes significantly. Once there is no significant difference in the AIC value then the simpler model is chosen.

As mentioned in Chapter 2, unlike all other batteries, NaS cell exists in two different phases. Before discharge operations begin, the sulfur electrode contains mostly sulfur. Then the sulfur electrode transitions to a two-phase mixture of sulfur and polysulfide. As the reaction progresses, more sodium ions react with the sulfur and the mole fraction of total sulfur decreases. Then the sulfur electrode becomes single-phase polysulfide. Therefore, because of the different voltage profiles in single and two-phase we had to generate four models (charging single-phase, charging two-phase, discharging single-phase and discharging two-phase).

Therefore, to identify the model 8 MATLAB models were generated (4 for voltage and 4 for air mass flowrate). The generated models were validated with the Aspen model as shown in Figure E1 and E2.

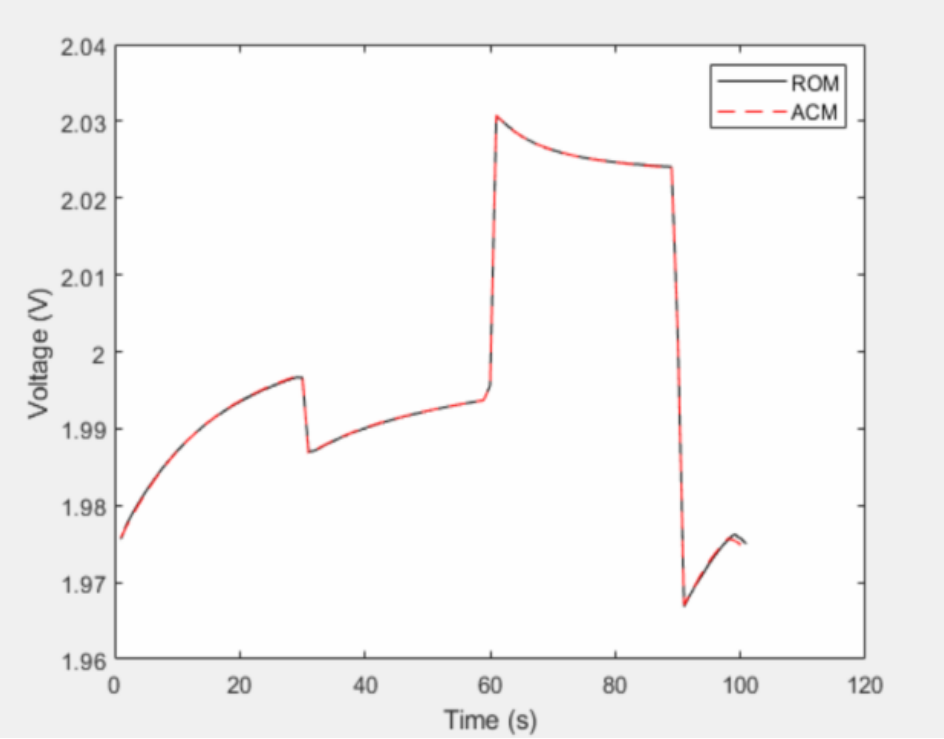

Figure E1. Comparison of voltage profile for ROM and ACM models.

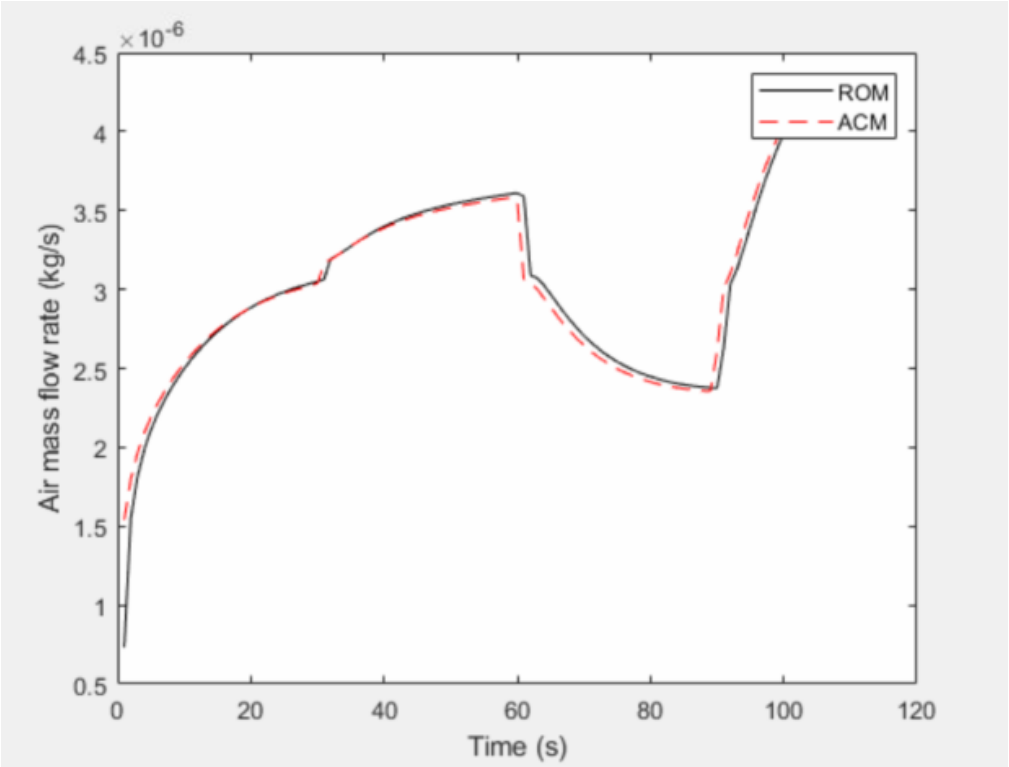

Figure E2. Comparison of air mass flowrate profile for ROM and ACM models.

The figures show that the developed model compares well with the full order model with error ~10^{-3} for both the profiles.

The following steps were considered while identifying the model:

1) State of discharge for sodium sulfur cell

Step 1:

Find initial/current energy capacity (kWh) of cell as a function of SOD.

$$E_t = f(SOD) \tag{E5}$$

Charging

$$E_t = 72.705(SOD)^4 - 21.378(SOD)^3 - 175.43(SOD)^2 - 9.1871(SOD) + 113.43 \tag{E6}$$

Discharging

$$E_t = -(72.705(SOD)^4 - 21.378(SOD)^3 - 175.43(SOD)^2 - 9.1871(SOD) + 113.43) + \varepsilon \tag{E7}$$

ε is the extra heat generated during discharge. $\varepsilon = 85.099$

Step 2:

Find new energy capacity:

$$E_{t+1} = E_t \pm \Delta E \tag{E8}$$

Step 3:

Using the new energy capacity, find new SOD using equation (E6) and equation (E7) for charging and discharging, respectively.

2) Voltage

Voltage is estimated using the NAARX model as mentioned before. Therefore, we have 4 voltage models which gives us 4 NAARX equations for model output 'voltage'.

$$V = f(I, SOD) \tag{E9}$$

4 equations => charging single-phase '$f1_v$', charging two-phase '$f2_v$', discharging single-phase '$f3_v$' and discharging two-phase '$f4_v$'.

3) Power

Power is calculated from voltage and current as follows:

$$P = V * I \tag{E10}$$

4) Air mass flow rate

Similar to voltage, air mass flowrate is estimated using NAARX equation. Therefore, we have 4 NAARX equations for air mass flowrate model output.

$$\dot{m}_{air} = f(P, SOD) \tag{E11}$$

4 equations => charging single-phase '$f1_m$', charging two-phase '$f2_m$', discharging single-phase '$f3_m$' and discharging two-phase '$f4_m$'.

5) Determining the phase and charge/ discharge

To determine if its charging or discharging and single-phase or two-phase we used a flag variable as follows:

Charging

$$flag_{charge} = \frac{1-\frac{I}{abs(I+1e^{-5})}}{2} \tag{E12}$$

Discharging

$$flag_{discharge} = \frac{1+\frac{I}{abs(I)}}{2} \tag{E13}$$

Single-phase

$$flag_{single} = \frac{1+\frac{SOD-55.8}{abs(SOD-55.8+1e^{-5})}}{2} \tag{E14}$$

Two-phase

$$flag_{two} = \frac{1-\frac{SOD-55.8}{abs(SOD-55.8+1e^{-5})}}{2} \tag{E15}$$

The flag variable helps to determine the phase and also if its charging or discharging. Therefore, the equations for voltage and air mass flowrate can be written in terms of flag variable as follows:

Air mass flow rate

$$\dot{m}_{air} = flag_{charge} * flag_{single} * f1_m + flag_{charge} * flag_{two} * f2_m + flag_{discharge} * flag_{single} * f3_m + flag_{discharge} * flag_{two} * f4_m \quad \text{(E16)}$$

Voltage

$$V = flag_{charge} * flag_{single} * f1_v + flag_{charge} * flag_{two} * f2_v + flag_{discharge} * flag_{single} * f3_v + flag_{discharge} * flag_{two} * f4_v \quad \text{(E17)}$$

These steps along with the estimated parameters will be used in the integration of NGCC and NaS battery model.

Appendix F: Publications and Presentations

Publications

1. Sarah Schaefer (Caprio), **Sai Pushpitha Vudata**, Debangsu Bhattacharyya, Richard Turton, "Transient Modeling and Simulation of a Non-isothermal Sodium-sulfur Cell", *Journal of Power Sources*, 453 (2020) 227849.
2. Kim, R., Wang, Y., **Vudata, S. P.**, Bhattacharyya, D., Lima, F. V., & Turton, R. (2020). "Dynamic Optimal Dispatch of Energy Systems with Intermittent Renewables and Damage Model", *Mathematics*, 8 (6) (2020) 868.
3. **Sai Pushpitha Vudata**, Debangsu Bhattacharyya, Richard Turton, "Dynamic Modeling of a High-Temperature Sodium Sulphur Battery Stack and Development of Model-Based Thermal Management Strategies for High Current-Density Operation" under review in *Journal of Energy.*
4. **Sai Pushpitha Vudata**, Debangsu Bhattacharyya, Richard Turton, "Transient modeling of Vanadium Redox Flow Battery Incorporating Different Capacity Fade Mechanisms" to be submitted in *Electrochimica Acta.*
5. **Sai Pushpitha Vudata**, Debangsu Bhattacharyya, Richard Turton, "Condition Monitoring of Vanadium Redox Flow Batteries through Co-estimation of Capacity Fade and State of Charge" to be submitted in *Electrochimica Acta.*

Accepted Presentations

1. **Sai Pushpitha Vudata**, Debangsu Bhattacharyya, Richard Turton, "Development of a Dynamic Model and Thermal Management Strategies for High-Temperature Sodium Sulfur Batteries", Paper 40i, AIChE Annual Meeting, Minneapolis, MN, October 29 – November 3, 2017.
2. **Sai Pushpitha Vudata**, Debangsu Bhattacharyya, Richard Turton, "Optimal Thermal Management of a High-Temperature Sodium Sulphur Battery", Paper 49e, AIChE Annual Meeting, Pittsburgh, PA, October 28 – November 2, 2018.
3. **Sai Pushpitha Vudata**, Debangsu Bhattacharyya, Richard Turton, "Design and Optimization of a Vanadium Redox Flow Battery for Load-Following Applications", Paper 226b 2019 AICHE Annual Meeting, Orlando, FL, Nov 10 – Nov 15, 2019.
4. Rebecca Kim, **Sai Pushpitha Vudata**, Yifan Wang, Debangsu Bhattacharyya, Richard Turton, "Scheduling of Baseload Power Plants and Batteries with Integration of Renewables", Poster 373f, AIChE Annual Meeting, Orlando, FL, November 10-15, 2019.
5. Manali S. Zantye, **Sai Pushpitha Vudata**, Yifan Wang, Debangsu Bhattacharyya, M.M. Faruque Hasan, "Optimal Selection and Design of Energy Storage Technologies Integrated with Advanced Energy Plants", Paper 576a 2019 AICHE Annual Meeting, Orlando, FL, Nov 10 – Nov 15, 2019.
6. **Sai Pushpitha Vudata**, Debangsu Bhattacharyya, Richard Turton, "Development of Condition Monitoring and Prognostic Capabilities for a Vanadium Redox Flow Battery", Paper 399d, Virtual AIChE Annual Meeting, November 16 – November 20, 2020.

7. Rebecca Kim, **Sai Pushpitha Vudata**, Yifan Wang, Debangsu Bhattacharyya, Fernando V. Lima and Richard Turton. Optimal Dispatch of Energy Systems Considering Penetration of Renewables and Power Plant Health. 2020 AIChE Annual Meeting, Virtual

References

[1] H. Ibrahim, A. Ilinca, and J. Perron, “Energy storage systems-Characteristics and comparisons,” *Renewable and Sustainable Energy Reviews*, vol. 12, no. 5. Pergamon, pp. 1221–1250, Jun. 01, 2008, doi: 10.1016/j.rser.2007.01.023.

[2] P. Sarda, E. Hedrick, K. Reynolds, D. Bhattacharyya, S. E. Zitney, and B. Omell, “processes Article,” 2018, doi: 10.3390/pr6110226.

[3] B. Sorensen, *Renewable Energy Conversion, Transmission and Storage*, 1st ed. AP, London, 2007.

[4] M. Beaudin, H. Zareipour, A. Schellenberglabe, and W. Rosehart, “Energy storage for mitigating the variability of renewable electricity sources: An updated review,” *Energy for Sustainable Development*, vol. 14, no. 4. Elsevier B.V., pp. 302–314, Dec. 01, 2010, doi: 10.1016/j.esd.2010.09.007.

[5] S. Nykamp, M. G. C. Bosman, A. Molderink, J. L. Hurink, and G. J. M. Smit, “Value of Storage in Distribution Grids—Competition or Cooperation of Stakeholders?,” *IEEE Trans. Smart Grid*, vol. 4, no. 3, pp. 1361–1370, Sep. 2013, doi: 10.1109/TSG.2013.2254730.

[6] D. Rastler, “Electricity energy storage technology options: a white paper primer on applications, costs, and benefits,” 2010.

[7] M. Hiremath, K. Derendorf, and T. Vogt, “Comparative life cycle assessment of battery storage systems for stationary applications,” *Environ. Sci. Technol.*, vol. 49, no. 8, pp. 4825–4833, 2015, doi: 10.1021/es504572q.

[8] “Electrical Energy Storage project team, International Electrotechnical Commission. “Electrical energy storage" White Paper IEC WP EES:2011-12(en).” [Online]. Available: https://www.iec.ch/whitepaper/pdf/iecWP-energystorage-LR-en.pdf.

[9] J. A. J. Makansi, “Energy Storage, The Missing Link in the Electricity Value Chain,” 2002. [Online]. Available: http://www.ridgeenergystorage.com/ESCWhitepaper.pdf.

[10] L. Li *et al.*, “A Stable Vanadium Redox-Flow Battery with High Energy Density for Large-Scale Energy Storage,” *Adv. Energy Mater.*, vol. 1, no. 3, pp. 394–400, May 2011, doi: 10.1002/aenm.201100008.

[11] A. Tang, J. Bao, and M. Skyllas-Kazacos, “Dynamic modelling of the effects of ion diffusion and side reactions on the capacity loss for vanadium redox flow battery,” *J. Power Sources*, vol. 196, no. 24, pp. 10737–10747, Dec. 2011, doi: 10.1016/j.jpowsour.2011.09.003.

[12] T. Hino and A. Lejeune, “Pumped Storage Hydropower Developments,” in *Comprehensive Renewable Energy*, Elsevier, 2012, pp. 405–434.

[13] P. W. C. Northrop, V. Ramadesigan, S. De, and V. R. Subramanian, “Coordinate Transformation, Orthogonal Collocation, Model Reformulation and Simulation of Electrochemical-Thermal Behavior of Lithium-Ion Battery Stacks,” *J. Electrochem. Soc.*, vol. 158, no. 12, p. A1461, 2011, doi: 10.1149/2.058112jes.

[14] L. Hao, Y. Wang, and Y. He, “Modeling of Ion Crossover in an All-Vanadium Redox Flow Battery with the Interfacial Effect at Membrane/Electrode Interfaces,” *J. Electrochem. Soc.*, vol. 166, no. 8, pp. A1310–A1322, Apr. 2019, doi: 10.1149/2.1061906jes.

[15] S. Rehman, L. M. Al-Hadhrami, and M. M. Alam, “Pumped hydro energy storage system: A technological review,” *Renew. Sustain. Energy Rev.*, vol. 44, pp. 586–598, Apr. 2015, doi: 10.1016/j.rser.2014.12.040.

[16] B. Dunn, H. Kamath, and J. M. Tarascon, “Electrical energy storage for the grid: A battery of choices,” *Science (80-.).*, vol. 334, no. 6058, pp. 928–935, 2011, doi: 10.1126/science.1212741.

[17] B. Battke, T. S. Schmidt, D. Grosspietsch, and V. H. Hoffmann, “A review and probabilistic model of lifecycle costs of stationary batteries in multiple applications,” *Renew. Sustain. Energy Rev.*, vol. 25, pp. 240–250, 2013, doi: 10.1016/j.rser.2013.04.023.

[18] A. R. Sparacino, G. F. Reed, R. J. Kerestes, B. M. Grainger, and Z. T. Smith, “Survey of battery energy storage systems and modeling techniques,” *IEEE Power Energy Soc. Gen. Meet.*, pp. 1–8, 2012, doi: 10.1109/PESGM.2012.6345071.

[19] D. Manz, J. Keller, and N. Miller, “Value propositions for utility-scale energy storage,” in *2011 IEEE/PES Power Systems Conference and Exposition*, Mar. 2011, pp. 1–10, doi: 10.1109/PSCE.2011.5772524.

[20] A. R. Dehghani-Sanij, E. Tharumalingam, M. B. Dusseault, and R. Fraser, “Study of energy storage systems and environmental challenges of batteries,” *Renew. Sustain. Energy Rev.*, vol. 104, no. November 2018, pp. 192–208, 2019, doi: 10.1016/j.rser.2019.01.023.

[21] K. Nestmeier, “Grid-integrated Storage Systems,” in *6th International Renewable Energy Storage Conference and Exhibition*, 2011, pp. 1188–1208.

[22] G. Girishkumar, B. McCloskey, A. C. Luntz, S. Swanson, and W. Wilcke, “Lithium-air battery: Promise and challenges,” *J. Phys. Chem. Lett.*, vol. 1, no. 14, pp. 2193–2203, 2010, doi: 10.1021/jz1005384.

[23] A. Yoshino, *Development of the Lithium-Ion Battery and Recent Technological Trends*. Elsevier, 2014.

[24] I. Kim *et al.*, “A room temperature Na/S battery using a β″ alumina solid electrolyte separator, tetraethylene glycol dimethyl ether electrolyte, and a S/C composite cathode,” *J. Power Sources*, vol. 301, pp. 332–337, 2016, doi: 10.1016/j.jpowsour.2015.09.120.

[25] J. B. Goodenough and K. S. Park, “The Li-ion rechargeable battery: A perspective,” *J. Am. Chem. Soc.*, vol. 135, no. 4, pp. 1167–1176, 2013, doi: 10.1021/ja3091438.

[26] G. Nikiforidis, M. C. M. Van de Sanden, and M. N. Tsampas, “High and intermediate temperature sodium-sulfur batteries for energy storage: development, challenges and perspectives,” *RSC Adv.*, vol. 9, no. 10, pp. 5649–5673, 2019, doi: 10.1039/c8ra08658c.

[27] C. Delmas, “Sodium and Sodium-Ion Batteries: 50 Years of Research,” *Adv. Energy Mater.*, vol. 8, no. 17, pp. 1–9, 2018, doi: 10.1002/aenm.201703137.

[28] S. Wei *et al.*, “A stable room-temperature sodium-sulfur battery,” *Nat. Commun.*, vol. 7, pp. 1–10, 2016, doi: 10.1038/ncomms11722.

[29] P. Adelhelm, P. Hartmann, C. L. Bender, M. Busche, C. Eufinger, and J. Janek, “From lithium to sodium: cell chemistry of room temperature sodium–air and sodium–sulfur batteries,” *Beilstein J. Nanotechnol.*, vol. 6, pp. 1016–1055, Apr. 2015, doi: 10.3762/bjnano.6.105.

[30] J. L. Sudworth and A. R. Tilley, *The sodium sulfur battery*. London; New York: Chapman and Hall, 1985.

[31] T. Oshima, M. Kajita, and A. Okuno, “Development of Sodium-Sulfur Batteries,” *Int. J. Appl. Ceram. Technol.*, vol. 1, no. 3, pp. 269–276, Jan. 2005, doi: 10.1111/j.1744-7402.2004.tb00179.x.

[32] C. J. Rydh and B. A. Sandén, “Energy analysis of batteries in photovoltaic systems. Part I: Performance and energy requirements,” *Energy Convers. Manag.*, vol. 46, no. 11–12, pp. 1957–1979, Jul. 2005, doi: 10.1016/j.enconman.2004.10.003.

[33] D. Kumar, S. K. Rajouria, S. B. Kuhar, and D. K. Kanchan, “Progress and prospects of sodium-sulfur batteries: A review,” *Solid State Ionics*, vol. 312, pp. 8–16, Dec. 2017, doi: 10.1016/J.SSI.2017.10.004.

[34] D. Kumar, M. Suleman, and S. A. Hashmi, “Studies on poly(vinylidene fluoride-co-hexafluoropropylene) based gel electrolyte nanocomposite for sodium–sulfur batteries,” *Solid State Ionics*, vol. 202, no. 1, pp. 45–53, Nov. 2011, doi: 10.1016/j.ssi.2011.09.001.

[35] R. Carter, L. Oakes, A. Douglas, N. Muralidharan, A. P. Cohn, and C. L. Pint, “A Sugar-Derived Room-Temperature Sodium Sulfur Battery with Long Term Cycling Stability,” *Nano Lett.*, vol. 17, no. 3, pp. 1863–1869, Mar. 2017, doi: 10.1021/acs.nanolett.6b05172.

[36] J. Kummer and N. Weber, “US3413150A,” 1968.

[37] M. C. H. McKubre, F. L. Tanzella, and S. I. Smedley, “The Electromotive Force of the Na/S Cell,” *J. Electrochem. Soc.*, vol. 136, no. 2, pp. 303–305, 1989, doi: 10.1149/1.2096625.

[38] M. C. H. McKubre, S. I. Smedley, and F. L. Tanzella, “The Electrochemical Impedance of the Na/S Cell: I . Experiments and Results,” *J. Electrochem. Soc.*, vol. 136, no. 7, pp. 1962–1968, Jul. 1989, doi: 10.1149/1.2097101.

[39] J. G. Gibson, “The distribution of potential and electrochemical reaction rate in molten polysulphide electrodes,” *J. Appl. Electrochem.*, vol. 4, no. 2, pp. 125–134, May 1974, doi: 10.1007/BF00609021.

[40] M. W. Breiter and B. Dunn, “Potential distribution model for rechargeable sulphur electrodes in sodium-sulphur cells,” *J. Appl. Electrochem.*, vol. 9, no. 3, pp. 291–299, May 1979, doi: 10.1007/BF01112482.

[41] R. Knoedler, “Calorimetric Determination of the Heat Generation Rate of Sodium-Sulfur Cells during Discharge and Charge,” *J. Electrochem. Soc.*, vol. 131, no. 4, pp. 845–850, 1984, doi: 10.1149/1.2115711.

[42] R. Knoedler, “Thermal properties of sodium-sulphur cells,” *J. Appl. Electrochem.*, vol. 14, no. 1, pp. 39–46, Jan. 1984, doi: 10.1007/BF00611256.

[43] H. Kawamoto, “Two-Dimensional Distribution of Sodium Polysulfide Composition in Sulfur Electrodes of Sodium-Sulfur Cells,” *J. Electrochem. Soc.*, vol. 136, no. 7, pp. 1851–1860, Jul. 1989, doi: 10.1149/1.2097059.

[44] H. Kawamoto and Y. Kusakabe, “Performance and Thermal Behavior of Sodium-Sulfur Cell under High Current Density Operations,” *J. Electrochem. Soc.*, vol. 136, no. 5, pp. 1355–1361, 1989, doi: 10.1149/1.2096921.

[45] H. Kawamoto, “Dynamic simulation of the charge-discharge characteristics of the sodium-sulphur cell,” *J. Appl. Electrochem.*, vol. 21, no. 5, pp. 409–414, 1991, doi: 10.1007/BF01024576.

[46] Z. F. Hussien, L. W. Cheung, M. F. M. Siam, and A. B. Ismail, “Modeling of sodium sulfur battery for power system applications,” *Elektrika*, vol. 9, no. 2, pp. 66–72, 2007.

[47] A. E. Sarasua, M. G. Molina, D. E. Pontoriero, and P. E. Mercado, “Modelling of NAS energy storage system for power system applications,” in *2010 IEEE/PES Transmission and Distribution Conference and Exposition: Latin America (T&D-LA)*, Nov. 2010, pp. 555–560, doi: 10.1109/TDC-LA.2010.5762937.

[48] J. K. Min and C.-H. Lee, “Numerical study on the thermal management system of a molten sodium-sulfur battery module,” *J. Power Sources*, vol. 210, pp. 101–109, Jul. 2012, doi: 10.1016/j.jpowsour.2012.03.028.

[49] M. Aygun, “A computational model for thermal management of battery storage systems,” West Virginia University Libraries, 2016.

[50] Z. Wen, J. Cao, Z. Gu, X. Xu, F. Zhang, and Z. Lin, “Research on sodium sulfur battery for energy storage,” *Solid State Ionics*, vol. 179, no. 27–32, pp. 1697–1701, 2008, doi: 10.1016/j.ssi.2008.01.070.

[51] T. Risch and J. Newman, “Transference Number Calculations for Sodium Polysulfides,” *J. Electrochem. Soc.*, vol. 135, no. 7, pp. 1715–1718, 1988, doi: 10.1149/1.2096103.

[52] B. Cleaver and A. J. Davies, “Properties of fused polysulphides—III. EMF measurements on the sodium-sulphur cell, and sulphur activities and constitution in fused sodium polysulphides,” *Electrochim. Acta*, vol. 18, no. 10, pp. 733–739, Oct. 1973, doi: 10.1016/0013-4686(73)80064-7.

[53] B. Cleaver, A. J. Davies, and M. D. Hames, “Properties of fused polysulphides—I. The electrical conductivity of fused sodium and potassium polysulphides,” *Electrochim. Acta*, vol. 18, no. 10, pp. 719–726, Oct. 1973, doi: 10.1016/0013-4686(73)80062-3.

[54] S. D. Thompson and J. Newman, “Differential Diffusion Coefficients of Sodium Polysulfide Melts,” *J. Electrochem. Soc.*, vol. 136, no. 11, pp. 3362–3369, 1989, doi: 10.1149/1.2096451.

[55] M. . Ryan, R. . Williams, C. . Allevato, C. . Vining, C. . Lowe-Ma, and S. . Robie, “Thermophysical properties of sodium β″-alumina polycrystalline ceramic,” *J. Phys. Chem. Solids*, vol. 55, no. 11, pp. 1255–1260, Nov. 1994, doi: 10.1016/0022-3697(94)90207-0.

[56] H. Kawamoto and M. Wada, “Two-Dimensional Distribution of Electrochemical Reaction Rate in Porous Sulfur Electrodes of Sodium-Sulfur Cells,” *J. Electrochem. Soc.*, vol. 134, no. 2, pp. 280–285, 1987, doi: 10.1149/1.2100446.

[57] H. KAWAMOTO, “Numerical Analysis on Potential Distribution and Resistance of Sodium-Sulphur Batteries,” *Denki Kagaku oyobi Kogyo Butsuri Kagaku*, vol. 52, no. 9, pp. 589–595, Sep. 1984, doi: 10.5796/kogyobutsurikagaku.52.589.

[58] M. S. Whittingham and R. A. Huggins, “Measurement of Sodium Ion Transport in Beta Alumina Using Reversible Solid Electrodes,” *J. Chem. Phys.*, vol. 54, no. 1, pp. 414–416, 1971, doi: 10.1063/1.1674623.

[59] A. V. VIRKAR, G. R. MILLER, and R. S. GORDON, “Resistivity-Microstructure Relations in Lithia-Stabilized Polycrystalline beta"-Alumina,” *J. Am. Ceram. Soc.*, vol. 61, no. 5–6, pp. 250–252, May 1978, doi: 10.1111/j.1151-2916.1978.tb09292.x.

[60] Y. Ito, H. Hayashi, N. Hayafuji, and S. Yoshizawa, “Energy flow through β-alumina solid electrolyte,” *Electrochim. Acta*, vol. 30, no. 5, pp. 701–703, May 1985, doi: 10.1016/0013-4686(85)80114-6.

[61] A. C. Buechele, L. C. De Jonghe, and D. Hitchcock, “Degradation of Sodium β″-Alumina: Effect of Microstructure,” *J. Electrochem. Soc.*, vol. 130, no. 5, pp. 1042–1049, 1983, doi:

10.1149/1.2119881.

[62] P. Breeze, “Power System Energy Storage Technologies,” in *Power Generation Technologies*, Elsevier, 2019, pp. 219–249.

[63] G. Eck, “Design of the thermal management systems for sodium-sulphur traction batteries using battery models,” *J. Power Sources*, vol. 17, no. 1–3, pp. 226–227, Jan. 1986, doi: 10.1016/0378-7753(86)80041-6.

[64] J. R. Hartenstine, “Heat Pipes for Sodium-Sulfur Batteries,” *Final Rep.*, 1988.

[65] C. Menale, F. D’Annibale, B. Mazzarotta, and R. Bubbico, “Thermal management of lithium-ion batteries: An experimental investigation,” *Energy*, vol. 182, pp. 57–71, Sep. 2019, doi: 10.1016/j.energy.2019.06.017.

[66] D. H. Doughty, P. C. Butler, R. G. Jungst, and E. P. Roth, “Lithium battery thermal models,” *J. Power Sources*, vol. 110, no. 2, pp. 357–363, Aug. 2002, doi: 10.1016/S0378-7753(02)00198-2.

[67] H. Sun, X. Wang, B. Tossan, and R. Dixon, “Three-dimensional thermal modeling of a lithium-ion battery pack,” *J. Power Sources*, vol. 206, pp. 349–356, May 2012, doi: 10.1016/j.jpowsour.2012.01.081.

[68] Y. Ye, Y. Shi, N. Cai, J. Lee, and X. He, “Electro-thermal modeling and experimental validation for lithium ion battery,” *J. Power Sources*, vol. 199, pp. 227–238, Feb. 2012, doi: 10.1016/j.jpowsour.2011.10.027.

[69] R. Zhao, S. Zhang, J. Liu, and J. Gu, “A review of thermal performance improving methods of lithium ion battery: Electrode modification and thermal management system,” *J. Power Sources*, vol. 299, pp. 557–577, Dec. 2015, doi: 10.1016/j.jpowsour.2015.09.001.

[70] V. G. Choudhari, A. S. Dhoble, and S. Panchal, “Numerical analysis of different fin structures in phase change material module for battery thermal management system and its optimization,” *Int. J. Heat Mass Transf.*, vol. 163, p. 120434, Dec. 2020, doi: 10.1016/j.ijheatmasstransfer.2020.120434.

[71] M. S. Patil, J. Seo, S. Panchal, and M. Lee, “Numerical study on sensitivity analysis of factors influencing liquid cooling with double cold-plate for lithium-ion pouch cell,” *Int. J. Energy Res.*, vol. 45, no. 2, pp. 2533–2559, Feb. 2021, doi: 10.1002/er.5946.

[72] M. S. Patil, J.-H. Seo, S. Panchal, S.-W. Jee, and M.-Y. Lee, “Investigation on thermal performance of water-cooled Li-ion pouch cell and pack at high discharge rate with U-turn type microchannel cold plate,” *Int. J. Heat Mass Transf.*, vol. 155, p. 119728, Jul. 2020, doi: 10.1016/j.ijheatmasstransfer.2020.119728.

[73] S. Panchal, K. Gudlanarva, M.-K. Tran, R. Fraser, and M. Fowler, “High Reynold’s Number Turbulent Model for Micro-Channel Cold Plate Using Reverse Engineering Approach for Water-Cooled Battery in Electric Vehicles,” *Energies*, vol. 13, no. 7, p. 1638, Apr. 2020, doi: 10.3390/en13071638.

[74] S. Park and D. Jung, “Battery cell arrangement and heat transfer fluid effects on the parasitic power consumption and the cell temperature distribution in a hybrid electric vehicle,” *J. Power Sources*, vol. 227, pp. 191–198, Apr. 2013, doi: 10.1016/j.jpowsour.2012.11.039.

[75] Z. Rao and S. Wang, “A review of power battery thermal energy management,” *Renew. Sustain. Energy Rev.*, vol. 15, no. 9, pp. 4554–4571, Dec. 2011, doi: 10.1016/j.rser.2011.07.096.

[76] K. Yu, X. Yang, Y. Cheng, and C. Li, “Thermal analysis and two-directional air flow thermal management for lithium-ion battery pack,” *J. Power Sources*, vol. 270, pp. 193–200, Dec. 2014, doi: 10.1016/j.jpowsour.2014.07.086.

[77] Y. S. Choi and D. M. Kang, “Prediction of thermal behaviors of an air-cooled lithium-ion battery system for hybrid electric vehicles,” *J. Power Sources*, vol. 270, pp. 273–280, Dec. 2014, doi: 10.1016/j.jpowsour.2014.07.120.

[78] L. Fan, J. M. Khodadadi, and A. A. Pesaran, “A parametric study on thermal management of an air-cooled lithium-ion battery module for plug-in hybrid electric vehicles,” *J. Power Sources*, vol. 238, pp. 301–312, Sep. 2013, doi: 10.1016/j.jpowsour.2013.03.050.

[79] R. Kizilel, R. Sabbah, J. R. Selman, and S. Al-Hallaj, “An alternative cooling system to enhance the safety of Li-ion battery packs,” *J. Power Sources*, vol. 194, no. 2, pp. 1105–1112, Dec. 2009, doi: 10.1016/j.jpowsour.2009.06.074.

[80] K. Pielichowska and K. Pielichowski, “Phase change materials for thermal energy storage,” *Prog. Mater. Sci.*, vol. 65, pp. 67–123, Aug. 2014, doi: 10.1016/j.pmatsci.2014.03.005.

[81] S. Al-Hallaj and J. . Selman, “Thermal modeling of secondary lithium batteries for electric vehicle/hybrid electric vehicle applications,” *J. Power Sources*, vol. 110, no. 2, pp. 341–348, Aug. 2002, doi: 10.1016/S0378-7753(02)00196-9.

[82] Z. Ling *et al.*, “Experimental and numerical investigation of the application of phase change materials in a simulative power batteries thermal management system,” *Appl. Energy*, vol. 121, pp. 104–113, May 2014, doi: 10.1016/j.apenergy.2014.01.075.

[83] N. Javani, I. Dincer, G. F. Naterer, and B. S. Yilbas, “Heat transfer and thermal management with PCMs in a Li-ion battery cell for electric vehicles,” *Int. J. Heat Mass Transf.*, vol. 72, pp. 690–703, May 2014, doi: 10.1016/j.ijheatmasstransfer.2013.12.076.

[84] N. Nieto, L. Díaz, J. Gastelurrutia, F. Blanco, J. C. Ramos, and A. Rivas, “Novel thermal management system design methodology for power lithium-ion battery,” *J. Power Sources*, vol. 272, pp. 291–302, Dec. 2014, doi: 10.1016/j.jpowsour.2014.07.169.

[85] R. Bubbico, F. D’Annibale, B. Mazzarotta, and C. Menale, “Analysis of Passive Temperature Control Systems Using Phase Change Materials for Application to Secondary Batteries Cooling,” *J. Therm. Sci. Eng. Appl.*, vol. 10, no. 6, Dec. 2018, doi: 10.1115/1.4040643.

[86] Z. Ling, F. Wang, X. Fang, X. Gao, and Z. Zhang, “A hybrid thermal management system for lithium ion batteries combining phase change materials with forced-air cooling,” *Appl. Energy*, vol. 148, pp. 403–409, Jun. 2015, doi: 10.1016/j.apenergy.2015.03.080.

[87] L. Ianniciello, P. H. Biwole, and P. Achard, “A Hybrid System for Battery Thermal Management for Electric Vehicles,” 2017.

[88] H. Fathabadi, “High thermal performance lithium-ion battery pack including hybrid active–passive thermal management system for using in hybrid/electric vehicles,” *Energy*, vol. 70, pp. 529–538, Jun. 2014, doi: 10.1016/j.energy.2014.04.046.

[89] S. Schaefer (Caprio), S. P. Vudata, D. Bhattacharyya, and R. Turton, “Transient modeling and simulation of a nonisothermal sodium–sulfur cell,” *J. Power Sources*, vol. 453, p. 227849, Mar. 2020, doi: 10.1016/j.jpowsour.2020.227849.

[90] L. Cai and R. E. White, “Reduction of Model Order Based on Proper Orthogonal Decomposition for Lithium-Ion Battery Simulations,” *J. Electrochem. Soc.*, vol. 156, no. 3, p. A154, 2009, doi:

10.1149/1.3049347.

[91] L. Cai and R. E. White, “Efficient Modeling for a Lithium-Ion Battery Using the Proper Orthogonal Decomposition and the Orthogonal Collocation on Finite Elements,” 2010.

[92] J. C. Forman, S. Bashash, J. L. Stein, and H. K. Fathy, “Reduction of an Electrochemistry-Based Li-Ion Battery Model via Quasi-Linearization and Padé Approximation,” *J. Electrochem. Soc.*, vol. 158, no. 2, p. A93, 2011, doi: 10.1149/1.3519059.

[93] S.-I. Lee, Y.-S. Kim, and H.-S. Chun, “Modeling on lithium insertion of porous carbon electrodes,” *Electrochim. Acta*, vol. 47, no. 7, pp. 1055–1067, Jan. 2002, doi: 10.1016/S0013-4686(01)00835-0.

[94] V. R. Subramanian, V. Boovaragavan, and V. D. Diwakar, “Toward real-time simulation of physics based lithium-ion battery models,” *Electrochem. Solid-State Lett.*, vol. 10, no. 11, pp. 255–260, 2007, doi: 10.1149/1.2776128.

[95] A. Bito, “Overview of the sodium-sulfur battery for the IEEE stationary battery committee,” in *IEEE Power Engineering Society General Meeting, 2005*, pp. 2346–2349, doi: 10.1109/PES.2005.1489556.

[96] W. Jung, J. Jeong, J. Kim, and D. Chang, “Optimization of hybrid off-grid system consisting of renewables and Li-ion batteries,” *J. Power Sources*, vol. 451, p. 227754, Mar. 2020, doi: 10.1016/j.jpowsour.2020.227754.

[97] J. Liu, X. Chen, S. Cao, and H. Yang, “Overview on hybrid solar photovoltaic-electrical energy storage technologies for power supply to buildings,” *Energy Convers. Manag.*, vol. 187, pp. 103–121, May 2019, doi: 10.1016/j.enconman.2019.02.080.

[98] K.-N. Jung, J. Kim, Y. Yamauchi, M.-S. Park, J.-W. Lee, and J. H. Kim, “Rechargeable lithium–air batteries: a perspective on the development of oxygen electrodes,” *J. Mater. Chem. A*, vol. 4, no. 37, pp. 14050–14068, 2016, doi: 10.1039/C6TA04510C.

[99] K. B. Dönmez, M. Gençten, and Y. Şahin, “A performance comparison of protective silicate-coated lead and non-coated lead electrodes in various kind electrolytes of gel valve-regulated lead-acid battery,” *Ionics (Kiel).*, vol. 24, no. 11, pp. 3655–3664, Nov. 2018, doi: 10.1007/s11581-018-2551-1.

[100] M. GENÇTEN, “Investigation the Effects of Boehmite and Gibbsite on the Electrochemical Behaviours of Gel-VRLA Batteries,” *Int. J. Electrochem. Sci.*, pp. 11741–11751, Dec. 2018, doi: 10.20964/2018.12.15.

[101] K. B. Dönmez, M. Gençten, and Y. Şahin, “A novel polysiloxane-based polymer as a gel agent for gel–VRLA batteries,” *Ionics (Kiel).*, vol. 23, no. 8, pp. 2077–2089, Aug. 2017, doi: 10.1007/s11581-017-2040-y.

[102] M. Gençten, K. B. Dönmez, Y. Şahin, K. Pekmez, and E. Suvacı, “Voltammetric and electrochemical impedimetric behavior of silica-based gel electrolyte for valve-regulated lead-acid battery,” *J. Solid State Electrochem.*, vol. 18, no. 9, pp. 2469–2479, Sep. 2014, doi: 10.1007/s10008-014-2507-y.

[103] Natasha, C. Dumat, M. Shahid, S. Khalid, and B. Murtaza, “Lead Pollution and Human Exposure: Forewarned is Forearmed, and the Question Now Becomes How to Respond to the Threat!,” 2020, pp. 33–65.

[104] M. Oswal, J. Paul, and R. Zhao, “A Comparative Study of Lithium-Ion Batteries,” 2010.

[105] H. Chen, T. N. Cong, W. Yang, C. Tan, Y. Li, and Y. Ding, “Progress in electrical energy storage system: A critical review,” *Prog. Nat. Sci.*, vol. 19, no. 3, pp. 291–312, Mar. 2009, doi: 10.1016/j.pnsc.2008.07.014.

[106] C. Ponce de León, A. Frías-Ferrer, J. González-García, D. A. Szánto, and F. C. Walsh, “Redox flow cells for energy conversion,” *J. Power Sources*, vol. 160, no. 1, pp. 716–732, Sep. 2006, doi: 10.1016/j.jpowsour.2006.02.095.

[107] M. Skyllas-Kazacos, M. H. Chakrabarti, S. A. Hajimolana, F. S. Mjalli, and M. Saleem, “Progress in Flow Battery Research and Development,” *J. Electrochem. Soc.*, vol. 158, no. 8, p. R55, 2011, doi: 10.1149/1.3599565.

[108] C. Choi *et al.*, “A review of vanadium electrolytes for vanadium redox flow batteries,” *Renew. Sustain. Energy Rev.*, vol. 69, pp. 263–274, Mar. 2017, doi: 10.1016/j.rser.2016.11.188.

[109] N. Kocyigit, M. Gencten, M. Sahin, and Y. Sahin, “A novel vanadium/cobalt redox couple in aqueous acidic solution for redox flow batteries,” *Int. J. Energy Res.*, vol. 44, no. 1, pp. 411–424, Jan. 2020, doi: 10.1002/er.4938.

[110] K. Lourenssen, J. Williams, F. Ahmadpour, R. Clemmer, and S. Tasnim, “Vanadium redox flow batteries: A comprehensive review,” *J. Energy Storage*, vol. 25, p. 100844, Oct. 2019, doi: 10.1016/j.est.2019.100844.

[111] X. Yuan *et al.*, “A review of all-vanadium redox flow battery durability: Degradation mechanisms and mitigation strategies,” *Int. J. Energy Res.*, p. er.4607, Jun. 2019, doi: 10.1002/er.4607.

[112] F.-C. Gu, H.-C. Chen, and K.-Y. Li, “Mathematic Modeling and Performance Analysis of Vanadium Redox Flow Battery,” *Energy & Fuels*, vol. 34, no. 8, pp. 10142–10147, Aug. 2020, doi: 10.1021/acs.energyfuels.0c01536.

[113] M. Gencten and Y. Sahin, “A critical review on progress of the electrode materials of vanadium redox flow battery,” *Int. J. Energy Res.*, vol. 44, no. 10, pp. 7903–7923, Aug. 2020, doi: 10.1002/er.5487.

[114] A. Z. Weber, M. M. Mench, J. P. Meyers, P. N. Ross, J. T. Gostick, and Q. Liu, “Redox flow batteries: a review,” *J. Appl. Electrochem.*, vol. 41, no. 10, pp. 1137–1164, Oct. 2011, doi: 10.1007/s10800-011-0348-2.

[115] P. Leung, X. Li, C. Ponce de León, L. Berlouis, C. T. J. Low, and F. C. Walsh, “Progress in redox flow batteries, remaining challenges and their applications in energy storage,” *RSC Adv.*, vol. 2, no. 27, p. 10125, 2012, doi: 10.1039/c2ra21342g.

[116] W. Wang, Q. Luo, B. Li, X. Wei, L. Li, and Z. Yang, “Recent Progress in Redox Flow Battery Research and Development,” *Adv. Funct. Mater.*, vol. 23, no. 8, pp. 970–986, Feb. 2013, doi: 10.1002/adfm.201200694.

[117] R. Ye *et al.*, “Redox Flow Batteries for Energy Storage: A Technology Review,” *J. Electrochem. Energy Convers. Storage*, vol. 15, no. 1, Feb. 2018, doi: 10.1115/1.4037248.

[118] B. K. Das, Y. M. Al-Abdeli, and M. Woolridge, “Effects of battery technology and load scalability on stand-alone PV/ICE hybrid micro-grid system performance,” *Energy*, vol. 168, pp. 57–69, Feb. 2019, doi: 10.1016/j.energy.2018.11.033.

[119] M. Ulaganathan, V. Aravindan, Q. Yan, S. Madhavi, M. Skyllas-Kazacos, and T. M. Lim, “Recent Advancements in All-Vanadium Redox Flow Batteries,” *Adv. Mater. Interfaces*, vol. 3, no. 1, p. 1500309, Jan. 2016, doi: 10.1002/admi.201500309.

[120] M. Martínez, M. G. Molina, and P. E. Mercado, "Optimal sizing method of vanadium redox flow battery to provide load frequency control in power systems with intermittent renewable generation," *IET Renew. Power Gener.*, vol. 11, no. 14, pp. 1804–1811, Dec. 2017, doi: 10.1049/iet-rpg.2016.0798.

[121] B. Xiong, J. Zhao, Y. Su, Z. Wei, and M. Skyllas-Kazacos, "State of Charge Estimation of Vanadium Redox Flow Battery Based on Sliding Mode Observer and Dynamic Model Including Capacity Fading Factor," *IEEE Trans. Sustain. Energy*, vol. 8, no. 4, pp. 1658–1667, Oct. 2017, doi: 10.1109/TSTE.2017.2699288.

[122] K. J. Kim, M.-S. Park, Y.-J. Kim, J. H. Kim, S. X. Dou, and M. Skyllas-Kazacos, "A technology review of electrodes and reaction mechanisms in vanadium redox flow batteries," *J. Mater. Chem. A*, vol. 3, no. 33, pp. 16913–16933, 2015, doi: 10.1039/C5TA02613J.

[123] M. Skyllas-Kazacos and F. Grossmith, "Efficient Vanadium Redox Flow Cell," *J. Electrochem. Soc.*, vol. 134, no. 12, pp. 2950–2953, Dec. 1987, doi: 10.1149/1.2100321.

[124] P. Alotto, M. Guarnieri, F. Moro, and A. Stella, "Redox Flow Batteries for large scale energy storage," in *2012 IEEE International Energy Conference and Exhibition (ENERGYCON)*, Sep. 2012, pp. 293–298, doi: 10.1109/EnergyCon.2012.6347770.

[125] M. Rychcik and M. Skyllas-Kazacos, "Characteristics of a new all-vanadium redox flow battery," *J. Power Sources*, vol. 22, no. 1, pp. 59–67, Jan. 1988, doi: 10.1016/0378-7753(88)80005-3.

[126] F. T. Wandschneider *et al.*, "Model of a vanadium redox flow battery with an anion exchange membrane and a Larminie-correction," *J. Power Sources*, vol. 272, pp. 436–447, Dec. 2014, doi: 10.1016/j.jpowsour.2014.08.082.

[127] S. I. Hossain, M. A. Aziz, and S. Shanmugam, "Ultrahigh Ion-Selective and Durable Nafion-NdZr Composite Layer Membranes for All-Vanadium Redox Flow Batteries," *ACS Sustain. Chem. Eng.*, vol. 8, no. 4, pp. 1998–2007, Feb. 2020, doi: 10.1021/acssuschemeng.9b06541.

[128] T. Sukkar and M. Skyllas-Kazacos, "Water transfer behaviour across cation exchange membranes in the vanadium redox battery," *J. Memb. Sci.*, vol. 222, no. 1–2, pp. 235–247, Sep. 2003, doi: 10.1016/S0376-7388(03)00309-0.

[129] C. Sun, J. Chen, H. Zhang, X. Han, and Q. Luo, "Investigations on transfer of water and vanadium ions across Nafion membrane in an operating vanadium redox flow battery," *J. Power Sources*, vol. 195, no. 3, pp. 890–897, Feb. 2010, doi: 10.1016/j.jpowsour.2009.08.041.

[130] M. Skyllas-Kazacos and L. Goh, "Modeling of vanadium ion diffusion across the ion exchange membrane in the vanadium redox battery," *J. Memb. Sci.*, vol. 399–400, pp. 43–48, May 2012, doi: 10.1016/j.memsci.2012.01.024.

[131] K. W. Knehr, E. Agar, C. R. Dennison, A. R. Kalidindi, and E. C. Kumbur, "A Transient Vanadium Flow Battery Model Incorporating Vanadium Crossover and Water Transport through the Membrane," *J. Electrochem. Soc.*, vol. 159, no. 9, pp. A1446–A1459, Jan. 2012, doi: 10.1149/2.017209jes.

[132] Y. Lei, B. W. Zhang, B. F. Bai, and T. S. Zhao, "A transient electrochemical model incorporating the Donnan effect for all-vanadium redox flow batteries," *J. Power Sources*, vol. 299, pp. 202–211, Dec. 2015, doi: 10.1016/j.jpowsour.2015.08.100.

[133] R. A. Elgammal, Z. Tang, C.-N. Sun, J. Lawton, and T. A. Zawodzinski, "Species Uptake and Mass Transport in Membranes for Vanadium Redox Flow Batteries," *Electrochim. Acta*, vol. 237, pp. 1–11, May 2017, doi: 10.1016/j.electacta.2017.03.131.

[134] A. A. Shah, H. Al-Fetlawi, and F. C. Walsh, “Dynamic modelling of hydrogen evolution effects in the all-vanadium redox flow battery,” *Electrochim. Acta*, vol. 55, no. 3, pp. 1125–1139, Jan. 2010, doi: 10.1016/j.electacta.2009.10.022.

[135] H. Al-Fetlawi, A. A. Shah, and F. C. Walsh, “Modelling the effects of oxygen evolution in the all-vanadium redox flow battery,” *Electrochim. Acta*, vol. 55, no. 9, pp. 3192–3205, Mar. 2010, doi: 10.1016/j.electacta.2009.12.085.

[136] A.-F. Hassan, “Modelling and Simulation of All-Vanadium Redox Flow Batteries,” University of Southampton, 2011.

[137] R. Badrinarayanan, J. Zhao, K. J. Tseng, and M. Skyllas-Kazacos, “Extended dynamic model for ion diffusion in all-vanadium redox flow battery including the effects of temperature and bulk electrolyte transfer,” *J. Power Sources*, vol. 270, pp. 576–586, Dec. 2014, doi: 10.1016/j.jpowsour.2014.07.128.

[138] X. Luo *et al.*, “Influences of Permeation of Vanadium Ions through PVDF-g-PSSA Membranes on Performances of Vanadium Redox Flow Batteries,” *J. Phys. Chem. B*, vol. 109, no. 43, pp. 20310–20314, Nov. 2005, doi: 10.1021/jp054092w.

[139] J. grosse Austing, C. Nunes Kirchner, L. Komsiyska, and G. Wittstock, “Investigation of crossover processes in a unitized bidirectional vanadium/air redox flow battery,” *J. Power Sources*, vol. 306, pp. 692–701, Feb. 2016, doi: 10.1016/j.jpowsour.2015.12.052.

[140] W. Xie, R. M. Darling, and M. L. Perry, “Processing and Pretreatment Effects on Vanadium Transport in Nafion Membranes,” *J. Electrochem. Soc.*, vol. 163, no. 1, pp. A5084–A5089, Oct. 2016, doi: 10.1149/2.0111601jes.

[141] Q. Luo *et al.*, “In-situ investigation of vanadium ion transport in redox flow battery,” *J. Power Sources*, vol. 218, pp. 15–20, Nov. 2012, doi: 10.1016/j.jpowsour.2012.06.066.

[142] D. C. Sing and J. P. Meyers, “Direct Measurement of Vanadium Crossover in an Operating Vanadium Redox Flow Battery,” *ECS Trans.*, vol. 50, no. 45, pp. 61–72, Apr. 2013, doi: 10.1149/05045.0061ecst.

[143] Y. Ashraf Gandomi, D. S. Aaron, and M. M. Mench, “Coupled Membrane Transport Parameters for Ionic Species in All-Vanadium Redox Flow Batteries,” *Electrochim. Acta*, vol. 218, pp. 174–190, Nov. 2016, doi: 10.1016/j.electacta.2016.09.087.

[144] J. Chahwan, C. Abbey, and G. Joos, “VRB Modelling for the Study of Output Terminal Voltages, Internal Losses and Performance,” in *2007 IEEE Canada Electrical Power Conference*, Oct. 2007, pp. 387–392, doi: 10.1109/EPC.2007.4520363.

[145] L. Barote and C. Marinescu, “A new control method for VRB SOC estimation in stand-alone wind energy systems,” in *2009 International Conference on Clean Electrical Power*, Jun. 2009, pp. 253–257, doi: 10.1109/ICCEP.2009.5212047.

[146] L. Barote, C. Marinescu, and M. Georgescu, “VRB modeling for storage in stand-alone wind energy systems,” in *2009 IEEE Bucharest PowerTech*, Jun. 2009, pp. 1–6, doi: 10.1109/PTC.2009.5281922.

[147] M. R. Mohamed, H. Ahmad, M. N. A. Seman, S. Razali, and M. S. Najib, “Electrical circuit model of a vanadium redox flow battery using extended Kalman filter,” *J. Power Sources*, vol. 239, pp. 284–293, Oct. 2013, doi: 10.1016/j.jpowsour.2013.03.127.

[148] B. Xiong, J. Zhao, Z. Wei, and M. Skyllas-Kazacos, “Extended Kalman filter method for state of

charge estimation of vanadium redox flow battery using thermal-dependent electrical model," *J. Power Sources*, vol. 262, pp. 50–61, Sep. 2014, doi: 10.1016/j.jpowsour.2014.03.110.

[149] Y. Zhang, J. Zhao, P. Wang, M. Skyllas-Kazacos, B. Xiong, and R. Badrinarayanan, "A comprehensive equivalent circuit model of all-vanadium redox flow battery for power system analysis," *J. Power Sources*, vol. 290, pp. 14–24, Sep. 2015, doi: 10.1016/j.jpowsour.2015.04.169.

[150] Z. Wei, K. J. Tseng, N. Wai, T. M. Lim, and M. Skyllas-Kazacos, "Adaptive estimation of state of charge and capacity with online identified battery model for vanadium redox flow battery," *J. Power Sources*, vol. 332, pp. 389–398, Nov. 2016, doi: 10.1016/j.jpowsour.2016.09.123.

[151] Z. Wei, J. Zhao, D. Ji, and K. J. Tseng, "A multi-timescale estimator for battery state of charge and capacity dual estimation based on an online identified model," *Appl. Energy*, vol. 204, pp. 1264–1274, Oct. 2017, doi: 10.1016/j.apenergy.2017.02.016.

[152] Z. Wei, A. Bhattarai, C. Zou, S. Meng, T. M. Lim, and M. Skyllas-Kazacos, "Real-time monitoring of capacity loss for vanadium redox flow battery," *J. Power Sources*, vol. 390, pp. 261–269, Jun. 2018, doi: 10.1016/j.jpowsour.2018.04.063.

[153] M. LI and T. HIKIHARA, "A Coupled Dynamical Model of Redox Flow Battery Based on Chemical Reaction, Fluid Flow, and Electrical Circuit," *IEICE Trans. Fundam. Electron. Commun. Comput. Sci.*, vol. E91-A, no. 7, pp. 1741–1747, Jul. 2008, doi: 10.1093/ietfec/e91-a.7.1741.

[154] A. Tang, J. Bao, and M. Skyllas-Kazacos, "Thermal modelling of battery configuration and self-discharge reactions in vanadium redox flow battery," *J. Power Sources*, vol. 216, pp. 489–501, Oct. 2012, doi: 10.1016/j.jpowsour.2012.06.052.

[155] Y. Yan, M. Skyllas-Kazacos, and J. Bao, "Effects of battery design, environmental temperature and electrolyte flowrate on thermal behaviour of a vanadium redox flow battery in different applications," *J. Energy Storage*, vol. 11, pp. 104–118, Jun. 2017, doi: 10.1016/j.est.2017.01.007.

[156] A. A. Shah, M. J. Watt-Smith, and F. C. Walsh, "A dynamic performance model for redox-flow batteries involving soluble species," *Electrochim. Acta*, vol. 53, no. 27, pp. 8087–8100, Nov. 2008, doi: 10.1016/j.electacta.2008.05.067.

[157] H. Al-Fetlawi, A. A. Shah, and F. C. Walsh, "Non-isothermal modelling of the all-vanadium redox flow battery," *Electrochim. Acta*, vol. 55, no. 1, pp. 78–89, Dec. 2009, doi: 10.1016/j.electacta.2009.08.009.

[158] M. Vynnycky, "Analysis of a model for the operation of a vanadium redox battery," *Energy*, vol. 36, no. 4, pp. 2242–2256, Apr. 2011, doi: 10.1016/j.energy.2010.03.060.

[159] X.-G. Yang, Q. Ye, P. Cheng, and T. S. Zhao, "Effects of the electric field on ion crossover in vanadium redox flow batteries," *Appl. Energy*, vol. 145, pp. 306–319, May 2015, doi: 10.1016/j.apenergy.2015.02.038.

[160] R. M. Darling, A. Z. Weber, M. C. Tucker, and M. L. Perry, "The Influence of Electric Field on Crossover in Redox-Flow Batteries," *J. Electrochem. Soc.*, vol. 163, no. 1, pp. A5014–A5022, 2016, doi: 10.1149/2.0031601jes.

[161] P. A. Boettcher, E. Agar, C. R. Dennison, and E. C. Kumbur, "Modeling of Ion Crossover in Vanadium Redox Flow Batteries: A Computationally-Efficient Lumped Parameter Approach for Extended Cycling," *J. Electrochem. Soc.*, vol. 163, no. 1, pp. A5244–A5252, Dec. 2016, doi: 10.1149/2.0311601jes.

[162] K. Oh, M. Moazzam, G. Gwak, and H. Ju, “Water crossover phenomena in all-vanadium redox flow batteries,” *Electrochim. Acta*, vol. 297, pp. 101–111, Feb. 2019, doi: 10.1016/j.electacta.2018.11.151.

[163] K. E. T.-A. J. Newman, *Electrochemical Systems*, 3rd ed. New Jersey: John Wiley Sons, 2004.

[164] Y. Shi *et al.*, “Recent development of membrane for vanadium redox flow battery applications: A review,” *Appl. Energy*, vol. 238, pp. 202–224, Mar. 2019, doi: 10.1016/j.apenergy.2018.12.087.

[165] X. Zhang, Y. Li, M. Skyllas-Kazacos, and J. Bao, “Optimal Sizing of Vanadium Redox Flow Battery Systems for Residential Applications Based on Battery Electrochemical Characteristics,” *Energies*, vol. 9, no. 10, p. 857, Oct. 2016, doi: 10.3390/en9100857.

[166] Sara Corcuera and Maria Skyllas-Kazacos, “STATE-OF-CHARGE MONITORING AND ELECTROLYTE REBALANCING METHODS FOR THE VANADIUM REDOX FLOW BATTERY,” *Eur. Chem. Bull.*, vol. 1, no. 12, pp. 511–519, 2012, doi: 10.17628/ECB.2012.1.511.

[167] X. Li, J. Xiong, A. Tang, Y. Qin, J. Liu, and C. Yan, “Investigation of the use of electrolyte viscosity for online state-of-charge monitoring design in vanadium redox flow battery,” *Appl. Energy*, vol. 211, pp. 1050–1059, Feb. 2018, doi: 10.1016/j.apenergy.2017.12.009.

[168] Z. Wei, C. Zou, F. Leng, B. H. Soong, and K.-J. Tseng, “Online Model Identification and State-of-Charge Estimate for Lithium-Ion Battery With a Recursive Total Least Squares-Based Observer,” *IEEE Trans. Ind. Electron.*, vol. 65, no. 2, pp. 1336–1346, Feb. 2018, doi: 10.1109/TIE.2017.2736480.

[169] Y. Li, M. Vilathgamuwa, T. Farrell, S. S. Choi, N. T. Tran, and J. Teague, “A physics-based distributed-parameter equivalent circuit model for lithium-ion batteries,” *Electrochim. Acta*, vol. 299, pp. 451–469, Mar. 2019, doi: 10.1016/j.electacta.2018.12.167.

[170] X. Cui, Z. He, E. Li, A. Cheng, M. Luo, and Y. Guo, “State-of-charge estimation of power lithium-ion batteries based on an embedded micro control unit using a square root cubature Kalman filter at various ambient temperatures,” *Int. J. Energy Res.*, vol. 43, no. 8, pp. 3561–3577, Jun. 2019, doi: 10.1002/er.4503.

[171] J. Lee, J. Kim, and H. Park, “Numerical simulation of the power-based efficiency in vanadium redox flow battery with different serpentine channel size,” *Int. J. Hydrogen Energy*, vol. 44, no. 56, pp. 29483–29492, Nov. 2019, doi: 10.1016/j.ijhydene.2019.05.013.

[172] A. Tang, J. Bao, and M. Skyllas-Kazacos, “Studies on pressure losses and flow rate optimization in vanadium redox flow battery,” *J. Power Sources*, vol. 248, pp. 154–162, Feb. 2014, doi: 10.1016/j.jpowsour.2013.09.071.

[173] Meng, Xiong, and Lim, “Model-Based Condition Monitoring of a Vanadium Redox Flow Battery,” *Energies*, vol. 12, no. 15, p. 3005, Aug. 2019, doi: 10.3390/en12153005.

[174] E. Agar, A. Benjamin, C. R. Dennison, D. Chen, M. A. Hickner, and E. C. Kumbur, “Reducing capacity fade in vanadium redox flow batteries by altering charging and discharging currents,” *J. Power Sources*, vol. 246, pp. 767–774, Jan. 2014, doi: 10.1016/j.jpowsour.2013.08.023.

[175] M. M. Denholm P, Ela E, Kirby B, “The Role of Energy Storage with Renewable Electricity Generation,” 2010. [Online]. Available: https://www.nrel.gov/docs/fy10osti/47187.pdf.

[176] J. K. Kaldellis, M. Kapsali, and K. A. Kavadias, “Energy balance analysis of wind-based pumped hydro storage systems in remote island electrical networks,” *Appl. Energy*, vol. 87, no. 8, pp. 2427–2437, Aug. 2010, doi: 10.1016/j.apenergy.2010.02.016.

[177] G. Caralis, D. Papantonis, and A. Zervos, “The role of pumped storage systems towards the large scale wind integration in the Greek power supply system,” *Renew. Sustain. Energy Rev.*, vol. 16, no. 5, pp. 2558–2565, Jun. 2012, doi: 10.1016/j.rser.2012.01.068.

[178] The Economist, “Energy Storage-Packing some power,” 2011. https://www.economist.com/technology-quarterly/2012/03/03/packing-some-power.

[179] J. Thierry, “Pumped storage in Switzerland - an outlook beyond 2000,” *Stucky*, 2012. http://www.stucky.ch/en/contenu/pdf/Pumped_storage_in_Switzerland_Dr_Jacob.pdf.

[180] C.-J. Yang, “Pumped Hydroelectric Storage,” in *Storing Energy*, Elsevier, 2016, pp. 25–38.

[181] B. K. James Ellison, Dhruv Bhatnagar, “Maui Energy Storage Study,” 2012. [Online]. Available: https://old.energyexemplar.com/wp-content/uploads/publications/Maui Energy Storage Study.pdf.

[182] O. of E. E. and R. Energy, “Pumped Storage Hydropower.” https://www.energy.gov/eere/water/pumped-storage-hydropower.

[183] A. Mitteregger and G. Penninger, “Austrian pumped storage power stations supply peak demands,” *World Pumps*, vol. 2008, no. 500, pp. 16–21, May 2008, doi: 10.1016/S0262-1762(08)70147-0.

[184] M. E. Nazari, M. M. Ardehali, and S. Jafari, “Pumped-storage unit commitment with considerations for energy demand, economics, and environmental constraints,” *Energy*, vol. 35, no. 10, pp. 4092–4101, Oct. 2010, doi: 10.1016/j.energy.2010.06.022.

[185] N. Sivakumar, D. Das, N. P. Padhy, A. R. Senthil Kumar, and N. Bisoyi, “Status of pumped hydro-storage schemes and its future in India,” *Renew. Sustain. Energy Rev.*, vol. 19, pp. 208–213, Mar. 2013, doi: 10.1016/j.rser.2012.11.001.

[186] J. P. Deane, B. P. Ó Gallachóir, and E. J. McKeogh, “Techno-economic review of existing and new pumped hydro energy storage plant,” *Renew. Sustain. Energy Rev.*, vol. 14, no. 4, pp. 1293–1302, May 2010, doi: 10.1016/j.rser.2009.11.015.

[187] F. Blaabjerg, A. Consoli, J. A. Ferreira, and J. D. VanWyk, “The Future of Electronic Power Processing and Conversion,” *IEEE Trans. Power Electron.*, vol. 20, no. 3, pp. 715–720, May 2005, doi: 10.1109/TPEL.2005.846516.

[188] D. Connolly, S. MacLaughlin, and M. Leahy, “Development of a computer program to locate potential sites for pumped hydroelectric energy storage,” *Energy*, vol. 35, no. 1, pp. 375–381, Jan. 2010, doi: 10.1016/j.energy.2009.10.004.

[189] R. Baxter, *Energy storage: a nontechnical guide*. Tulsa, OK: PennWell, 2006.

[190] Jiaqi Liang and R. G. Harley, “Pumped storage hydro-plant models for system transient and long-term dynamic studies,” in *IEEE PES General Meeting*, Jul. 2010, pp. 1–8, doi: 10.1109/PES.2010.5589330.

[191] H. Taniguchi, T. Nagao, and H. Higasa, “Development of a pumped-storage power station model for power system stability study,” *Electr. Eng. Japan*, vol. 112, no. 3, pp. 50–62, 1992, doi: 10.1002/eej.4391120306.

[192] L. N. Hannett, B. P. Lam, F. S. Prabhakara, Qiu Guofu, Ding Mincheng, and Bian Beilei, “Modeling of a pumped storage hydro plant for power system stability studies,” in *POWERCON ’98. 1998 International Conference on Power System Technology. Proceedings (Cat. No.98EX151)*, vol. 2, pp. 1300–1304, doi: 10.1109/ICPST.1998.729296.

[193] S. P. Mansoor, D. J. Jones, D. A. Bradley, F. C. Aris, and G. R. Jones, “Stability of a pump storage hydro-power station connected to a power system,” in *IEEE Power Engineering Society. 1999 Winter Meeting (Cat. No.99CH36233)*, 1999, pp. 646–650 vol.1, doi: 10.1109/PESW.1999.747531.

[194] H. M. Gao and C. Wang, “A detailed pumped storage station model for power system analysis,” in *2006 IEEE Power Engineering Society General Meeting*, 2006, p. 5 pp., doi: 10.1109/PES.2006.1709259.

[195] and T. O. O. Nagura, M. Higuchi, K. Tani, “Hitachi’s Adjustable-Speed Pumped-Storage System Contributing to Prevention of Global Warming,” *Hitachi Rev.*, vol. 59, no. 3, 2010, [Online]. Available: https://www.hitachi.com/rev/pdf/2010/r2010_03_107.pdf.

[196] M. Mohanpurkar *et al.*, “Real-time co-simulation of adjustable-speed pumped storage hydro for transient stability analysis,” *Electr. Power Syst. Res.*, vol. 154, pp. 276–286, Jan. 2018, doi: 10.1016/j.epsr.2017.08.010.

[197] A. C. Padoan *et al.*, “Dynamical Behavior Comparison Between Variable Speed and Synchronous Machines With PSS,” *IEEE Trans. Power Syst.*, vol. 25, no. 3, pp. 1555–1565, Aug. 2010, doi: 10.1109/TPWRS.2009.2039586.

[198] C. Nicolet, “Hydroacoustic modelling and numerical simulation of unsteady operation of hydroelectric systems,” 2007.

[199] J. Feltes *et al.*, “Review of Existing Hydroelectric Turbine-Governor Simulation Models,” Argonne, IL (United States), Oct. 2013. doi: 10.2172/1098022.

[200] G. Kaye and W. Higgins, “The thermal conductivity of solid and liquid sulphur,” *Proc. R. Soc. London. Ser. A, Contain. Pap. a Math. Phys. Character*, vol. 122, no. 790, pp. 633–646, Feb. 1929, doi: 10.1098/rspa.1929.0049.

[201] K. Manohar and K. Ramroop, “A Comparison of Correlations for Heat Transfer from Inclined Pipes,” *Int. J. Eng.*, vol. 4, no. 4, pp. 268–278, 2010.

[202] R. G. Kemink and E. M. Sparrow, “Heat transfer coefficients for melting about a vertical cylinder with or without subcooling and for open or closed containment,” *Int. J. Heat Mass Transf.*, vol. 24, no. 10, pp. 1699–1710, Oct. 1981, doi: 10.1016/0017-9310(81)90078-8.

[203] Y. Nagasaka and A. Nagashima, “The thermal conductivity of molten NaNO3 and KNO3,” *Int. J. Thermophys.*, vol. 12, no. 5, pp. 769–781, Sep. 1991, doi: 10.1007/BF00502404.

[204] M. Lança, M. Lourenço, F. Santos, V. Nunes, and C. N. de Castro, “Viscosity of molten potassium nitrate,” *High Temp. Press.*, vol. 33, no. 4, pp. 427–434, 2001, doi: 10.1068/htwu496.

[205] T. Yamamura, N. Watanabe, T. Yano, and Y. Shiokawa, “Electron-Transfer Kinetics of Np[sup 3+]/Np[sup 4+], NpO[sub 2][sup +]/NpO[sub 2][sup 2+], V[sup 2+]/V[sup 3+], and VO[sup 2+]/VO[sub 2][sup +] at Carbon Electrodes,” *J. Electrochem. Soc.*, vol. 152, no. 4, p. A830, 2005, doi: 10.1149/1.1870794.

[206] T. E. Springer, T. A. Zawodzinski, and S. Gottesfeld, “Polymer Electrolyte Fuel Cell Model,” *J. Electrochem. Soc.*, vol. 138, no. 8, pp. 2334–2342, Aug. 1991, doi: 10.1149/1.2085971.

[207] E. Agar, C. R. Dennison, K. W. Knehr, and E. C. Kumbur, “Identification of performance limiting electrode using asymmetric cell configuration in vanadium redox flow batteries,” *J. Power Sources*, vol. 225, pp. 89–94, Mar. 2013, doi: 10.1016/j.jpowsour.2012.10.016.